이학박사학위논문

Electronic Structure and Blinking Kinetics of Single CdSe Quantum Dots Studied with Scanning Tunneling Microcopy and Spectroscopy

CdSe 양자점의 전기적 구조와 깜빡임 동역학의 주사터널링현미경 및 분광학 연구

2012 년 8 월

서울대학교 대학원

물리천문학부

임 성 준

이학박사학위논문

Electronic Structure and Blinking Kinetics of Single CdSe Quantum Dots Studied with Scanning Tunneling Microcopy and Spectroscopy

CdSe 양자점의 전기적 구조와 깜빡임 동역학의 주사터널링현미경 및 분광학 연구

2012 년 8 월

서울대학교 대학원

물리천문학부

임 성 준

Abstract

Since Quantum Dot (QD) has a size-tunable energy gap, it has various promising applications like QD display, biological fluorophore and photo voltaic device. In the way of applications, the intermittency in fluorescence so called 'blinking' hinders the efficient generation of photons. Various models are suggested to describe this phenomenon, but the fundamental mechanism is not fully understood yet. Recent single QD Photo Luminescence (PL) experiments revealed dot-to-dot variation in the blinking, so more local probings of QDs are required. Scanning Tunneling Microscopy (STM) and Spectroscopy (STS) studies are adequate to observe such local variations of electrical properties for its high spatial and energy resolution.

In this study, we used pulse injection method to deposit QDs on various surfaces. With the method, we deposited CdSe/ZnS core-shell type QDs capped with organic molecules on gold, nickel and hexagonal Boron Nitride (h-BN) thin film which are representatives of inert metal, reactive metal and inert insulator, respectively. And the electronic states are measured by STS. Though some QDs show electrical structure consistent with ab-initio calculation, most of QDs have some unexpected electrical states inside the gap region. Besides, such states have certain distribution on single QD surface and localized in about 1 nm range.

Some blinking models suggested the existence of external trap states to explain the dark state of the blinking. The observed states can prove the validity of the trap models and suggest some improvements of the models with the information about the distribution of the trap states. With the realistic distribution of the trap states,

we suggest a simple model which explains the origin of the trap state as an external defects with capping molecule bonded. Though the individual capping molecules are not resolved on QD surface, Negative Differential Resistance (NDR), observed at high tunneling current, proved the existence of a capping molecule barrier under the QD. Numerical simulation of the Double Barrier Tunneling Junction (DBTJ) reproduced the observed NDR and also provided the relevant thickness of capping molecule.

By combining a photon detection system with STM, a simultaneous measurement of the tunneling current and photons from a single QD is possible, and it will end the long debates on the blinking mechanism.

Keywords: Quantum Dot, Trap State, Capping Molecule, Negative Differential Resistance, Scanning Tunneling Spectroscopy

Student Number: 2005-20377

Table of Contents

Figure Contents

Chapter 1 Quantum Dot and its Applications

1.1 Energy Levels of QD

Semiconductor nanocrystals, often called Quantum Dots (QDs), have been studied intensively for its confined discrete energy levels[53] and their tunability by size. We can calculate the electronic energy levels by Density Functional Theory (DFT)[19] calculation or Linear Combination of Atomic Orbitals (LCAO)[4, 36]. However, with these methods, only small size QDs can be calculated because of the massive size of the calculation[61]. In the other way, tight binding calculations based on effective mass approximation are also possible, and these methods have their origins in band structure of bulk material. With these approaches, electron levels from conduction bands and hole levels from valence bands can be obtained. In section 1.1.1, the substance of the "top down'' approach is introduced.

1.1.1 Confined States

QD has a forbidden energy gap originated from its semiconductor nature[51] and the gap is tunable by the size of the crystal or in other words controlling the confinement effect[68]. So a theoretical prediction of the change of energy gap from the bulk value can be achieved by introducing a confinement potential to the bulk states as a perturbation. Like the Bloch theorem introduced the periodicity of crystal lattice through the Bloch envelope function[13], QD states also can be described by the envelope function correspond to the confinement potential. In this context, the derivation of the Bloch theorem has some common ideas with the perturbation approach of

QD[11].

Understanding the motion of electrons in indefinite amount of atoms is not an easy task[37]. Bloch's theorem, however, makes the situation feasible with simple assumptions of periodicity. It states that the eigenstates of infinitely periodic lattice can be written as the convolution of a plane wave envelope function and a periodic Bloch function $u_{nk}(r)$.

$$\psi_{nk}(r) = e^{ik\cdot r} u_{nk}(r) \tag{1.1}$$

Here n and k denotes the band index and the momentum vector, respectively. The Bloch function corresponds to the energy eigenvalue of $\epsilon_n(k) = \epsilon_n(k+K)$ which shows the same periodicity with the lattice. The deconvolution is relevant to the extraction of the translational symmetry which shows the invariance under a translational movement in multiples of the lattice constant. In other words, the lattice periodicity of the original Hamiltonian results in the same periodicity of the resultant eigenenergies and eigenstates. The relation between these eigenstates and eigenenergies with the original Hamiltonian says

$$H_0\psi_{nk} = \epsilon_n(k)\psi_{nk} = \epsilon_n(k)e^{ikr}u_{nk}(r) \tag{1.2}$$

Then these bulk states can be a basis for QD confined states.

In the case of QD which has bounded states rather than the infinitely periodic states, the new eigenstate can be obtained using perturbation approach to the original Hamiltonian as follows

$$(H_0 + U)\psi = \epsilon\psi \tag{1.3}$$

where U is the confinement potential which prevents electrons from going out of the QD. As a consequence of this perturbation, the newly acquired eigenstates are expanded as a series of the original eigenfunctions near the band minimum for conduc-

tion band (or maximum for valence band).[1] The expansion of ψ with $k = 0$ component of $u_{nk}(r)$ is

$$\chi_{nk} = e^{ikr} u_{n0} \tag{1.4}$$

Like the envelope function approach in the Bloch theorem, we introduce $A_n(k)$ as a coefficient of ψ expansion in momentum space as $\psi = \sum_{n'} \int dk' A_{n'}(k') \chi_{n'k'}$. By substituting the expression into the original Hamiltonian, we get multi band Schrödinger equation for the envelope function[19].

$$\sum_{n'=bands} \int \langle nk|H_0 + U|n'k'\rangle A_{n'}(k') = \epsilon A_n(k) \tag{1.5}$$

Note that this Schrödinger-like equation is different from the original Schrödinger equation because it is summed over multi band and represented in momentum space. To obtain proper momentum space representation of the Hamiltonian, we substitute k' by the del operator and use the periodicity of u_{n0}. (in other words, $\langle nk|H_0|n'k'\rangle = \int e^{-ik\cdot r} u^*_{n0} H_0 e^{ik'\cdot r} u_{n'0} dr$ can be represented as $\delta(k-k')[(\epsilon_n(0) + \frac{k^2}{2m})\delta_{n'n} + \frac{k\cdot p_{nn'}}{m}]$, where $p_{nn'} \propto \int u^*_{n0}(-i\nabla) u_{n'0} dr$.) Then the (Eq. 1.5) can be written as follows.

$$(\epsilon_n(0) + \frac{k^2}{2m}) A_n(k) + \sum_{n'\neq n} \frac{k\cdot p_{nn'}}{m} A_{n'}(k) + \int dk' u(k-k') A_n(k') = \epsilon A_n(k) \tag{1.6}$$

Though we started the derivation near the band extrema, the first two terms in (Eq. 1.6) approximate the value of $\epsilon_n(k)$ up to second order in k.

To obtain the representation in real space, the function $A_n(k)$ can be inverse-Fourier transformed to $A_n(k) = \frac{\Omega}{(2\pi)^3} \sum_m e^{-ikR_m} F_n(R_m)$ where R_ms denote all the lattice points. With the definition of $F_n(r)$ and the simplification of first two terms in (Eq. 1.6), the simplified form of (Eq. 1.6) is acquired as follows.

$$[\epsilon_n(-i\nabla) + U(r)] F_n(r) = \epsilon F_n(r) \tag{1.7}$$

[1] Because of this assumption, higher order excited states cannot be described properly with this approach. The result only describes the states near the band extrema.

To emphasize that this equation is different from the original Schrödinger equation, they should be noted that this envelope Schrödinger-like equation is a sum of equations for each band and also that the k in the original Hamiltonian (the first term) is replaced by $-i\nabla$ which means the $k \cdot p$ Hamiltonian is used here[23].

And finally, to recover the eigenstate ψ of the whole system, we use this envelope function as "envelope" of the bulk eigenstate near the band edges.

$$\psi_c = F_c(r)\psi_c(r) \tag{1.8}$$

$$\psi_v = F_v(r)\psi_v(r) \tag{1.9}$$

Their energy levels are briefly represented by schematic diagram in (Fig. 1.1).

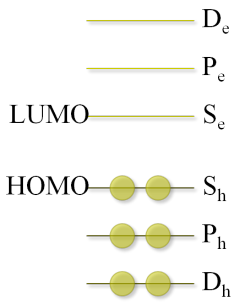

Figures 1.1 **Discrete Levels of QD** - S, P and D denotes symmetries analogous to the atomic orbitals and the subscription e and h denote electron and hole levels, respectively

This envelope function approach has an advantage, because we acquire Schrödinger-like equation with only the confinement potential included. This means that the fundamental characteristics of this system is not much different from the elementary quantum mechanical problem, called "particle-in-a-box", or "particle-in-a-spherical-box" like a hydrogen atom[30]. In this sense, QD states are also called artificial atom states[41]. We should note that the spherical box model cannot predict exact electronic structure of QD, but symmetries of some low lying states are almost exactly

predicted.

To examine the analogy of the obtained discrete energy levels with other systems, first we compare the states with molecular orbitals. Molecules also have discrete energy levels called molecular orbitals. The Fermi level or the chemical potential describes that which of these levels is filled or empty. Common notation to indicate the highest filled level is Highest Occupied Molecular Orbital (HOMO) and Lowest Unoccupied Molecular Orbital (LUMO) for the lowest empty level. Despite the size of QD is much bigger than molecules, QDs can be viewed as big "molecules"[66]. In this analogy, we usually indicate the first excited state of QD as LUMO and the second as LUMO+1 and so on. And these unoccupied states are occupied when an electron is excited from its ground state. The filled states also have the same analogy with HOMO levels and they are occupied when a hole (an absence state of electron) is created.

Another analogy of QD can be found from atomic orbitals[60]. The envelope function shares the same form of equation with a hydrogen atom and the confinement potential also has a spherical symmetry. Only the differences are the relatively bigger size and dielectric property of semiconductor material (or surrounding materials). The dielectric screening makes QD even similar to a hydrogen atom. The details of potential from each ionic core are effectively screened by the dielectric property, and an electron or a hole in the excited states feels strongly screened potential inside the QD. Then they behave like they are the only particles in the QD. These aspects are well reflected by the fact that the first few excited states of QD have almost the same spatial symmetries described by S, P and D. The major difference of QD states from atomic orbitals is that hole states in QD have no analogy in real atom. To distinguish the hole states from the electron states, the notation of the QD confined states are

accompanied by subscripts, "e" and "h", as in S_e, P_e, D_e or S_h, P_h, D_h, etc.

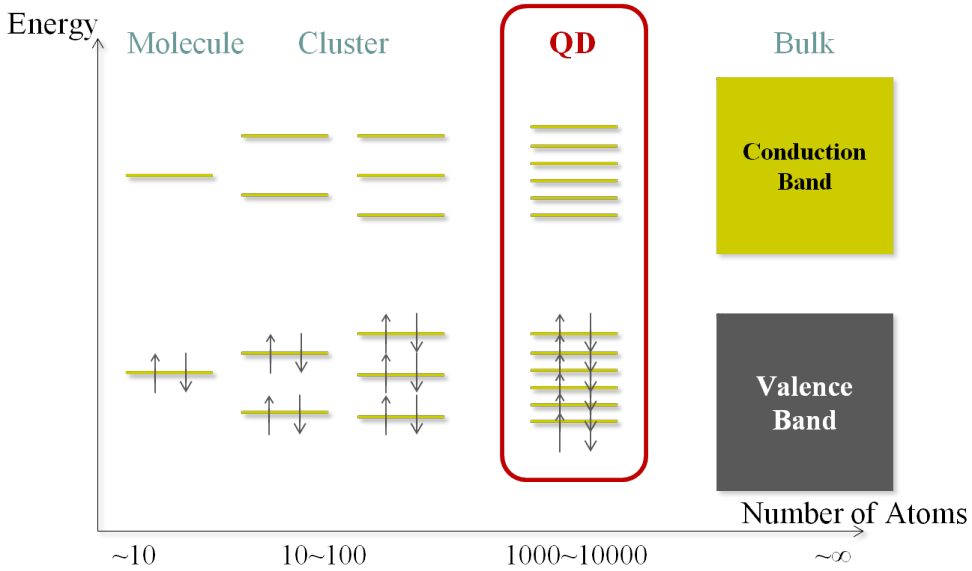

Figures 1.2 **In-between Nature of QD** - QDs have characteristics between bulk and molecular states. They have discrete energy levels analogous to molecular orbitals and also semiconducting energy gap analogous to bulk band gap.

The envelope function approach shows "top down" view point of the discrete energy levels in QD[6], while analogies to molecular or atomic orbitals exhibit "bottom up" view point. This intermediate property comes from QD's size which is in the middle of bulk and molecule as in (Fig. 1.2).

1.1.2 Excitonic States

Most distinguished feature of the discrete energy levels in QD is that they can create or absorb photons[9]. The QD interactions with the photon include emission and absorption. By absorbing photons, QD creates an excited electron which occupies excited electron states (e.g. S_e, P_e, etc.), while leaves a hole in the hole excited states (e.g. S_h, P_h, etc.)[46]. And the opposite reaction is possible through a recombination

of the excited electrons and holes. When an electron and a hole are created at the same time, like the situation of photon absorption, they have different energy from the sum of the single particle excited states[9], because of their electron-hole interaction (mostly, it comes from the coulomb interaction)[5]. So their coexistence makes a new quasi particle state called the exciton.

The exciton states in bulk semiconducting materials are categorized by two.

- Frenkel exciton
- Wannier-Mott exciton

The Frenkel exciton describes a strongly localized state of electron-hole pair of which spatial extension is comparable to the unit cell size of the lattice, while the Wannier-Mott exciton indicates the delocalized or weakly coupled states of them. So the Wannier-Mott exciton size is sometimes extended more than few hundred times of the lattice constant.

These two concepts, which are originally describe the exciton states in bulk semiconductor, can be expanded generally. So they indicate the strength of electron-hole interaction. That means if the spatial distance of the electron-hole interaction is larger than the system's natural unit size (for example, size of single molecule in molecular aggregation, atomic lattice size in semiconductor) then the exciton is in the Wannier-Mott regime. Or, for the opposite case it is in the Frenkel exciton regime.

In this context, QD exciton is said to be in the mid-range of those two regimes[10]. For the bulk exciton, the size can be extended few tens or hundreds of nanometers for semiconductor material. That means that the QD exciton undergoes confinement[48] as the size of bulk material is reduced to QD size. So the original Wannier-Mott nature of the exciton is modified by this confinement[53]. They, however, have larger

size than the lattice size, so they are still different from the Frenkel exciton. At this moment, we need truly generalized picture of exciton to resolve the characteristics.

Understanding exciton physics is closely related to an interactions between electronic states and photon[65]. The excitons are created by both of free carrier or photon. The former case can be found in electroluminescence and the latter in photoluminescence or photovoltaic system. In the electroluminescence, the excitons are created by free carriers (electrons and holes) and then decay as photons. And excitons are created by incoming photons and decay as photons (free carriers) in the photoluminescence process (photovoltaic). Throughout these processes, the exciton plays the central role.

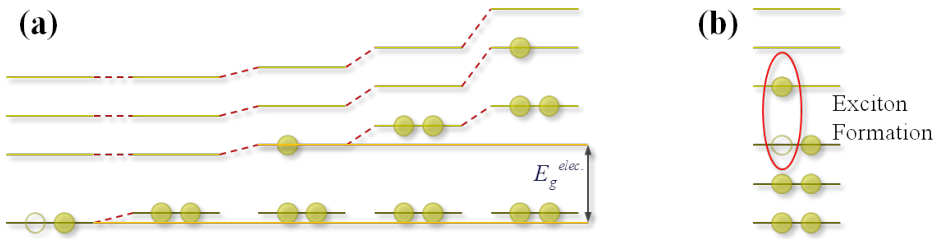

Figures 1.3 **Two Different Gap Measurements** - (a) Quasi Particle Gap Measurement: we measure the difference in the electron and hole excitation energy (b) Optical Gap Measurement: we measure the energy of an electron and a hole pair.

The single particle approach only gives us the ground states, and the excited states are different from the ground states. The contributions come from QD polarization, electron-electron interaction and exchange interaction. Among these interactions, the polarization energy is the major contribution, and can be written as follows.

$$E_e = E_{S_e} + \Sigma_e^{pol} \tag{1.10}$$

$$E_h = E_{S_h} + \Sigma_h^{pol} \tag{1.11}$$

However, the excitonic states are different from the sum of the excited states in (Eq. 1.7). In the case of the exciton formation (e.g. an excited electron and a hole), the interaction between electron and hole should be considered. This energy difference is the exciton binding energy. Generally the binding energy of the excitons in bulk semiconductor is relatively lower than that of other excitons in molecular aggregation or carbon nanotube. The binding energy of the QD exciton has middle size compared to the two cases. The excited electrons and holes are forced to confined in a small size of QD (e.g. QD size is smaller than bulk Wannier-Mott exciton), so the binding energy of QD exciton is larger than bulk exciton. Molecular aggregation or CNT exciton, however, have excitons much localized size and consequently larger binding energy than QD. Here again we can see that we need more generalized approach to describe this middle ranged binding energy.

1.2 Applications of QD

QDs have been studied intensively since the development of chemical synthetic method in early 1990s[42]. The QDs have attractive properties like size-tunable energy gap, adaptable chemical property changeable by exchanging the surface capping molecule and solution processability which enables mass production, storage and deposition. Because of these advantages, QDs are considered as being used in many applications like light emitting device, biological imaging or solar cell.

Though the applications of QDs are now at the stage of commercialization and statistical properties of QDs are well known from ensemble experiments, the fundamental properties are not fully understood yet at the single QD level. In addition to the averaged property of QD, the details of QD surface and their influence to the electronic structure should be observed to improve the understanding and the

applicability of QD.

1.2.1 Synthesis of QD

QDs can be synthesized by various methods like precipitation[10] or epitaxial growth. Especially the invention of hot-injection method [42] promotes the development of numerous applications, since it utilizes mass production, tunable size and energy gap, variation of material and prolonged storage time. In the hot-injection method, precursor materials of QDs are injected to ligand solvent at elevated temperature[16]. At the high temperature, the ligand molecules act like solvent, so the precursor materials dissolve and form a solution phase[54]. With the aid of fine temperature control, the solution undergoes a supersaturation and a nucleation phase according to the programmed temperature sequence. In the nucleation phase, nanocrystals of semiconductor material begin to grow and at the specific time, the growth is terminated by the extraction of solution out of the vessel. After the extraction, solvent molecules passivate the surface of the QD and stop the nucleation process. After removing the excessive precursors and the capping molecules, pure QD materials can be isolated from the solution.

A typical structure of QD with the hot-injection method is illustrated in (Fig. 1.4). QDs can have different sizes, core-shell materials, shapes and types of capping molecules. With these flexible tunability of chemical and optophysical properties, the QDs can be adapted to diverse environments and applications.

1.2.2 Light Emitting Diode

QDs have spectrally narrow emissions controlled by delicate chemical synthesis and are known to be more stable compared to other organic fluorophores[15], because they are composed of inorganic materials. So QDs are considered as a good candidate

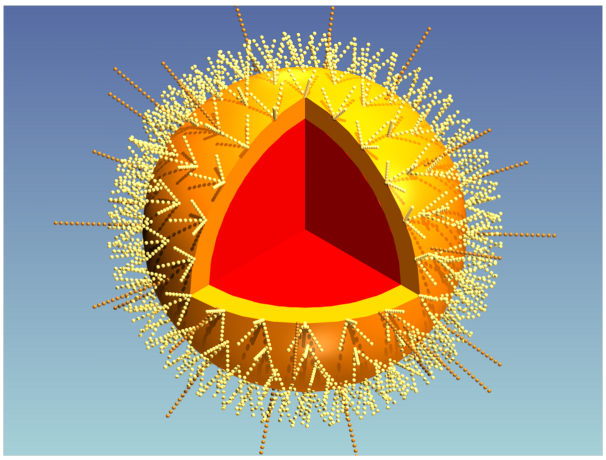

Figures 1.4 **Typical Structure of QD** - 3-Dimensional solid model of typical core-shell type QD with surrounding capping molecules.

of next-generation display[29] or illumination device[1]. The principal advantages of using QDs as light emitters[63] can be summarized as follows.

- Mass Productable
- Inorganic Material (Stability)
- Narrow and Tunable Emission Band

The prescribed hot-injection method using organometallic precursors is easily scalable and the capping layer prevents degradation or aggregation during storage and device fabrication. Because QDs are dissolved in organic solvents like the case of organic fluorophores, they can be deposited as thin films by spin coating. And recently, another method to make close-packed QD thin films with least chemical impurities was developed. In the method, which is called contact printing, QDs are uniformly dispersed on PDMS material and the PDMS stamp softly contacts the target surface. With the proper control of speed and force of the stamping, full color QD LED device

was fabricated with record luminescence efficiency.

In comparison with the organic light emitting devices (OLEDs), QDs are inherently more stable for its inorganic nature. The OLEDs of commercial devices have a major limit, the lifetime. Though QD has inorganic nature, the early QD devices have similar structure of OLEDs to perform electroluminescence. The first demonstration of electroluminescence from QD thin film embedded in organic material transport layers showed 0.52% of external quantum efficiency in 2002. Though the early stage efficiency is not satisfactory compared to commercial OLED devices, steeply developed technologies in this architecture recently show external quantum efficiency of about 7% which is comparable to that of the OLED. Though the approach of organic layer architecture lacks the benefit of stability, it proved the possibility of successful fabrication of QD luminescence.

Recently, efforts to make fully inorganic-material based device are focused. Though they exhibited relatively low efficiencies about 1∼2 orders of magnitude lower than OLED, their efficiencies are developed by 2 orders through its short development history. Besides the fully inorganic QD LED already proved its stability by air stable operation without packaging which is impossible in OLED technology[64].

QD LEDs already have proven its ability to tune the color with ultimately narrow bandwidth. The typical emission spectra of QD shows a full-width at half-maximum (FWHM) of 30∼40 nm. The monodispersity is achieved by fine size control during the synthesis. With the pure colors, QD LEDs can show saturated colors with high hue values as can be seen in (Fig. 1.5). QDs are already commercialized in forms of optical down conversion devices which control the color and temperature of illumination by adding mixed luminescence from QD and LED. With the aid of QD, established LED devices can finely tune its temperature and raise its luminescence efficiency.

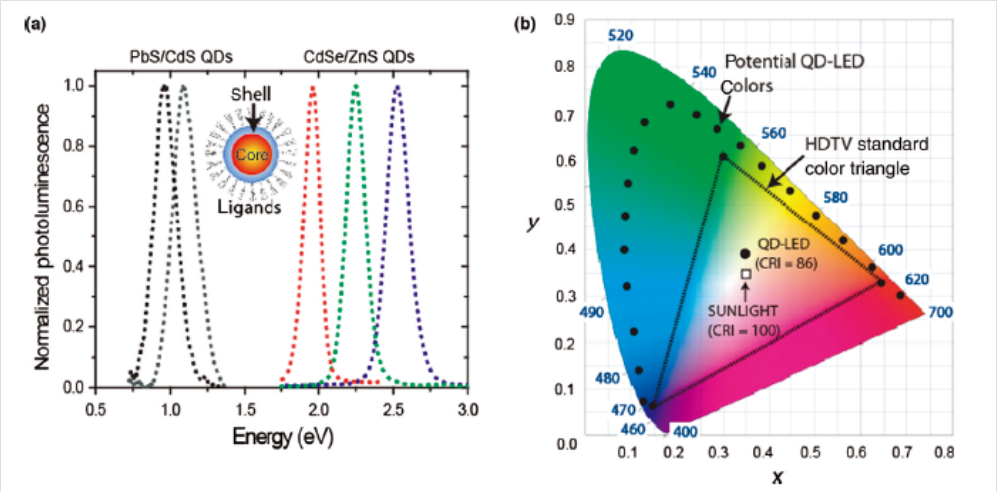

Figures 1.5 **Narrow Band of QD Emission and Chromaticity Diagram of QD-LED** - (a) Photoluminescence spectra of CdSe/ZnS and PbS/CdS QDs showing narrowband emission across the visible and near infra red regions (b) Commission Internationale de l'Eclairage (CIE) chromaticity diagram showing that the spectral purity of QDs enables a color gamut larger than the HDTV standard[63]

1.2.3 Biological Application

Another important application of QD is found in biological imaging[7, 18]. Most studies are focused on developing near infra red luminescent QDs ranging from 700 to 900nm[28]. Because the luminescence in that range has high penetration depth on tissue and also the wavelength is different from tissue's autofluorescence of about 400 to 600 nm. With the aid of the functionalization of QD surface with various ligand materials, biological imaging with QD can achieve specific target imaging and reduction of nonspecific binding.

1.3 Blinking Phenomena

Most applications of QD have photon related physics as its fundamental. In this aspect, fluorescence intermittency which is so called "blinking" is the most serious

disturbance in the applications[62, 22]. Since the first observations in CdSe QD photo-luminescence in 1994, the blinking has been a major obstacle which limits the viability of QDs in many applications. During the blinking, QD shows non-constant intensity in photo luminescence. The bright states of photo luminescence are often called the "on" state and the other states are called the "off" state. This alternating appearance of the on and off states limits the efficiency and hinders the using of QD as stable single photon emitter. Recent progress in QD LED and biological imaging with QD luminescence proved the possibility of using QDs as bright, pure-colored and single photon source of luminescence. Despite the improvement of QD applications are continued without exclusion or understanding of the blinking, it is apparent that we will induce further improvements if we can find and tame the blinking mechanism. Other new born applications like solar cell or QD laser also suffer from the loss mechanisms related to the blinking.

1.3.1 Proposed Mechanisms

Though it has been long to find the fundamental mechanism of blinking for about 15 years, no successfully accepted description of blinking is currently available[47, 67]. There are many difficulties in finding the blinking mechanism. The representative properties of this phenomenon are summarized in the following items.

- Blinking occurs over a wide range of timescales
- Blinking lacks dependence on temperature

QD photo luminescence intensity typically shows on and off states alternately during the blinking. The transition time from "on to off" or "off to on" can be defined as time between two threshold intensities. The time between each transition

is called on-time or off-time, respectively. The distribution of on or off-time typically exhibits power law behavior[40]. This distribution shows very wide range from ms to min or hour scale which ranges over 5 orders of magnitude. The wide range of timescale is not easily explained by one universal mechanism[49].

The blinking process is relatively insensitive to temperature change as checked by experiments from 4K to 300K. This has led one to speculate that tunneling process (which is temperature independent) is at play.

Though there are many difficulties to make model to simulate the blinking phenomena[31], there have been constant effort to find proper models to explain the mechanism of the blinking. Some suggested models are summarized here.

(1) Multiple trap model: this model assumes the existence of multiple electron traps near the quantum dot. Owing to a static distribution of trapping and de-trapping rates, varying with distance and/or trap depth, power-law off-time distributions are obtained. Furthermore, this model readily explains the dependence of off-time power-law slopes on the dielectric properties of the environment. Finally, the lack of temperature dependence can be explained through a tunneling process.

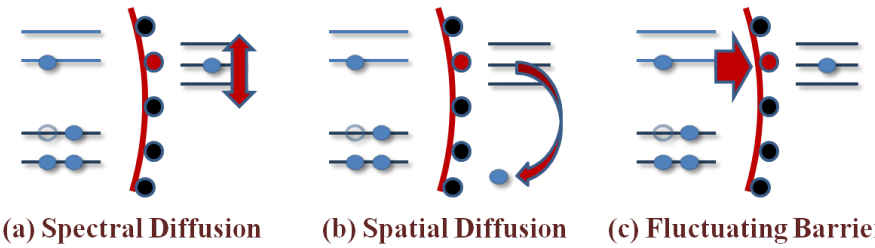

Figures 1.6 **Various Suggested Mechanisms of Blinking with External Traps** - (a) Power law behavior of blinking can be described by spectral diffusion of external trap states. exceptionally long period of off time can be assigned to the spectral shift of external trap states (b) Another mechanism explains the prolonged off time by diffusion of electron alongside the surface of QD (c) Some models assume the tunneling barrier between QD and external barrier can fluctuate from time to time

(2) Spectral diffusion model: This model hypothesized a resonant tunneling between QD confined states and external trap states. Because the power-law behavior cannot be obtained by static trap states, this model assumes the diffusion of the trap energy levels. So the tunneling to the diffusive level exhibits the power-law behavior. A key prediction of this model is a change in the slopes of both on-time and off-time power laws from 3/2 at long times to 1/2 at short times. Interestingly, this has recently been corroborated by power spectral density experiments.

(3) Spatial diffusion model: This model suggests that any ejected electron carries out a three-dimensional diffusion in space about the quantum dot before its return. So the extremely long lifetime of the off state is easily explained in this model.

(4) Fluctuating barrier model: Kuno et al. have alternatively suggested a model where emission intermittency involves fluctuations in the height or width of a tunneling barrier between an electron within the quantum dot and an external trap state. However, revealing the origin of the fluctuation is prerequisite of this model.

(5) Fluctuating non-radiative rate model: Frantsuzov and Marcus have suggested that quantum dot intermittency is a result of the fluctuations of the non-radiative recombination rate. Recombination occurs through the Auger-assisted excitation of deep surface states and is followed by relaxation to the ground state. The trapping rate is then governed by the spectral diffusion of a second excited quantum dot state (1Pe), which modulates the eventual non-radiative recovery of the system.

1.3.2 Trap States

Most of suggested theoretical models hypothesized the existence of external trap states around QD (from the lists above (1) - (4))[24, 33]. Though the existence of this trap states is continuously predicted, direct evidence of the trap states is not yet detected[47, 12]. In this context, STM which is capable of visualizing electronic states

in sub-atomic scale can be a proper tool to verify the existence of the trap states[32]. Combined with photon detection, STM can find the existence of the trap states and the relation between the trap states and blinking phenomena[38].

Chapter 2 Scanning Tunneling Microscopy and Spectroscopy

2.1 Introduction

Since the first invention in 1982, Scanning Tunneling Microscopy (STM) and Scanning Tunneling Spectroscopy (STS) have been unique tools to study various systems of surface science. STM and STS have sub-atomic resolution resulted from localized nature of quantum tunneling phenomena and sub-mV energy resolution with low operation temperature. Traditional STM studies are found in surface topography, reconstruction, growth dynamics, chemical property or magnetic property. But STM continued to expand its applications from these typical surface science studies to other samples or environments. STM expanded its operation environment from vacuum to ambient and liquid, operation temperature from room temperature to extremely low (10 mK range) or high temperature and is utilized with high magnetic field up to 15T or vector magnetic field. And STM even acquired temporal resolution by fast current amplifier and electronics to overcome its limitation in slowness. In these contexts, the history of STM can be summarized by expansion of its operation environment.

STM also tried to extend the choice of samples. STM founds many variations in samples so that it applied to doped semiconductor, super conductor, high-Tc superconductor, molecules, molecular aggregation, buried dopant, biological sample and graphene. In this point of view, STM successfully expanded its range of sample choice and now almost all nanosized objects are studied by STM and STS. QD or colloidal semiconductor nanocrystal is also such an example.

2.2 Tunneling Current Modeling

Methods for tunneling current modeling in STM can be summarized as follows

- Tersoff-Hamann approach
- Transfer Hamiltonian approach
- Landauer Bütticker approach
- Keldish or non-equilibrium Green's function approach

2.2.1 Tersoff-Hamann Approach

Tersoff-Hamann approach is the first attempt to modeling the tunneling current to emphasize its high spatial resolution and ability to extract sample's density of states with some simplifications to tip wave function[57]. From the original paper, they assumed simplified s-wave type tip wavefunction to focus on the sample wavefunction. From Bardeen's perturbation approach, tunneling current is expressed as follows

$$I \propto \sum_{\nu} |\psi_{\nu}(\vec{r_0})|^2 \delta(E_{\nu} - E_F) \tag{2.1}$$

Note that this perturbation approach only gives successful result near the Fermi energy. The subscript ν expresses each eigenstate of sample surface and $|\psi_{\nu}(\vec{r_0})|$ represent the magnitude of the sample wavefunction at the center of curvature of the tip. This equation is direct result of simplification of tip wavefunction as $\psi_{\mu} \propto \frac{e^{-k|\vec{r}-\vec{r_0}|}}{k|\vec{r}-\vec{r_0}|}$ which is exponentially decaying spherical wavefunction.

2.2.2 Transfer Hamiltonian Approach

This approach is the backbone of the Tersoff-Hamann approach, and originally called the Bardeen's tunneling theory[25]. In this approach, the sample eigenstate

is expressed as the sum of the original eigenstate and perturbed states from tip eigenstates. So the solution of the time dependent schrödinger equation can be written as follows

$$\psi(t) = e^{-it\epsilon/\hbar}\psi + \sum_k a_k(t)\phi_k \tag{2.2}$$

Where the sum is over all the tip bounded states. The coefficient $a_k(t)$ is the result of projection of $\psi(t)$–$e^{-it\epsilon/\hbar}\psi$ into the tip state space as in $a_k(t) = \langle\phi_k|H - H_{tip}|\phi_k\rangle$. Because the tip's bound states do not span the whole space, the (Eq. 2.2) is only an approximate solution. Then the approximate solution satisfies the time-dependent schrödinger equation.

$$i\hbar\frac{\partial}{\partial t}\psi(r,t) = H\psi(r,t) \tag{2.3}$$

$$= e^{-it\epsilon/\hbar}(H_{sam} + (H - H_{sam}))\psi + \sum_k a_k(t)(H_{tip} + (H - H_{tip}))\psi \tag{2.4}$$

Then we relate this equation with the partial time-derivative of $\psi(t)$ as in $i\hbar\frac{\partial}{\partial t}\psi(r,t) = \varepsilon e^{-it\varepsilon/\hbar}\psi + i\hbar\sum_k \frac{d}{dt}a_k(t)\phi_k$. The resulting equation is obtained by ignoring the term proportional to $a_k(t)$, since the value of $a_k(t)$ begin with 0 and remain small for short period of time t. The resulting equation of $a_j(t)$ is written as follows,

$$i\hbar\frac{d}{dt}a_j(t) = e^{-it\varepsilon/\hbar}\langle\phi_j|H - H_{sam}|\psi\rangle + E_j a_j(t) \tag{2.5}$$

The solution of this differential equation can be obtained with the boundary condition $a_j(0) = 0$.

$$|a_j(t)|^2 = \frac{4sin^2(t(E_j - \varepsilon)/2\hbar)}{E_j - \varepsilon}|\langle\phi_j|H - H_{sam}|\psi\rangle|^2 \tag{2.6}$$

This is the main part of the transition probability and can be rewritten as total scattering rate as

$$\sum_k P_t(E_k - \varepsilon)M^2(\phi_k, \psi) \tag{2.7}$$

where $M^2(\phi,\psi) = |\langle\phi|H - H_{sam}|\psi\rangle|^2$ and $P_t(x) = sin^2(tx/2\hbar)/x^2$. With the help of Fermi's golden rule, the main contribution of the current comes from the interval $-eh/t + \varepsilon < \epsilon < 2h/t + \varepsilon$. Then the sum over the narrow interval is similar to the average value over the range. so we can approximate it as follows

$$\sum_k P_t(E_k - \varepsilon)M^2(\phi_k,\psi) \tag{2.8}$$

$$\sim M^2(\psi) \sum_{k:|E_k-\varepsilon|<2h/t} P_t(E_k - \varepsilon) \tag{2.9}$$

$$\sim M^2(\psi)\rho_{tip}(\varepsilon) \int P_t(E)dE \tag{2.10}$$

This formula gives the rate at which electrons in the sample state are transferred into tip states of similar energy levels. However, the scattering can only occur when there is unoccupied tip state. So the Fermi-Dirac statistics comes into play and the integral gives finite value of $\frac{2\pi}{\hbar}$. Then the scattering rate from sample to tip state becomes

$$(1 - F_{\mu_t,\theta(\varepsilon)})\frac{2\pi}{\hbar}\rho_{tip}(\varepsilon)M^2(\psi) \tag{2.11}$$

where

$$F_{\mu_t,\theta}(x) = \frac{1}{e^{(x-\mu)/k_B\theta} + 1} \tag{2.12}$$

The (Eq. 2.11) tells us scattering rate from sample to tip. The scattering from the tip to sample can be found in a similar manner. To obtain the net current from this scattering rate, the information about the occupancy of states should be included. With the Fermi-Dirac statistics, at the temperature θ, the tunneling current I between tip and sample can be written as follows.

$$I = \frac{2\pi e}{\hbar}\sum_n \{F_{\mu t,\theta}(\varepsilon_n)(1 - F_{\mu s,\theta}(\varepsilon_n) - (1 - F_{\mu t,\theta}(\varepsilon_n)F_{\mu s,\theta}(\varepsilon_n)\}\rho_{tip}(\varepsilon_n)M^2(\psi_n) \tag{2.13}$$

Or a more simplified version of this formula is the zero temperature approximate version. At the zero temperature, the Fermi-Dirac function $F_{\mu,\theta}(x)$ becomes the Heaviside

function and the tunneling current becomes

$$I = \frac{2\pi e}{\hbar} \sum_{n:\mu_a<\varepsilon_n<\mu_b} \rho_{tip}(\varepsilon_n) M^2(\psi_n) \tag{2.14}$$

Or the sum can be approximated with the average value of sample density $\rho_{sam}(\varepsilon)$ of state over the summing range. The integral form of the tunneling current at low temperature can be obtained as follows.

$$I = \frac{2\pi e}{\hbar} \int_{\mu_a}^{\mu_b} \rho_{tip}(\varepsilon) T(\varepsilon) \rho_{sam}(\varepsilon) d\varepsilon \tag{2.15}$$

where $T(\varepsilon)$ is the average value of $M^2(\psi_n)$ over the summing range.

This equation emphasizes the equally important roles of sample and tip. The tunneling current is the convolution of both tip and sample states. And it adds more features to the Tersoff-Hamann approach like the change of barrier tunneling probability (by the difference of workfunction between tip and sample or by electric field induced by relatively higher bias). So this model can generalize our view about the tunneling junction to the three important factors (tip, sample and barrier).

2.3 Tunneling Barrier Modeling

2.3.1 WKB Approximation

As seen from the (Eq. 2.15), proper modeling of tunneling barrier enables us to have more exact prediction about the tunneling spectroscopy. The most popular approach to the behavior of tunneling is Wentzel-Kramers-Brillouin (WKB) approximation. It is general method for finding mathematical approximate semi classical solutions to linear partial differential equations which are quantum mechanical equations. In this approximation the solution of partial differential equation is assumed to be in the form as follows.

$$y(x) \sim exp[\frac{1}{\delta} \Sigma_{n=0}^{\infty} \delta^n S_n(x)] \tag{2.16}$$

In the limit $\delta \to 0$, the dominant term in second order linear partial equation (as in the case of schrödinger equation) is the second derivative. With proper assumptions in the magnitude of δ, the second order differential equation can be representatively expressed as simple Eikonal type equation as $S'^2 = Q(x)$, and its solution is $S_0(x) = \int_{x_0}^{x} \sqrt{Q(t)}dt$.

2.3.2 Single Barrier Tunneling Junction

By applying the WKB approximation in tunneling barrier, the $Q(t)$ is then corresponding kinetic energy inside the tunneling barrier. Because the classical kinetic energy inside the barrier is negative (which is impossible in classical mechanics), the integrand is imaginary for the generalized wavefunction approach of quantum mechanics. So the exponent of the form $i \int dx \sqrt{\frac{2m}{\hbar^2}(V(x) - E)}$ is now the phase acquired by tunneling the barrier through. Note that this conclusion is not valid at the classical turning point because the normalized form of this exponent diverges at the turning points. But this factor is good approximate solutions in the region away from the barrier. So the tunneling probability between the barrier is precisely predicted by consider this approach. Since the kinetic energy inside the barrier is negative, the square root of the kinetic energy is now has pure imaginary parts. Then the resultant exponent becomes real value which gives finite possibility to find particles across the barrier. It expresses the probability to tunneling through the barrier or coupling strength between electron states of each side of the barrier. Then we can define coupling strength D as.

$$D = exp[-\int_{x_a}^{x_b} \sqrt{V(x) - \epsilon}dx] \tag{2.17}$$

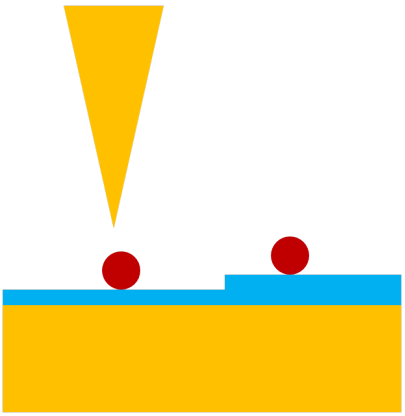

Figures 2.1 **Schematic Diagram showing Typical Double Barrier Tunneling Junction** - The sample under examination (red dot) is sandwiched by two metallic electrodes (tip and sample). Two barriers are depicted as vacuum and thin insulating layer (blue)

2.3.3 Double Barrier Tunneling Junction

In the case of decoupling layer in STM junction, the system often modeled as Double Barrier Tunneling Junction (DBTJ). Since the requirement of conductivity in STM experiment often resulted in hybridized electronic state from conduction electron from the substrate, thin layers of insulator film is typically used as decoupling layer. Though the electron can tunneling through the insulator film and enables STM experiment, the system is modeled to have two distinct barriers and complicate the situation. By applying the WKB approach to each barrier, we can write the corresponding rates as

$$W_1 \sim N_t(1 - f_1)D_1 \tag{2.18}$$

$$W_2 \sim N_t f_1 D_2 \tag{2.19}$$

where D_1 and D_2 are the corresponding coupling strength of each barrier.

$$D_1 = exp[-\int_{x_a}^{x_b} \sqrt{V(x) - \epsilon} dx] \tag{2.20}$$

$$D_2 = exp[-\int_{x_a}^{x_b} \sqrt{V(x) - \epsilon} dx] \tag{2.21}$$

Here N_t means the electron concentration in the middle of the barrier. For the case of steady current through the barrier, the rates w_1 and w_2 should be the same. In this assumption the f_1 term should be satisfy the relation $f_1 = \frac{D_1}{D_1+D_2}$ which yields the following modeling of tunneling current.

$$I = \int_0^V \frac{D_1 D_2}{D_1 + D_2} D_m(\epsilon) d\epsilon \tag{2.22}$$

where $D_m(\epsilon)$ is the density of states in the middle region between the two barriers.

2.4 Scanning Tunneling Spectroscopy

2.4.1 Local Density of States

The differential conductance of tunneling current is often interpreted as Local Density of States (LDOS) of the sample. Under the approach of Tersoff-Hamann, the derivative of the tunneling current is proportional to the sample LDOS.

According to the Tersoff-Hamann approach, the tunneling current only comes from sample density of state and the most important interpretation of STS can be deduced. E.g. STS is proportional to the sample local density of state (LDOS).

$$\frac{dI}{dV} \propto \rho(\vec{r_0}, E_F) \tag{2.23}$$

This expression has two important limits.

- It omits the details of the tip wavefunction. For example, if the tip has higher order symmetry other than s-symmetry or non-constant structure in its density of states, then this formula is inapplicable.

- The workfunction of metallic tip and sample is assumed to be identical and their formation of detailed structure in tunneling barrier is neglected. So in this Tersoff-Hamann approach, change of barrier height and the resultant change of tunneling probability are not reflected.

The workfunctions of tip and sample surfaces are generally different, but in this Tersoff-Hamann approach we assumed the same workfunction for sample and tip. And it also has no details about tunneling barrier of each system.

Despite of these limitations, (Eq. 2.23) offers first approximation to STS result. From the fact that STM tip wavefunction is generally unknown in experimental situation and altering frequently, the simplification of tip wavefunction has strength. Almost every DFT codes today use this simple picture to convert its calculated result to simulate STM images or STS mappings, because of the difficulty in assuming specific tip condition. In realistic modeling of tunneling junction, however, possibility of complicated tip electronic structure or variation of tunneling barrier (especially in high bias) should be considered.

2.4.2 Spatial Variation

LDOS of specific atomic site is obtained by one sweeping of bias voltage. We can repeat this spectroscopy after we reposition the tip over the new site of interest. By applying the procedure over the entire surface, we can obtain the spatial variation of LDOS of the surface. The capability of obtaining the spatial variation of the spectra with atomic resolution is the most important feature of STM.

Chapter 3 Experimental Techniques

We deposited QD solution onto the substrate by pulse injection method. The method has some advantages over previous deposition methods like drop casting or dipping. The sample surface can be kept in Ultra High Vacuum (UHV), so the surface shows atomically clean surface with QD.

3.1 Pulse Injection Method

3.1.1 Previous QD Deposition Methods

Typical sample deposition methods in vacuum can be summarized as follows

- Electron Beam Evaporation
- Thermal Evaporation
- Laser Ablation
- Sputtering Deposition
- Chemical Vapor Deposition

But these methods are inapplicable to QD deposition. Some of these methods introduce excessive heat during the deposition process through direct heating (thermal evaporation), electron bombardment (electron beam evaporation) or photon energy (laser ablation). With the heat energy, QD cannot sustain the original nano structure and will be eventually evaporated into disassembled fragment. And highly energized ions used in sputtering process will also destroy the nano structure of QD. And because QD has massive molar mass, it cannot be in gas phase which is required for

chemical vapor deposition method. So these typical procedures are hard to be applied in QD deposition.

Instead of the vacuum deposition methods, QD are introduced onto substrate from outside of the vacuum chamber. Previously studied QD deposition methods can be listed as follows

- Drop Casting
- Sample Dipping
- Contact Printing

The first two methods are not quite different. They use the formation of chemical bonding between sample surface and QD. The substrate contact the QD solution directly by dropping a drop of the solution in "drop casting" method. Or sample is being immersed in the QD solution for a period of time. QDs are known to make bonding with some surfaces like Highly Ordered Pyrolytic Graphite (HOPG). And for inert surfaces like gold which make no chemical bonding with QD, chemical treatment is needed to attach QD to the surface. So the formation of Self Assembled Monolayer (SAM) with alkanethiol molecules is used to alter the chemical property of the gold surface. The thiol functional group makes covalent Au-S bonding and then the other end of the SAM molecule makes chemical bonding with QD surface ligand. With this method various studies are produced on gold surface.

However the drop casting or dipping method has two limits. Firstly, to contact the QD solution, the sample should be go outside of the vacuum chamber, so chemically reactive substrates are easily contaminated by contact with ambient gas or even impure gas molecules in controlled environment. So these methods only can applied to relatively inert surfaces like HOPG or gold. Secondly, the choice of substrate is

very limited to surfaces which make chemical bonding with QD ligand. Since typical organic ligands like TriOctylPhosphineOxide (TOPO) have non polar property, they usually make no strong bonding with surface atoms. When there is only physisorption rather than chemisorption, then QD cannot maintain the bonding during the deposition or rinsing procedure. So these limitations hinders the freedom in choice of substrate and HOPG and SAM covered gold surface are mainly studied.

The restriction that QDs cannot be deposited on surfaces which make no chemical bonding with ligand, is overcame by recent progress of contact printing method. In this method, QDs are coated on top of PDMS surface by spin coating and then the layer is transferred to the target substrate by direct contact with controlled force and speed. With the method, it was possible to transfer QDs to device type substrate or bare gold surface. In principle, this method is applicable to any type of substrates. Though the limited choice of substrate is overcame by the method, there are still problems of contamination from violent process and it has relatively poorer sample quality than drop casting as shown in STM experiments.

3.1.2 Previous Results of Pulse Injection

The pulse injection method is originally known to have applications in gas dosing into a vacuum chamber. The pulse valve is a electromagnetically driven coil valve which can be operated from few hundred microsecond time scale. The valve opening is controlled by electric pulse signal from control electronics. During the short period of valve opening time, it can spray source material into the vacuum chamber. By control the length, frequency and duty cycle, the dosing amount can be controlled. Though it uses gas or solution which is relatively dense material for vacuum deposition, it has no significant influence on base pressure level since it is operated in fast and controlled manner. And samples can be deposited on the substrate which is kept in vacuum

environment, so the sample has no contact with ambient or other impure gases. This also has some advantages over other solution contact methods.

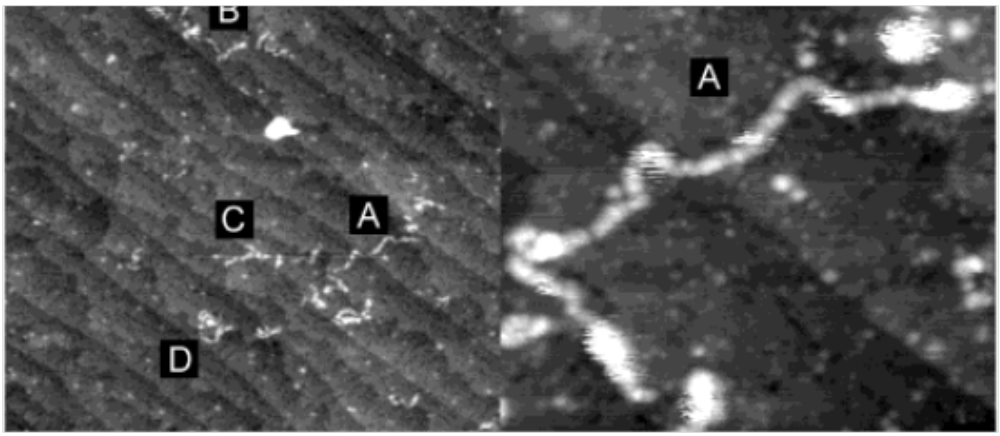

Figures 3.1 **Conducting Polymer on Silicon surface** - conducting polymer is deposited on hydrogen terminated Si(100) surface with pulse injection method[56]

The pulse valve has been applied to the deposition of nanosize materials in solution, since the demonstration of conducting polymer deposition which is impossible to evaporate by traditional evaporation methods[56]. Another famous application can be found in DNA partial sequencing by STM[55]. They found that DNA deposition on metal substrate is possible and the resulting surface is free of contamination which enables the spectral identification of guanine nucleobase. Despite its limited use in these special cases and relatively poor surface condition[1] After the pulse injection, pulse valve finds its advantage with its unique ability of solution dosing. In particularly, the pulse injection method suffers less from contamination compared to direct solution contact methods. In this context, the pulse injection method is also advantageous in QD deposition, however there was no application in QD study as far as we

[1]the resulting surface of pulse injection method has relatively contaminated compared to traditional evaporated samples. But when compared with other solution contact methods, it has less contamination.

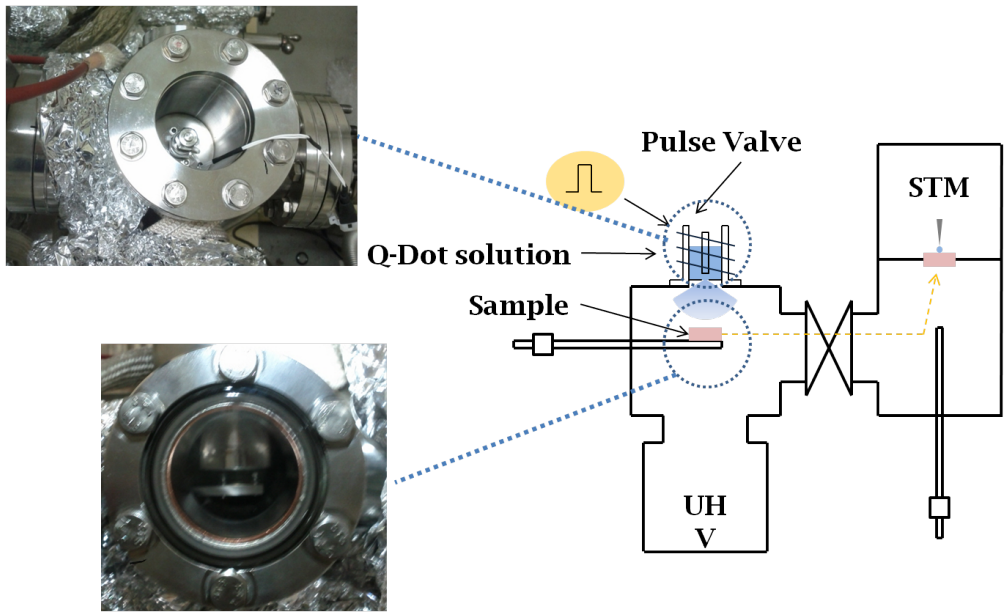

Figures 3.2 **Pulse Valve Deposition** - pulse valve is located on top of load-lock chamber (upper left). the pulse valve is re-entered to the vacuum side of the chamber to reduce the distance to the sample. The position of sample is observed through side view port(lower left).

know. So this experiment proves, for the first time, the validity of the pulse injection method in QD deposition. Some important points through our design of the pulse injection system can be summarized as follows.

- The distance between the valve and the sample should be as close as possible
- During the deposition process, vapors produced by the solution should be completely isolated from STM main chamber.
- QD solution should only contact the sample surface and unwanted deposition should be avoided.
- Instead of long duration pulse, we used short pulses repeatedly

The first point, the distance between the valve and the sample is critical to minimize the dosing amount of the solution. In the test experiments prior to QD solution deposition, only alcohol is loaded to the pulse valve and shots of alcohol vapor is sprayed repeatedly by the programmed control. The result is summarized in (Fig. 3.4). a series of ten pulses were conducted and the time trace of the chamber pressure is recorded with ionization gauge. As the pulse duration increases from 120 micro seconds to 150 micro seconds, the maximum pressure burst also increases from low 10^{-6} to 10^{-4} Torr. And the original base pressure of low 10^{-7} Torr is increased to high 10^{-7} Torr right after the 150 micro second pulses. And intermittent bursts of pressure which does not coincide with pulse injection moments are observed. This may the result of vaporization of injected alcohol from the surface which is in liquid phase right after the injection. From the results of the test, we can assure that QD solution injected should be carefully limited to minimum amount. Or the base pressure of the vacuum chamber can be increased and contaminations of vacuum systems like

sample heater, pumps, vacuum gauges and STM head would degrade the quality of the result. So we designed the pulse injection system to have minimum distance.

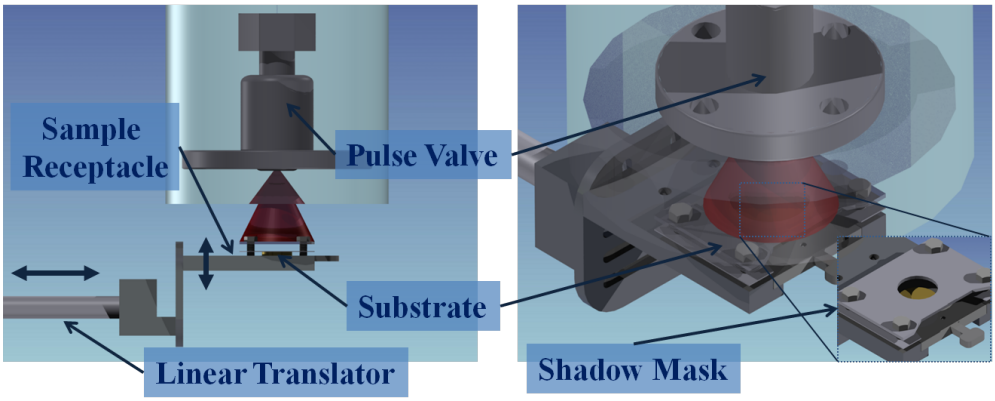

Figures 3.3 **Detailed Schematics of the Pulse Injection Method** - The pulse valve is at the air side of the top flange. The Top 4.5 inches Conflat flange is reentered toward vacuum side to reduce the distance between the pulse valve and substrate. The distance can also be adjusted by moving upward the sample receptacle. At the in front of the sample, a shadow mask prevents unwanted QD deposition to other parts of the sample holder.

The second and third points are also relevant to the minimization of chamber contamination. To isolate the solution vapor from the main chamber, we closed gate valve between the load-lock and STM chamber during the deposition. After the deposition, vaporized solvents are pumped by turbo molecular pump backed up by dry scroll pump. About few minutes of turbo molecular pumping is enough to recover the pressure of load-lock chamber to be able to re-open the gate to the STM chamber. Then the QD deposited substrate is transferred to the STM chamber by linear translator. Only the sample surface is exposed to the QD solution by covering other parts of the sample holder by shadow mask as shown in (lower right of Fig. 3.3). This reduces unwanted contamination of sample holder which will degrade the sample condition during the subsequent processes.

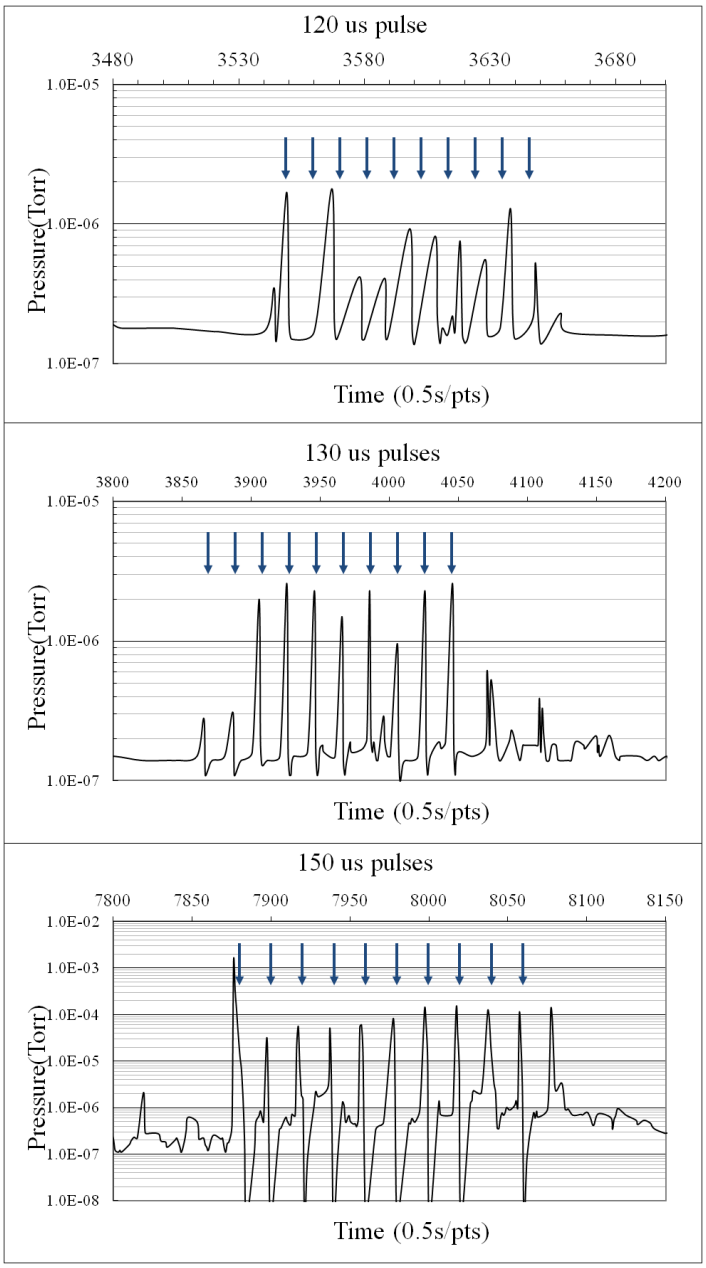

Figures 3.4 **Pulse Valve Test** - Pressure traces during series of 10 pulse injections repeated by 10 sec durations. The duration of the single pulse is stated at the title of each graph as 120, 130 and 150 micro seconds, respectively. The moments of valve opening is indicated by 10 consecutive arrows. The pressure burst is more frequent as the pulse duration increases and the base pressure is raised after the pulse injection of 150 micro seconds.

The last point arises due to the fact that the deposition is not uniform over the sample surface. When the deposition is done by few shots of ms injections, then the resulting sample has quite non uniform distribution of QDs. The STM topographic scans over the sample only show clean surface or thick covered QD layers. To obtain the desired homogeneous QD distribution, the deposition should be done by sequence of short pulses. The typical injection condition is about 300 micro seconds pulses with 30s duration time and 0.2 sec interval. This corresponds to duty cycle of about 1.5×10^{-3}, and the distribution of QDs are relatively uniform over the surface. Since the overall scan range of STM scanner is very narrow ($\sim 2\mu m$ for our scanner), the uniform distribution utilizes successful finding of QDs within a scan range.

The overall schematics and pictures of pulse valves used in this experiment are shown in (Fig. 3.2). The pulse valve is attached to the home-built STM system's load-lock chamber. At the top of the load-lock chamber the pulse valve is positioned inside the 4.5 inches Conflat flange. The pulse valve is reentered toward the vacuum side so that the distance between the sample and the valve can be reduced. To further reduce the distance, the sample holder receptacle is also adjusted toward the top flange from the original sample position as shown in (left of Fig. 3.3). And the modified sample holder receptacle also equipped with shadow mask to block the QD solution to the other parts of the sample holder (lower right of Fig. 3.3). The shadow mask prevents the introduction of excessive dose to the STM chamber.

3.1.3 Advantages

The advantages of using pulse valve can be summarized as following two aspects.

- Sample is not exposed to air throughout the whole deposition processes
- QD can be deposited on any kind of surfaces, regardless of its chemical property

In case of chemically reactive surface, the first one is of great advantage. Many substrates form oxide layer or chemisorption in ambient environment as in case of silicon surface. As seen in previous report, conducting polymer is successfully deposited on silicon surface with pulse valve [56]. In our case, QD was deposited on three kinds of substrates, gold, nickel and hexagonal boron nitride thin film. The gold is noble metal and known to be chemically inert so it is often used as substrate of QD as seen in many previous reports. Nickel, however, is relatively reactive metal as it forms oxide layer in ambient condition. So imaging of QD deposited nickel surface is more challenging than the gold surface. Despite the formation of monolayer of solvent molecules on nickel, STM imaging is possible with pulse injection. That the QDs are successfully deposited on these two metal surfaces represent the fact that QD can be deposited on both inert and reactive metals as can be seen in figure (3.5).

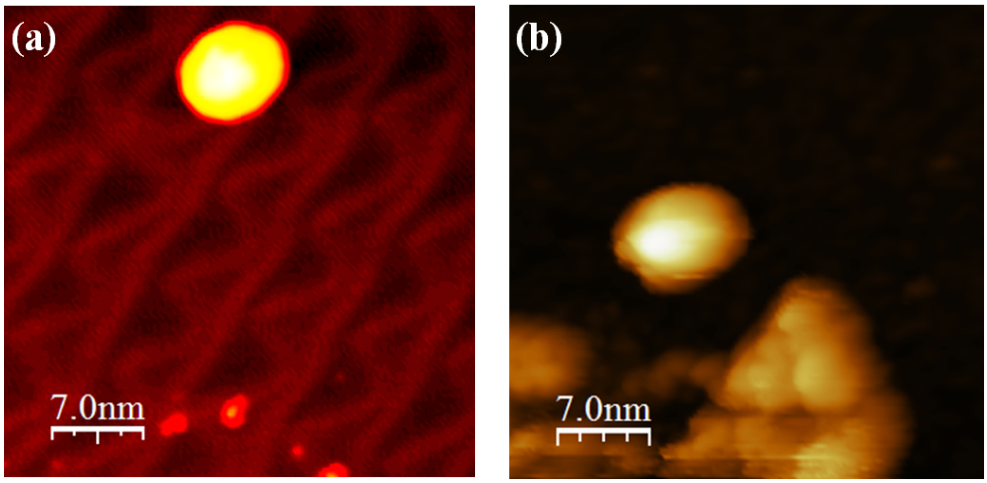

Figures 3.5 **QD Deposited on Au(111) and Ni(111)** - (a) single QD on Au(111) surface with herring bone reconstruction (b) single QD on Ni(111), note that the bare nickel surface is relatively contaminated with solvent molecules.

The image of QD deposited Hexagonal Boron Nitride (h-BN) film on Ni(111) surface proved that QD can also be deposited on inert insulator substrate. From the deposited QDs on different materials, it is clear that any specific chemical bonding between QD and surface is not important. Rather than chemisorption, physisorption is only required interactions between surface and QD to leave QD on the surface.

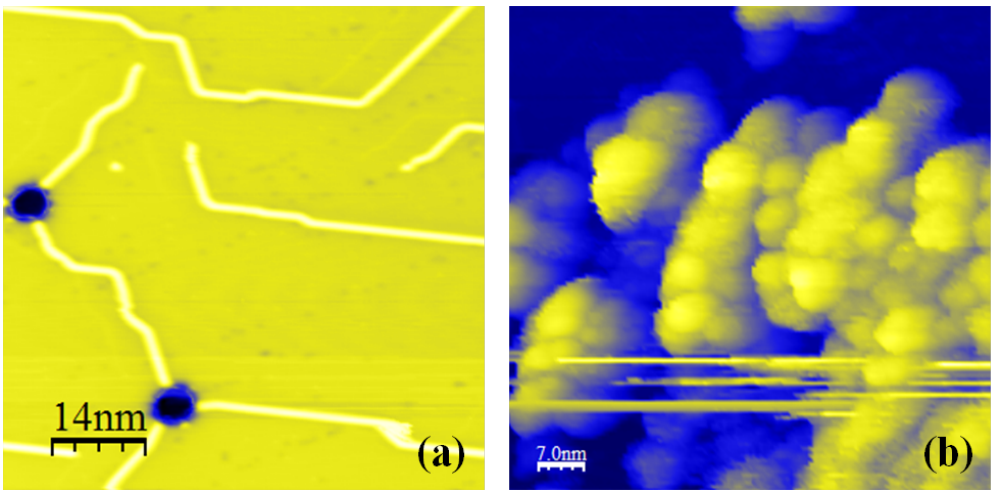

Figures 3.6 **QD deposited on h-BN surface** - (a) full coverage h-BN on Ni(111) with two types of defects(hole and line type) (b) QD aggregation formed by pulse injection

3.1.4 Limits

The disadvantages of pulse injection method can be summarized as following two aspects.

- Deposition is not uniform
- Impurity molecules are also transferred to the sample surface

The first one is critical in deciding the density of solution. As previously pointed out, non uniform distribution of QD on surface mainly limits the use of longer pulse.

Though we partly get over the problem by using series of short pulses, the distribution of QDs are not satisfactorily uniform. The problem of uniformity also prevents use of dense solution. In case of high density QD solution, then few counts of pulse injection is enough to obtain desired amounts of QD. But in this case, the resulting surface has the same uniformity problem. So to minimize this effect, the density of the solution should be kept dilute. The typical density of the solution used in the experiment was about 0.25 mg/mL which is 10 times diluted density compared to the density of the solution as purchased.

The second aspect requires exactly the opposite requirement on density of solution. If the QD density of the solution is too low, then impurity molecules in solution become comparable to QD density. It is because the impurity ratio of the solvent is constant though we change the ratio of QD in solution. So the more dense solution of QD is desirable. The impurity is solution is practically limited by quality of solvent used and typically few ppm of non-volatile impure material is contained when we buy solvent bottle from typical chemical suppliers (every solvents used are supplied by Sigma-Aldrich). A simple calculation emphasizes this aspect. If we compare molar mass between QD and solvent (DCM) molecule and weight percentage, then we can obtain their molar ratio which is calculated as 1 to 3000000. That means there are 3000000 solvent molecules per one QD molecule in the solution. And we know that 3ppm of non-volatile impurity and 100ppm of volatile impurity are contained in original DCM from the specification of Sigma Aldrich. This means that QD to impurity molecule ratio as 1 to 25 and 25 impurity molecules are deposited with one QD. In case of more dilute solution, this can be serious problem in the sense that the impurity density will be kept constant while QD composition is lowered. Then these impurity molecules are dominant in deposition process. So QD density should be denser than

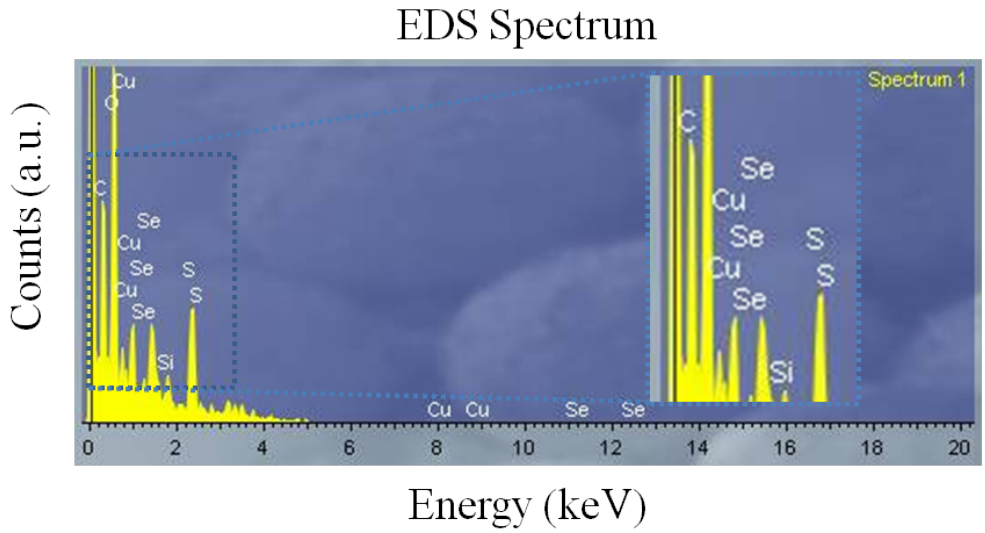

Figures 3.7 **Energy Dispersive X-ray Spectroscopy (EDS) Spectrum of QD deposited Silicon Sample** - EDS result shows various elemental composition of QD solution deposited silicon sample. Carbon, Copper, Silicon, Selenium and sulfur are the main contributed elements. Selenium and sulfur can be assigned to the core and shell of QD (cadmium is only detected in high energy EDS spectrum). Silicon is from the substrate itself and copper is possibly from gasket of vacuum chamber (copper gasket is used only for this test deposition on silicon which is conducted in another pumping stage). The major peak, carbon, can be assigned to the impurity molecules and capping molecules. From the ratio of intensity, carbon is major composition of QD deposited surface.

this practical limit. As can be seen in (Fit. 3.5) of nickel surface, unknown molecules are observed with QD.

To detect elemental composition of QD deposited samples, a test deposition on silicon was performed. The test was conducted in another independent vacuum chamber with the similar construction to the main experiments. In the EDS spectrum, carbon is the major elemental composition in the QD deposited sample. These carbon atoms can be assigned to both capping and impurity molecules. Note that the excessive amount of carbon cannot be explained only by the capping molecules, because bulk material of QD should surpass the surface material. We can assign the most of the excessive carbon atoms to the impurity from solvent. We also found that carbon based materials are used (various hydro carbonic amylenes) as stabilizer in DCM product from Sigma Aldrich. This problem mainly limits use of dilute density of QD solution.

With these two contrary considerations, we optimized the density of QD solution around 0.25mg/mL.

3.2 Ingredients of QD Solution

3.2.1 Core-shell Type QD

The most studied QD would be CdSe and core-shell type[39] derivatives of it. Since the CdSe QD is the first example of hot injection method and has many prominent properties and well understood electrical structures. The bulk CdSe material has energy gap of about 1.75eV. When the size of material becomes nanometer range then the energy gap changes. The energy gap increases with decreasing size of the crystal. Since the original band gap corresponds to the energy of red light, the increased energy gap can cover the entire visible spectral range[2]. So the CdSe is very promising in many applications using visible lights.

Right after the invention of the hot injection method, variations from the original synthesis made it possible to make core-shell type QDs. The most famous example would be ZnS shell. Since it has superior luminescent property than core type QD, core-shell type QDs are now mainly used in many applications.

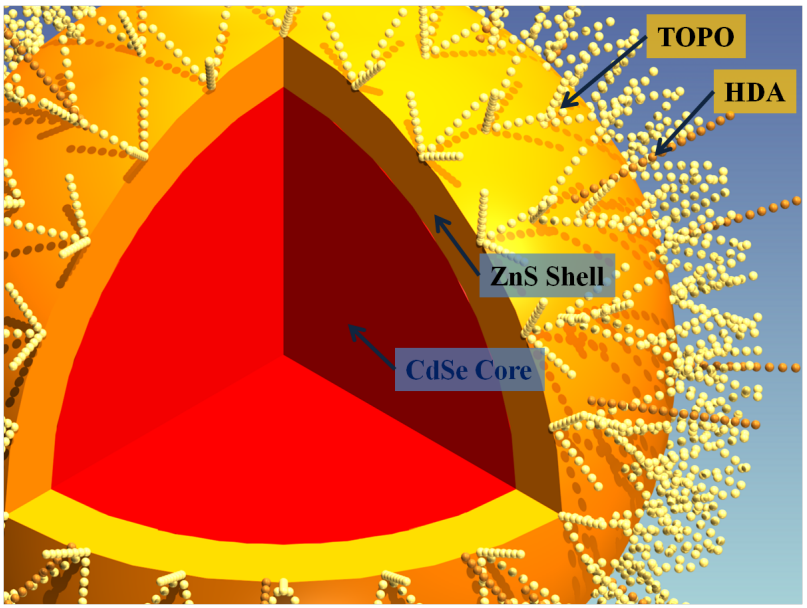

Figures 3.8 **Structure of QD used** - CdSe core is radially shelled by ZnS. The overall diameter of core-shell is 6.1nm and the QD is capped by two ligand materials, TOPO and HDA. The density of capping molecule is fictitious.

Typical capping molecules for CdSe are TriOctylPhosphineOxide(TOPO) and HexaDecilAmine(HDA). As can be seen in (Fig. 3.9), they have two distinct parts in a molecule, the bonding parts and carbon chains. The TOPO has phosphino and the HDA has amino functional group at one end. These functional groups make chemical bonding with QD surface since they have highly electronegative atoms. The HDA has carbon chain of 16 atoms at the other end and TOPO has three carbon chains of 8 atoms symmetrically spread to the other end symmetrically. These carbon chains

make no chemical bonding with QD surface nor to each other. So QDs capped with these molecules have non polar property because the covalently bonded carbon chains are only parts that are exposed to the outside. Because of the non polar property, the capped QDs are easily solved by non-polar solvents like toluene, hexane or chloroform. And the capping molecules also prevent QD from aggregation in solution by repulsing each other.

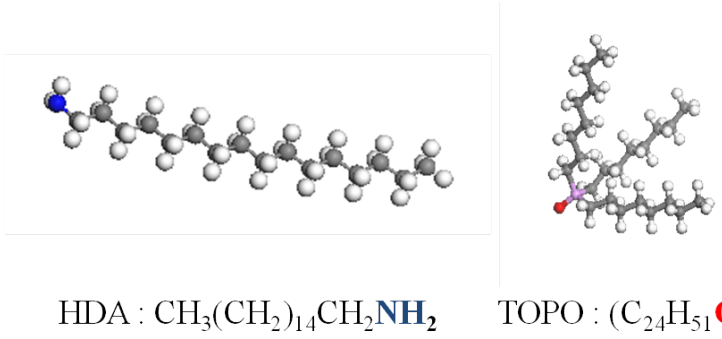

Figures 3.9 **Structure of Capping Molecules** - Two capping molecules of QD used in this experiment. The HDA has amino functional group at one end and sixteen carbon chains to the other end. The TOPO has phosphino functional group at the center and three carbon chains of eight carbons.

QD solution used in this experiment was purchased from Sigma-Aldrich, and it has CdSe core and ZnS shell with TOPO and HDA mixed capping layer. The diameter of core-shell is $\sim$ 6 nm and its PL spectrum is centered at 640 nm of red light. Its original solvent is toluene ($C_6H_5CH_3$) which are sometimes chosen for drop casting solvent. In STM experiment, however, even one monolayer of solvent molecule can be a hindrance for imaging and spectroscopy, so solvent material should be carefully chosen. So we tested pulse injection of several solvents without QD to characterize the property of solvent molecules on gold surface. The results and details will be described in the following chapter.

3.2.2 Properties of Deposited Solvents

Before we make QD solution, we deposited various solvents without QD to compare the effect of the solvent molecules on STM imaging. The solvents are loaded to pulse valve and injected on cleaned Au(111) surface. As can be seen in (Fig. 3.10), among DCM, toluene and DMSO, DCM proved its volatility and leaves no residue on the surface. Toluene made one monolayer of chemisorbed molecules which is not easily removed by mild annealing ($\sim 100°C$). DMSO shows worst performance among those. Especially DMSO has relatively high viscosity which results highly non-uniformly deposited surface.

3.2.3 Solvent Exchange

To exchange solvent of QD solution, typical cleaning of QD process was applied. In the procedure, QD solution is mixed with some amount of alcohol and then QDs form aggregation slowly. This precipitation process can be understood by reducing of repulsion of capping molecules by producing dynamic macro molecule of QD with surrounding alcohol molecules. To promote this aggregation, the mixed solution can be centrifuged for about 5 minutes at 3000 rpm. From this resultant liquid, the supernatant (which is partially clear) can be separated by pouring. The precipitate is now isolated QD in its solid phase. To further remove the residual solvent or alcohol molecules, we optionally pumped the precipitate out down to 10^{-6} Torr for a few hour with turbo molecular pump backed up by oil sealed rotary pump.

Throughout this procedure, we obtained isolated QD solid and it is resolved with DCM with the aid of sonication. And one of advantages of this procedure is that excessive amount of capping molecules can be extracted with alcohol.

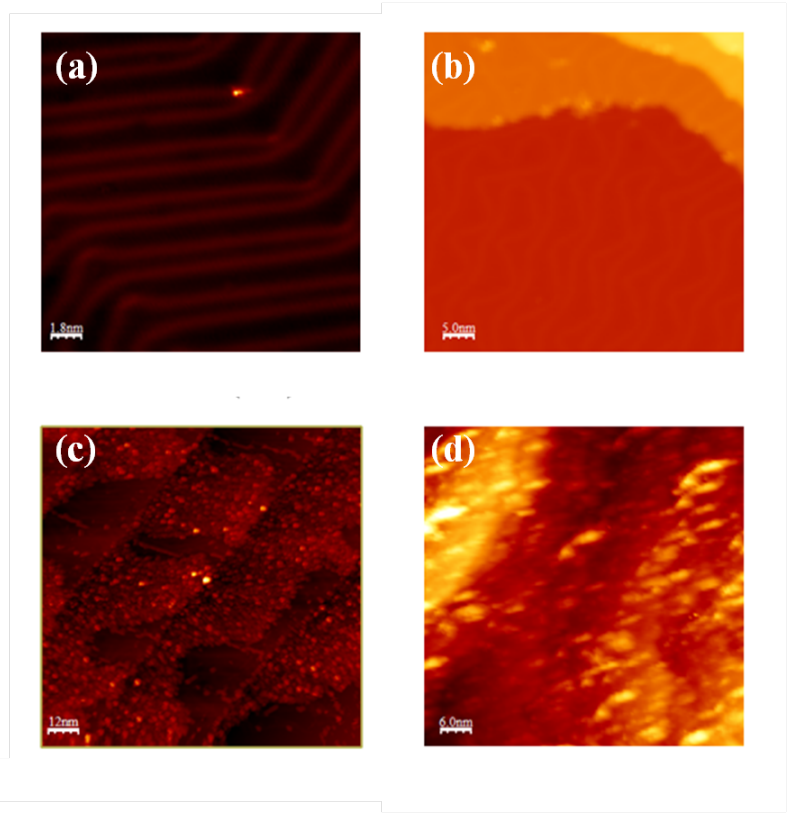

Figures 3.10 **Comparison of various solvents** - (a)Clean Au(111) surface with herringbone reconstruction (b),(c),(d) Au(111) surface after the injection of (b)DCM, (c)toluene and (d)Dimethylsulfoxide ,respectively.

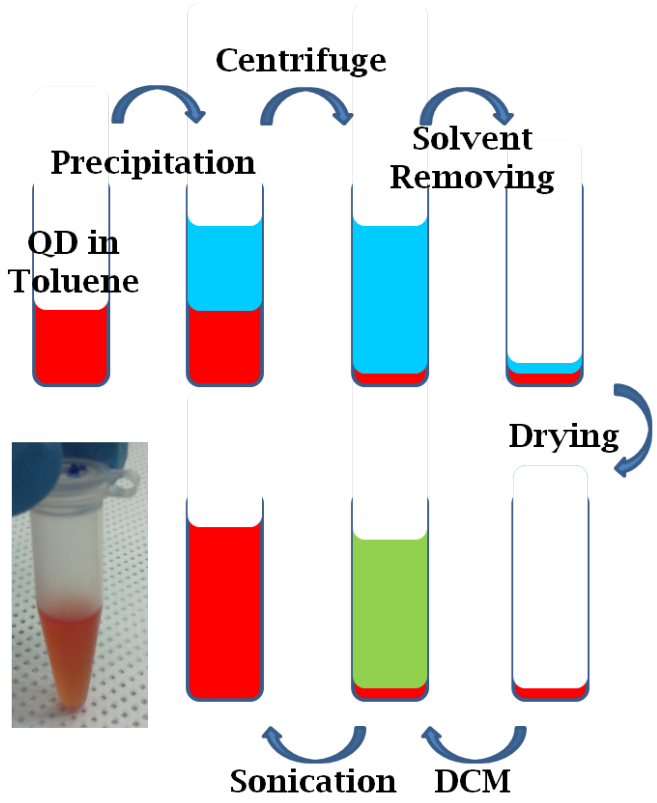

Figures 3.11 **Schematics showing method for solvent change** - solvent change process composed of (1) precipitation using alcohol (2) centrifugation to isolate QD (3) solvent removing and drying in dry nitrogen (4) ultimate drying in vacuum chamber for 1 hour (5) dissolve in DCM (6) sonication to help the dissolving. The typical solution after the exchange of solution is shown in the bottom left picture

3.2.4 Deposition Rate Determination

Deposition rate is determined by excessive dosing of QD solution on a macor surface. The macor is chosen for its white color which utilizes visual confirmation of deposited QD by its color. This procedure is done in independent pumping stage equipped with turbo molecular pump backed up by rotary pump. The actual deposition rate for STM experiment is selected in between $\frac{1}{1000} \sim \frac{1}{3000}$ from its color emergence.

3.3 Preparation of Substrates

3.3.1 Metal Substrates

Metal substrates (Au(111), Ni(111)) are cleaned by repeated cycles of sputtering and annealing procedure. These processes can be summarized as follows.

- Sputtering : Ar backfill (5×10^{-5} Torr), 1kV(Ni) 0.5kV(Au) acceleration Voltage, typically 10$\sim$20 μA sample current
- Annealing : electron bombardment, Au (500V, 5mA) Ni (1kV, 25mA)

These processes are appropriately repeated before every QD deposition and clean surface is periodically checked by STM imaging and STS measurement.

3.3.2 Insulator Substrates

hexagonal Boron Nitride Surface

Hexagonal-Boron Nitride (h-BN) surface is one of good candidates of decoupling layer in graphene based device which means it is chemically inert wide band gap insulator. And h-BN surface can be formed by thermal decomposition of borazine ($B_3H_6N_3$) gas on various metal surfaces, so high quality h-BN thin film can be obtained through vacuum process. We used Ni(111) substrate to grow h-BN thin film.

The Ni(111) surface is pre-cleaned by repeated sputtering-annealing cycles, then it is kept at high temperature ($\sim 800°C$) during borazine gas deposition. The representative structures of monolayer h-BN film are shown in (Fig. 3.12).

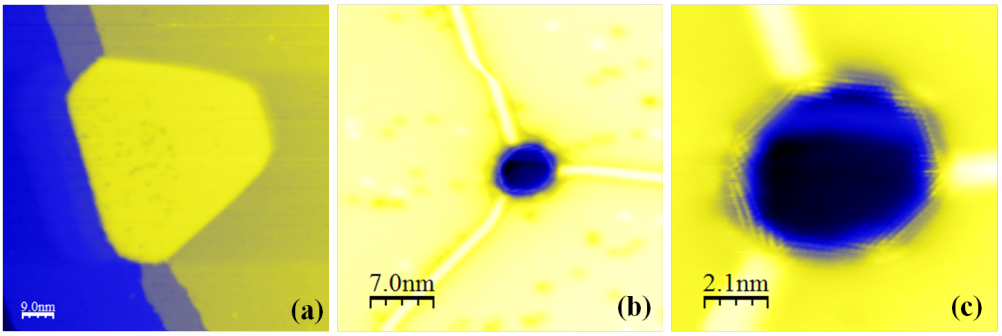

Figures 3.12 **Images of h-BN on Ni(111)** - (a)h-BN island on Ni(111) which has edges aligned to crystallographic directions (b)full covered h-BN with line type domain boundary and hole type defect (c) magnified image of hole type defect shows atomic structure of edge, note that only nitrogen atom is visible in the image for its high electron density

Chapter 4 Electronic Structure of QD

4.1 Imaging QD with STM

4.1.1 Determination of Tip Sharpness

In most applications of STM, the exact shape and size of the tip are difficult to be determined and even unnecessary. Since the most of the tunneling process occur through the very end of the tip, i.e. few end atoms, it is satisfactory to know the details of the tip at the sub-nanometer scale. Sometimes functionalization of the tip end with various atoms or fragments utilizes determination of exact wavefunction of the tip. So this information about formation of few tip end atoms helps to interpret the STM results properly. In this context, the tip shape in nano-meter scale or some hundreds of atoms has no importance in STM measurement for most cases. This aspect is also emphasized by the localized nature of tunneling phenomena. In QD measurement, however, the situation is totally different for the large size of QD.

As we pointed out in the previous section, the measured lateral sizes of isolated QDs show large size variation. It ranges from 1.5 to 2 times the QD size. This rather large distribution of the size cannot be explained by the QD size variation, since the variation is known to have approximately normal distribution with 0.73 nm standard deviation and 6.3 nm average and that is confirmed by PL emission spectra. This means that 75 % of QDs are in the range of 5.57 7.03 nm and 98 $ of QDs are in 4.84 7.76 nm. So the variation in experimental imaging size is not the real distribution of QD sizes. That can be explained by the effect of the tip geometry, instead. The (Fig. 4.2) summarizes this effect with geometrical schematics. The size of the QD

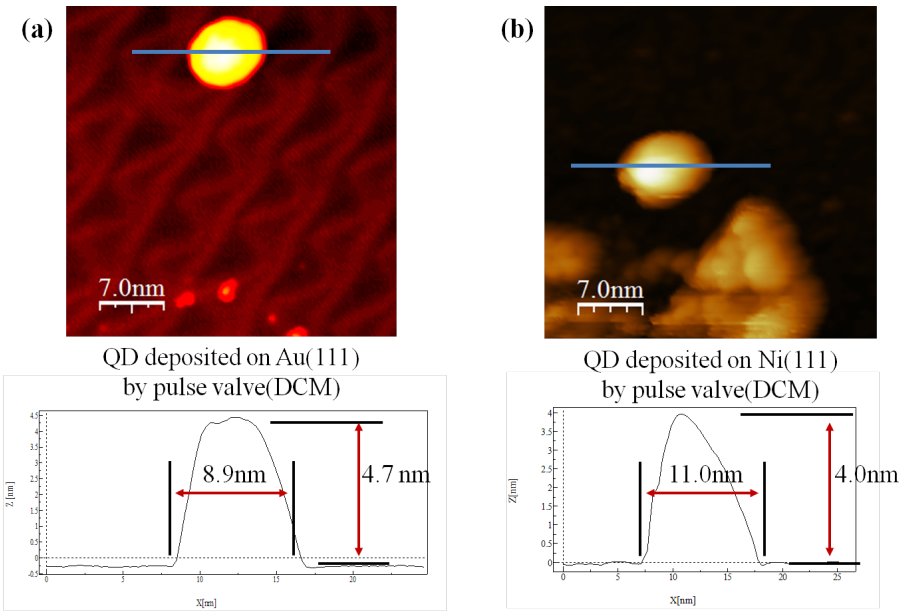

Figures 4.1 **observed single quantum dots on metal surfaces with height profiles across the QDs** - (a) QD on Au(111) (b) QD on Ni(111), note that the size of each QD is significantly different because of tip shape and radius, see text for details

is relatively big compared to that of typical STM experimental objects (i.e. single atoms, molecules, atomically thin layers, etc.). Then the tunneling process does not occur only from the end atoms, but also from other parts of the tip that contacts the QD. The idealized model in (Fig. 4.2) indicates that the tunneling process can be occurred from the side slope when it touches QD. When the tip side slope touches the QD, then feedback control of STM pulls the tip back. And the resultant image line is broadened by the lateral size of the tip at the scale of QD. The broadened topographic line is drawn as red curve in the schematic. Because the tunneling can only exist in sub-nanometer scale, this model intentionally ignores the tunneling gap between the tip and sample to simplify the situation. So QD and tips are rendered as hard solid that touches each other. Note that with the inclusion of the gap, it will magnify the imaging size of the QD. The red curve in (Fig. **??**) indicates the imaging size of QD in the direct contact scheme. With this simple model, the size of the tip radius of curvature and half cone angle (θ) can be related to the lateral imaging size Δ as follows through simple geometrical calculations.

$$\Delta = 2 \times \{\frac{R+r}{cos\theta} + (R-r)tan\theta\} \tag{4.1}$$

Where θ is the half cone angle of the tip in nanometer scale, and R and r are the radius of the QD and tip end, respectively. Since the lateral imaging size Δ and QD radius R are known factors, the remaining two variables of the tip have constraint with the relation. Though we cannot determine the two factors at the same time, it is possible to draw solutions of the two values. So we simulated the possible tip curvature as the function of the tip half cone angle. The relation of (Eq. 4.1) can be

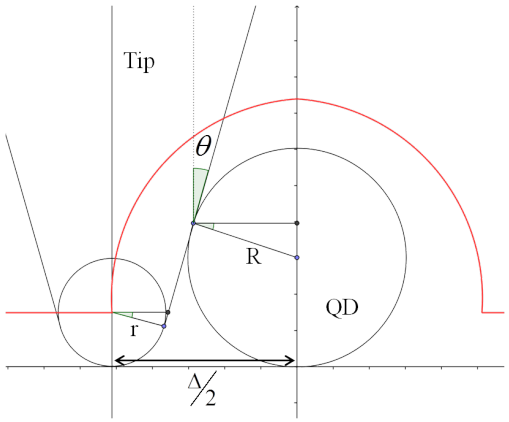

Figures 4.2 **Schematics shows image broadening of QD** - QD is typically larger than the STM probe tip. For the finite size of the tip end, QD is inherently broadened in image.

rewritten in r as the function of θ

$$r = \frac{\Delta cos\theta}{2(1 - sin\theta)} - \frac{R(1 + sin\theta)}{(1 - sin\theta)} \tag{4.2}$$

We draw the calculation result in (Fig. 4.3). The result represents the possible tip end radius as a function of half cone angle. The black curve shows the case such that the imaging size of the QD is 1.5 times of the original size. The result shows that 6 nm QD is imaged as 9 nm size if we have 1.5 nm radius and 0° half cone angle. Or more reasonable solutions are 1.0 nm tip end and 10° cone angle or 0.5 nm and 20°. Though we cannot determine the exact size of the tip, we can exclude the tip end radius larger than 1.5 nm and half cone angle larger than 22°. With this simulation, the QD image size of 8.9 nm in (Fig. 4.1) indicates that the tip end radius is smaller than 1.3 nm[1]. Another case with double sized image of QD can be seen in the orange curve of (Fig. 4.3). From this result, it is evident that QD image can be generally larger than the original size and the size and shape of the tip end in nanometer scale

[1]possible tip conditions are 1.3 nm end radius and 0° half cone angle, 0.87 nm and 10° or 0.43 nm and 20°.

is important in QD STM imaging.

To obtain the ideal tip end radius and shape, we carefully treated the tip end with several procedures. We used electrochemically etched tungsten tips and conducted typical treatment of electron beam heating and self sputtering after the introduction to vacuum chamber. With the processes, we removed the impurities or oxides at the tip end. Though the clean and metallic tip can be obtained through this treatment, the tip end radius and shape are not controlled with the process. So repeated indentations of the tip into clean Au(111) surface are performed until the ideal tip shape and size are obtained. The indentation is done by turning the feedback off and rapidly pushing the tip into the surface about 5 nm by adjusting the voltage to the z piezo. And then the tip is gradually pulled from the surface until the saturated current is back to the zero current. With the indentation process, we generally obtained larger z piezo set point which means the tip becomes longer after the indentation. The modified tip shape is checked by imaging of impurity particles and steep atomic steps on the Au(111) surface. And an electronic structure of the tip is also checked by tunneling spectroscopy on the gold. After this procedure, the tip is used for imaging and spectroscopy of the QD.

The indentation process is also performed after the imaging of QD, because the QD injected surfaces generally contains impurity or solvent molecules and they are easily transferred to the tip. Then they interrupted stable imaging and tunneling current measurement. So each time between the sample exchange, the tip condition is checked by scanning the clean Au(111) surface and the indentation is performed until the desired condition is obtained.

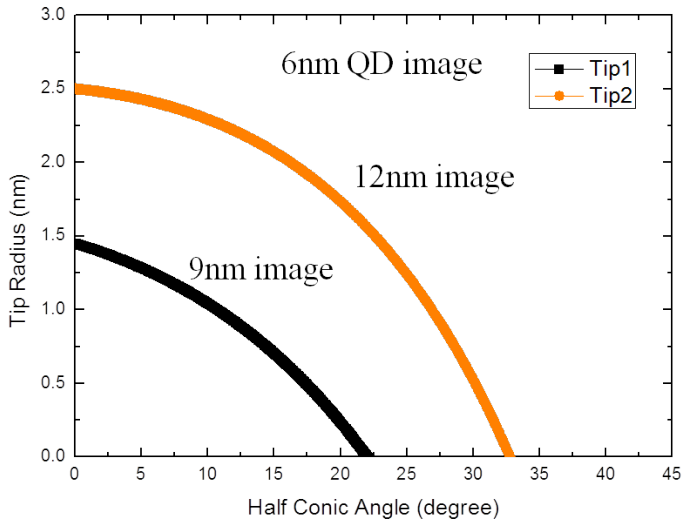

Figures 4.3 **Possible Tip Radius** - Two cases of 1.5 and 2 times of the original size are simulated with 6 nm QD diameter. The QD has imaging size of 9 nm with the tip of radius 1.5 nm or less according to the half cone angle. With the tip of 2.5 nm, the QD can be imaged as two times of the original size. Note that dull tips with large half conic angle ($> 33°$) will obtain the lateral QD size larger than two times of the original size.

4.2 Electronic Structure of QDs

4.2.1 Metal Substrates

STS measurement on metal substrates is obtained on isolated QDs or QDs at the edge of aggregation. An example of the isolated QDs are shown in (Fig.4.1). The exemplary STS spectrum of QD on metal surface is shown in (Fig. 4.1). Some notable features can be summarized as follows.

- Zero Conductance Gap
- peaks of hole and electron states corresponds to S, P and D symmetries
- Peak intensity is modulated by the conductance of the substrate
- Small size peaks inside the gap

The measured zero conductance gap of QD is about 1.8 eV. And some peaks of electron or hole levels can be assigned to the symmetry notations of S, P and D[35]. Though we can assign the origins of these low lying states with envelope function approach as described in chapter 1, the details of the spectrum can only be obtained by rigorous calculations like DFT theory. So, to further confirm that the STS structure is from the QD itself, we compare the result with DFT calculation.

Generally the atom numbers in a QD is too large to be calculated in an ab-intio calculation. For example, approximate atom numbers of 6 nm diameter QD (which is used in this experiment) exceeds 2000. So DFT calculation of such a large system is almost impossible for limited resources or lack of computing power. To obtain the properties of large QD, we usually calculate small size QD and scale it up. Since the gap is the function of QD size, it can be obtained from an experiment or a calculation.

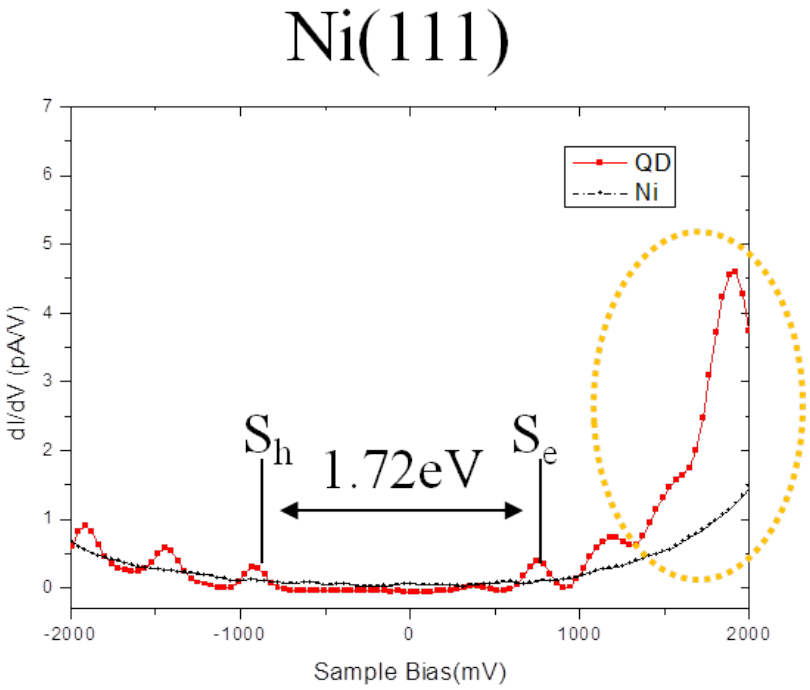

Figures 4.4 **Electronic Structure of QD on Ni(111)** - Gap between first electron and hole states is measured as 1.72eV, differential conductance of Ni(111) is plotted as dotted line. At positive bias, enhanced conductance influenced by high density of states of nickel substrate is visible (yellow dotted circle)

In (Fig. 4.5), theoretical calculation of gap as a function of the QD size is represented.

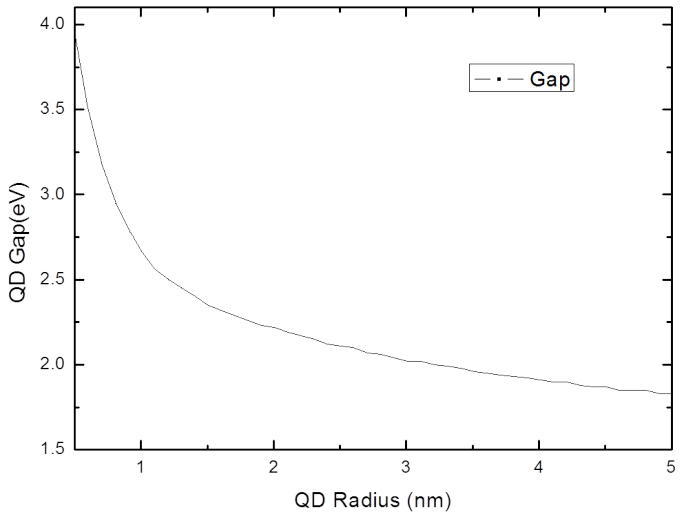

Figures 4.5 **Theoretically predicted Energy Gap** - Theoretical prediction of band gap as a function of the QD size from reference**??**. The result is calculated under the effective mass approximation. Though the calculation is done on CdSe core QD, it is approximately used as the scale factor of core-shell type QD gap in the text.

According to the gap variation, the DFT calculation result from reference**??** is scaled up. The calculation was done on 2 nm size core-shell type CdSe/ZnS QD. To compare the calculation with 6 nm QD experiment, we scaled the calculation by 2.04/2.64. The values of 2.04 and 2.64 eV are extracted from the gap values in (Fig. 4.5). The scaled result is shown in (Fig. 4.7). The theoretical prediction of the gap is agreed well with experimental gap size and peak positions of hole states also fit well.

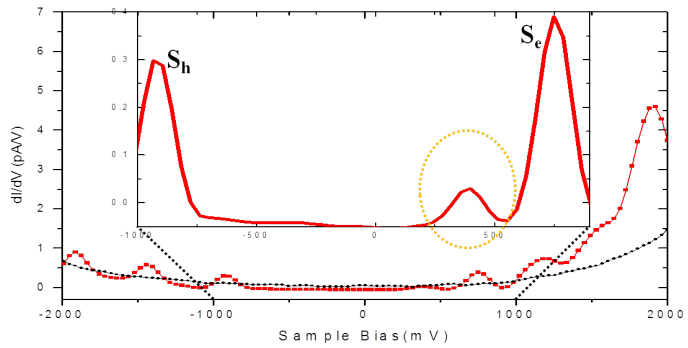

Figures 4.6 **Magnified View inside the Gap Region** - Additional state can be seen inside the gap region at 400 meV (inside the orange dot circle).

The noticeable differences of the comparison are that the structure of electron states are dissimilar to the calculation and state inside the gap is observed as in magnified view (Fig. 4.6).

At 400 meV in the gap, a state is clearly observed and there is an additional peak at 1.2 eV. The origin of the additional peaks is unclear now, but DFT calculations with some crystal defects show deviations from the pristine QD result. Though we cannot assign the peak to a specific type of defect, it is probable[27]. Sometimes the tunneling spectra show severely different STS from the predicted DOS as shown in (Fig. 4.8).

Another notable feature is peak intensity ratio between hole and electron states. According to the calculations, generally, hole states have relatively higher electron densities than electron states. The density of hole states implies the existence of heavy hole bands thus the hole bands show higher densities at the energy. However, the experimental results are not consistent with the calculations. On nickel surface, the differential conductance of the substrate at positive bias is higher than of the

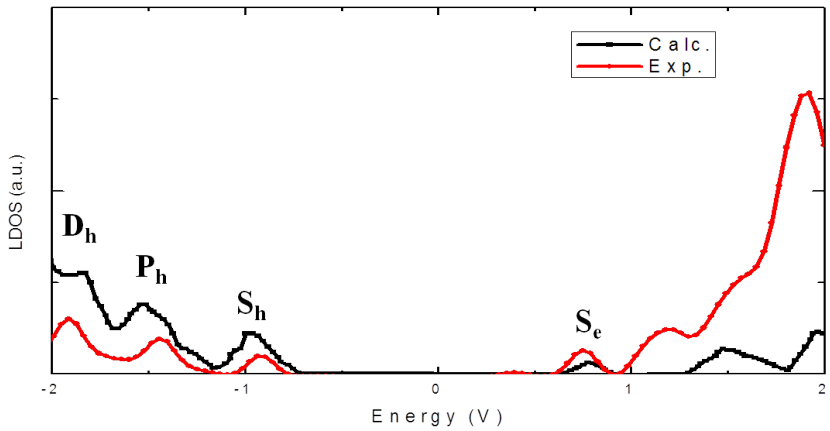

Figures 4.7 **Comparison between experiment and DFT calculation** - S, P and D symmetric states of holes coincide with the experimental data. However, electron states show additional peak at about 1.2 eV and exaggerated peak intensities. The increased peak intensity at the electron states coincide with the high tunneling conductance of the substrate nickel surface at positive bias.

negative bias. On this nickel surface, QD spectrum shows higher electron density at the positive bias. On the contrary, QD on gold surface shows higher density at negative bias, and the conductance of the gold substrate is also high at negative bias. With these results, the peak intensity reflects the conductance of the substrate as their background. This emphasizes the role of substrate conductance on QD spectrum. That is peak intensities in QD STS result are modulated by substrate conductance.

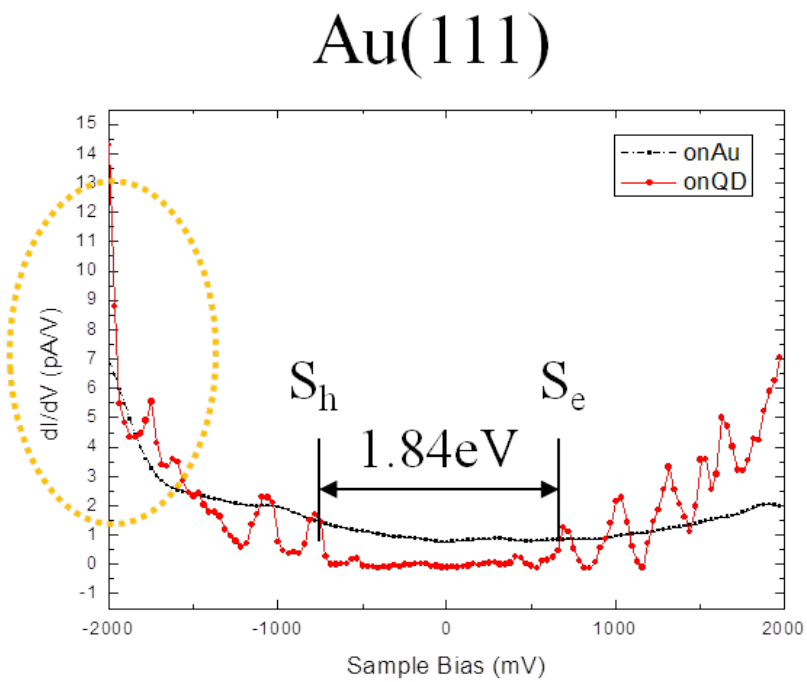

Figures 4.8 **Electronic Structure of QD on Au(111)** - Gap is measured as 1.84eV, differential conductance of Au(111) is plotted as dotted line. At negative bias, enhanced conductance influenced by high density of states of gold substrate is visible (yellow dotted circle)

To obtain the meaningful information from the peak intensity, we need to remove the effect of the metal substrates. That can be realized by a calculation including

the metal substrate atoms, but that is also an difficult task for the large size of the system. Or experimentally, QD deposition on insulating layer will decouple the QD wavefunction from the metallic states. In this context, the QD deposition on insulating layer has important meaning. The attempt to obtain the spectrum on thin insulating layer will be introduced in the next section.

4.2.2 h-BN Surface

Since STM requires conducting substrate, metallic substrate is essential to the experiment. However, when we observe target objects on metal substrate the hybridization of electron wavefunction complicates the problem. As we pointed out in the previous section, QD deposited on metal substrates shows strong modulation of LDOS by the conductance of the metal surfaces. And hence the specific intensities of each state are severely modified by the substrate conductance. To reduce the effect of metallic electron states, we need insulating decoupling layer on metal substrate. If the substrate is bulk insulating material, then tunneling current cannot pass through the sample. So few atomic monolayer of decoupling layer is required to perform the tunneling current measurement. Since the electrons from the tip can tunnel through the few layer of insulator, tunneling current measurement is possible. Then it is possible to measure the QD STS without the hybridization of QD states with the metallic states.

The h-BN surface attracts much interest for its inert property, wide band gap and easy formation of atomically flat surface. The h-BN surface is prepared as described in the previous chapter 3.3.2 and QDs are also injected by the same manner with the metal substrates. Since the pulse injection method is not dependent on the chemical property of the surface, the same conditions as in metal surfaces resulted in the similar density of QDs on h-BN surface.

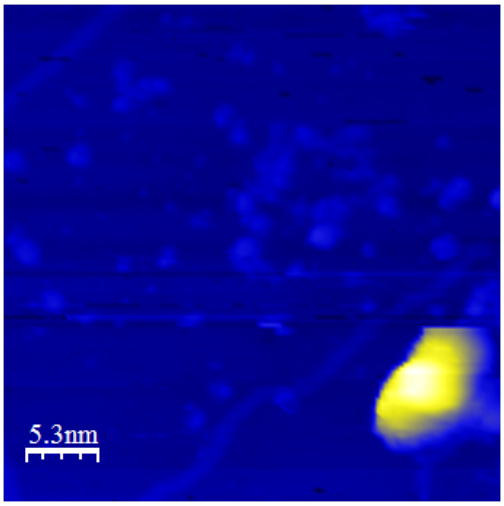

Figures 4.9 **Typical h-BN Surface after the Pulse Injection.** - Among the residual molecules, line type defects which are characteristic feature of h-BN surface on Ni(111) are observed. On the lower right part, an isolated QD is also observed.

The characteristic defects of h-BN surface of line and hole types (Fig. 3.12) are used as the indicative evidence of h-BN surface as in (Fig. 4.9). By the existence of the same defects before and after the injection, we can confirm that the h-BN monolayer is not damaged by the injected solution.

Though the h-BN surface is expected to be a good decoupling material for QD, the obtaining of tunneling spectra on QD/h-BN was not an easy task. Since the h-BN surface is known to be inert, residual molecules are also easily moved by tunneling current. The horizontal lines along the fast scan direction are noticeable in (Fig. 4.9) and the boundaries of QDs are fuzzy. So the tunneling current is usually unstable and difficult to acquire tunneling spectrum reproducibly. So STS spectrum of QD on h-BN surface would be possible by further removing of residual molecules.

As long as we know, this is the first attempt to deposit QD on decoupling layer. Though the stable measurement of spectrum on h-BN was not possible, this result

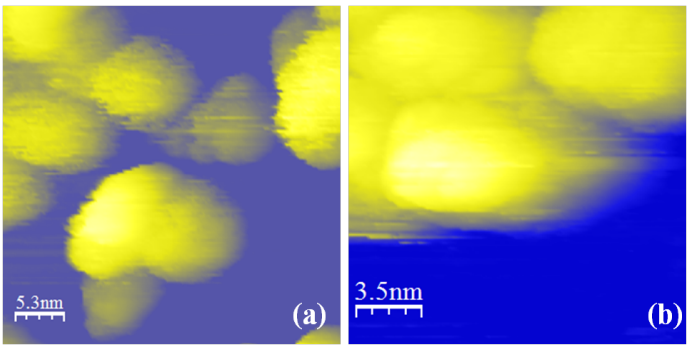

Figures 4.10 **pulse injected QD on h-BN surface** - Typical image of QD deposited on h-BN surface. The instability of tunneling current is reflected as horizontal lines and fuzzy boundary of QDs.

implies the possibility of QD deposition on insulating layers. The separation of QD states from the substrate implies the possibility of intact QD electronic structure measurement. And the wide band gap nature of h-BN also has advantages in photon detection from the QD STM junction, because the gap is much wider than the QD states, so the h-BN states have little influence on generation of photons. In this aspect, the first demonstration of QD deposition on h-BN layer will prove its value.

4.3 QD Aggregation

Despite well isolated QD is ideal for investigation of its own characteristics, such QD is rarely observed as in (Fig.3.5). Instead almost all QDs are found in aggregation commonly for all substrates (Au(111), Ni(111) and h-BN on Ni(111)) surfaces[44]. The formation of the aggregation seems to occur during pulse injection, because thermal diffusion of QD at room temperature is not probable for its massive number of atoms. And in the images taken before and after the mild heating process, QD aggregations are observed for the both. This excludes the possibility of aggregation by the post-heating process. So it is the result of dynamic diffusion of QD in solution during and

right after the pulse injection.

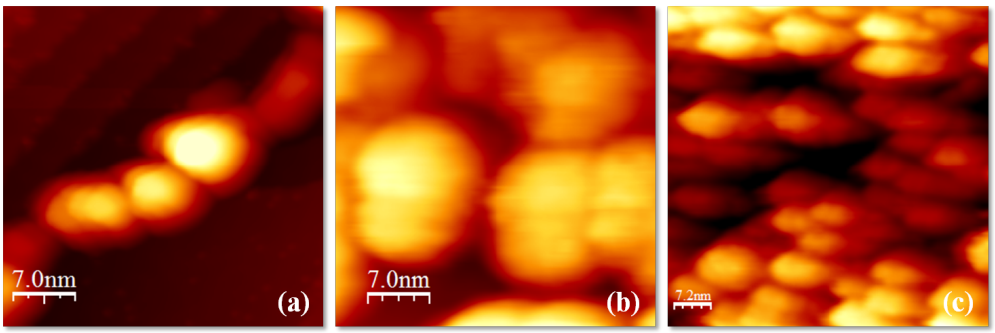

Figures 4.11 **QD aggregation on Au(111)** - (a) small aggregation of three QDs(b) magnified image of aggregated QDs (c) large scale view of QD aggregation

4.3.1 Metal Substrates

Typical images of QD aggregations are shown in (Fig.4.11) and (Fig.4.12). QD aggregations are commonly formed on both Au(111) and Ni(111) surface. But the rest bare metal surfaces show different characteristics, Au(111) shows modified herringbone structure(can be seen in (Fig.3.5 (a))) which is the evidence of abundant defect atoms, but no significant adatoms or molecules are observed. The modification of the herringbone structure is known in case of existence of defect atoms like sulfur**??**. On the other hand, Ni(111) is severely contaminated with solvent molecules. As in (Fig.4.12 (a)), nominal one monolayer of chemisorbed molecules are observed on the bare nickel surface. But their mixed feature (possibly solvent, excessive capping and impurity molecules) prevents the individual identification of the molecules.

Between the two surfaces, Au(111) shows relatively clean surface after the injection. Occasionally, on Au(111) surface, we can find capping ligand molecules. There might be on the Ni(111) surface, too. But the Ni(111) surface has too much chemisorbed molecules, so discrimination of capping molecules are almost impossible.

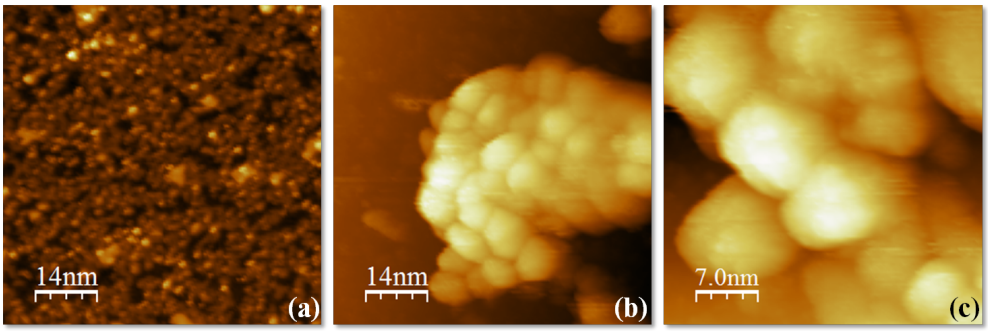

Figures 4.12 **QD aggregation on Ni(111)** - (a) Ni bare surface after the pulse injection, contaminated by mixture of solvents and capping molecules (b) aggregated QDs (c) magnified image

By the fact that the solvent, DCM, leaves no residues on gold surface, it is possible to image and observe the capping molecules and the result will be discussed in the next chapter.

4.3.2 h-BN Surface

Formation of QD aggregation on h-BN surface has no significant differences from metal substrates. But in detail, they exhibited relatively unstable tunneling current which is reflected as notable noises in image. (see (Fig.3.6 (b)) or (Fig.4.10 edge of each QD) For this reason, no stable STS spectrum is obtained.

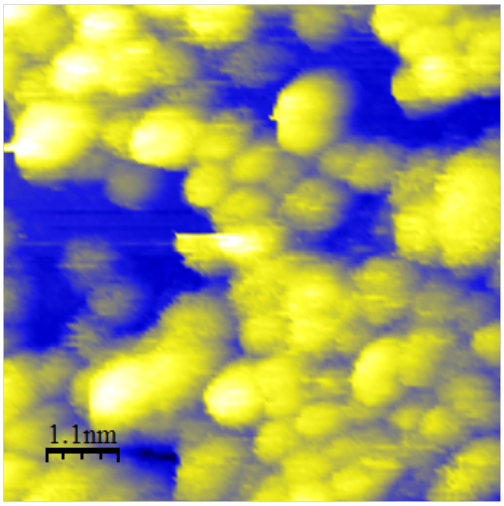

Figures 4.13 **QD aggregation on h-BN on Ni(111)** - The instability of tunneling current is reflected as horizontal lines and fuzzy boundary of QDs.

Chapter 5 External Trap States

5.1 Tunneling Spectra of External Trap States

Occasionally some QDs exhibit totally different spectrum from ordinary ones. An example of such a spectrum is shown in (Fig. 5.2) and for comparison the ordinary STS result is also shown in (Fig. 5.1). The most remarkable feature of that kind of spectrum is the existence of strong peaks inside the gap and positive sample bias. These peaks show much stronger intensity than the ordinary spectra.

We note that these states are different from defect states shown in (Fig. 4.6). As pointed out in the previous chapter, almost all QDs have small size gap states which are reasonable to assign as crystal defect states and they are confirmed by DFT calculations. Since the crystal defects are localized at the defect sites, their intensity cannot be much stronger than the original confined states' peaks. They only make some deviated peaks and change of the relative intensities from the original density of states. In this sense, the enhanced peak intensities of (Fig. 5.2) cannot be explained by the internal crystal defects. We assign this chapter to introduce possible mechanisms of this phenomenon.

The notable features of the spectra with the strong peaks inside the gap are summarized as follows.

- Strong peaks are observed from the gap through the positive bias region
- The peak intensity is much stronger than the ordinary QD confined states' peaks
- The detailed peak positions and shapes are different from QD to QD

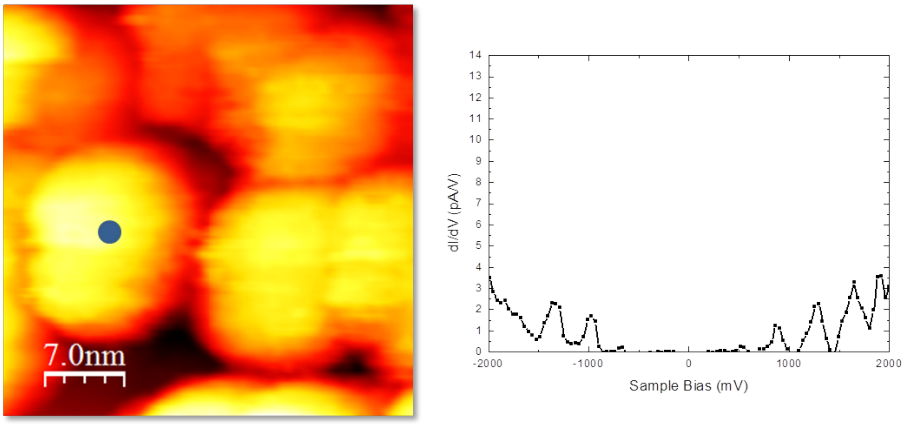

Figures 5.1 **STM topography image and STS spectrum from a QD** - The spectrum shows the ordinary gap feature and QD confined states. The set point current and bias are 200 pA and 2.5 V.

To find out the spatial variation of the observed peaks, we obtained a series of tunneling spectra along the center line of a single QD. The result is shown in (Fig. 5.4) as two dimensional map with color mapped by differential conductance. The result reveals the striking feature of the distribution of the observed states. As can be seen in the map, the states does not uniformly exist over the QD, but they are only observed on rather randomly spaced three points which are indicated by vertical red lines. In other words, the origin of the strong peaks is localized at specific sites on QD surface. So it is natural to introduce inhomogeneous QD surface condition to explain this phenomenon. And we will present some possible mechanisms in next section. Before that, some immediately noticeable features will be analyzed through this section.

1. The first noticeable feature of the states is the localization. The size of the localization can be estimated by the number of similar spectra near the sites. The strong peaks are observed over 2 or 3 spectra near the sites. From the fact that the

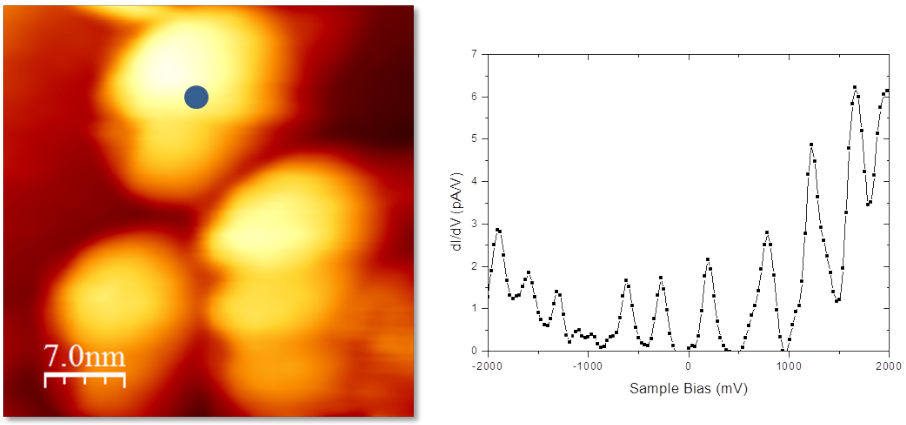

Figures 5.2 **STM topography image and STS spectrum from a QD** - The spectrum shows series of states from the gap to positive bias region. The set point current and bias are 100 pA and 2.0 V.

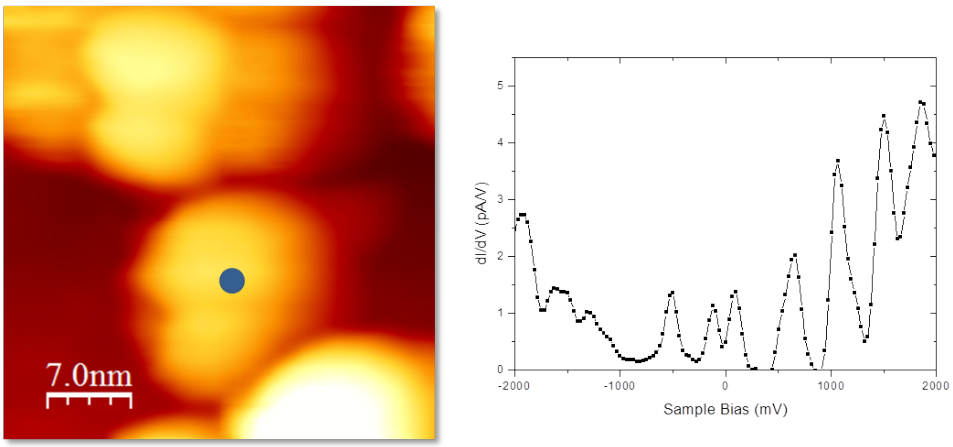

Figures 5.3 **Another STM topography image and STS spectrum with the strong gap states** - The set point current and bias are 100 pA and 2.0 V.

spacing between each point is 4.7Å, we can estimate the lateral localization size to be about 1.4 nm or less. Then it is natural to compare the size with lateral size of the capping molecule. Though the STM topography image did not show the existence of capping molecules directly, it is improbable that the capping molecules are removed by pulse injection or mild post heating procedure[1]. And evidence about the existence of ligand is found in estimation of barrier thickness between QD and metal surface which will be presented in chapter 6. The estimation of the thickness corresponds to the vertical size of one TOPO molecule. So we assume that the imaged QD surface is covered with closely packed TOPO molecules. The estimated lateral size of TOPO molecule is 5.5Å[2]. Then the localization size of 1.4 nm corresponds to 2 or 3 TOPO molecules. So we claim that the mechanism involved with this phenomenon only affects 2 or 3 capping molecules nearby.

2. Another noticeable feature is that the specific sites with the strong differential conductance are not recognizable in topography image. Any detectable change of tip height is observed on whole QD surface, even though their STS result show more than 20 fold enhanced signal. This inconsistency is explained by polarity of imaging bias. Since imaging with positive bias occasionally induced sudden change of QD moving or tip condition change, we usually used negative imaging bias. All the images in this chapter are obtained at negative bias and set point for STS is also set as negative. As can be seen in (Fig. 5.4), STS signals at negative sample bias are not quite different for all over the line. So it is apparent to see any difference in topography taken at

[1]The temperature is about 70°C and it is lower than thermal decomposition temperature of ligand materials

[2]The distance between closely packed TOPO is estimated from STM image on Au(111) surface. Since QD solution should be in rich-ligand condition to prevent aggregation, the excessive ligand molecules are also deposited by pulse injection. When we overdose the solution, we usually observed dispersed capping ligand on Au(111). We present the details about the imaged capping molecules on chapter 6.

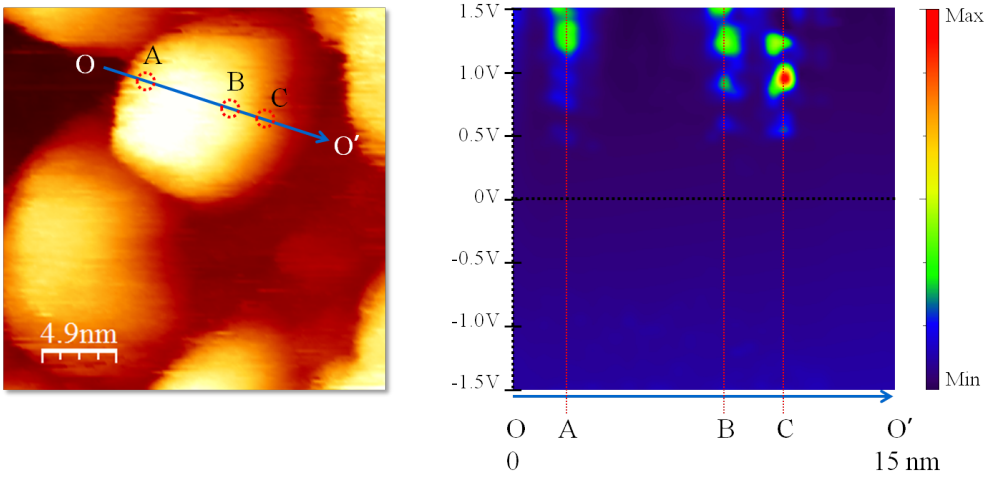

Figures 5.4 **SR-STS across a single QD** - Differential Conductance obtained from a center line of a single QD. The STM tip is moved from point O to O′, about 15 nm. And the 32 obtained spectra in 15 nm correspond to 4.7Å point distance. The obtained spectra reveal the spatial localization of the strong gap states. The localized sites are depicted by red circles and lines with labels, A, B and C. As shown in the map, the peak intensities are strong at those sites than other parts of the QD.

negative bias. It is contrast to the strong peak intensity difference at positive bias.

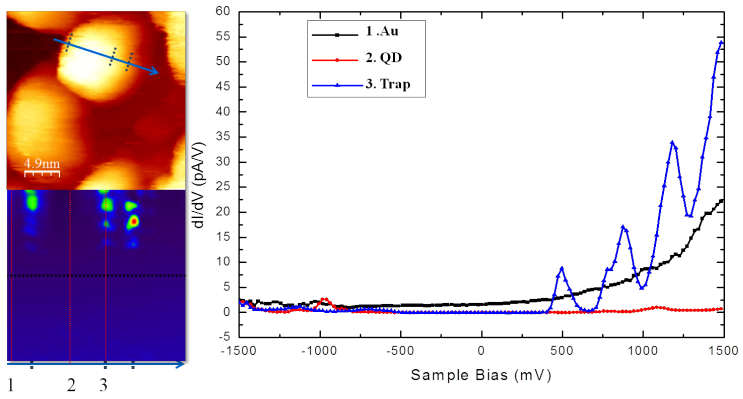

Figures 5.5 **Comparison of spectra from the trap states and interstitial part of the QD** - Three graphs are from bare gold surface (1), the trap sites (2) and interstitial part of QD (3). As shown in the graphs, the trap state has strong conductance even stronger than that of bare metallic gold surface. On the other hand, other QD surfaces have suppressed conductance like the red graph. (To see the details of the red curve, the magnified version is shown in (Fig. 5.6)

With the different behavior at positive and negative bias, we can exclude the possibility of being that the phenomenon is related to the absent of capping molecules. Because the absent of capping molecules is likely to induce indentation in topography regardless of imaging bias, the smooth surface image at negative bias cannot be explained by the deficient capping layer. So we expect that this phenomenon is related to a surface condition underneath the capping ligand, on the surface of the QD. And the condition also affects the tunneling conductance only at negative bias.

3. We note that the regions other than the three sites show typical STS with the gap structure. Since the enhanced peak size prevents the recognition of spectra in the same scale, we magnified the STS result of the interstitial site in (Fig. 5.6). In the magnified view, it is clear that the QD surface other than the specific sites have the

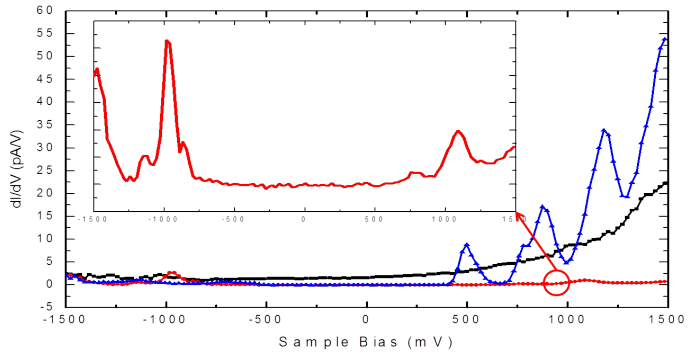

Figures 5.6 **Magnified View of the Red Curve in (Fig. 5.5)** - The curve is magnified by 10 times. The structure with the ordinary gap size is visible. Spectra obtained on the surface of QD other than three trap sites show similar structure with this graph.

electronic structure with the ordinary gap feature. This observation also assures that the special condition does not alter the other parts of the QD surface and only affects the property of localized sites.

4. We cannot see any nominal difference in image and spectroscopy at negative bias. At positive bias, however, the enhancement of differential conductance of the specific sites exceeds 20 fold than other sites. If we assume that this phenomenon is related to any static change of electronic state [3], then the model will include the modification of electronic structure or spatial dispersion of wavefunction at the positive energy. Between the two possibilities, the modified electronic structure cannot solely explain such a large enhancement. Any localized condition with 20 times larger local electron density than nearby sites is unlikely.

So we expect that the large enhancement is explained by delocalization of the

[3]though we cannot completely exclude the possibility of dynamic change like charging of the specific sites.

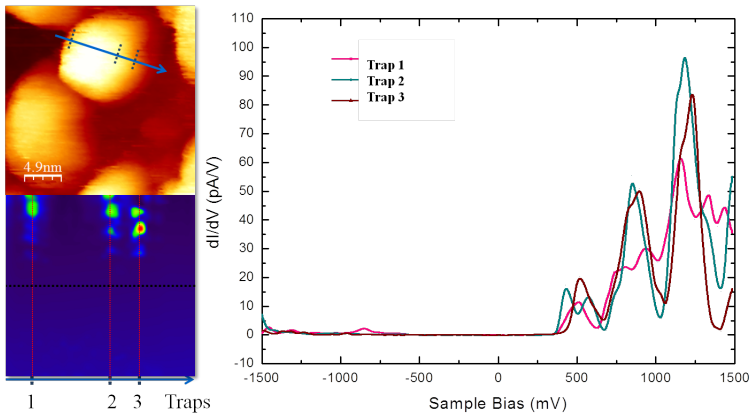

Figures 5.7 **Site variations of the trap states** - The three trap states show similar spectra. However, their detailed structures are different from each other. This variation indicates that their origins such as defects also have diversities.

wavefunction. The delocalization can enhance the conductance between two electrodes (STM tip and metal substrate) only when the dispersed wavefunction secures conducting pathway between the two electrodes. Since we already observed the localized characteristics in lateral direction, the formation of conducting path toward the metal substrate is inconsistent with this situation. The other pathway to the other electrode, i.e. delocalized wavefunction toward the STM tip, will be a major possibility.

5. The last notable feature about the spectra is variation of spectrum from site to site. The graph in (Fig. 5.7) emphasizes the difference of spectra of the three sites. This variation indicates the existence of various types of origins for this phenomenon.

Throughout these features, the states are consistent with the external trap states responsible for blinking.

5.2 Possible Mechanism

As we pointed out in the previous section 5.1, the observed strong gap states show certain properties. The previously described properties can be summarized as follows.

- Localization
- Affects only empty states
- Strongly enhanced conductance
- No vacancy in ligand molecules covering the QD surface
- No difference in filled states
- Site variation

From these properties, we propose the most probable model. From the fact that there is no evidence of vacant ligand molecule, the origin of the states should be localized underneath the surface ligands and it will be covered by the ligands. And the temperatures during the whole process were much lower than the thermal dissociation temperature of ligand molecule. This also disproves the possibility of flawed ligand molecule. The most probable defect is crystal defect on QD surface which is formed during the synthesis[59]. So we examine the possible defect types to reveal the origin of strong gap states.

Though there are many possible defect types, they can be reasonably classified by two category, Zn or S deficient defects. So we compared their possibilities by calculation. For lack of computing power, the calculation of whole QD and ligand system was impossible. Instead of that, we made small test system to investigate the possibility.

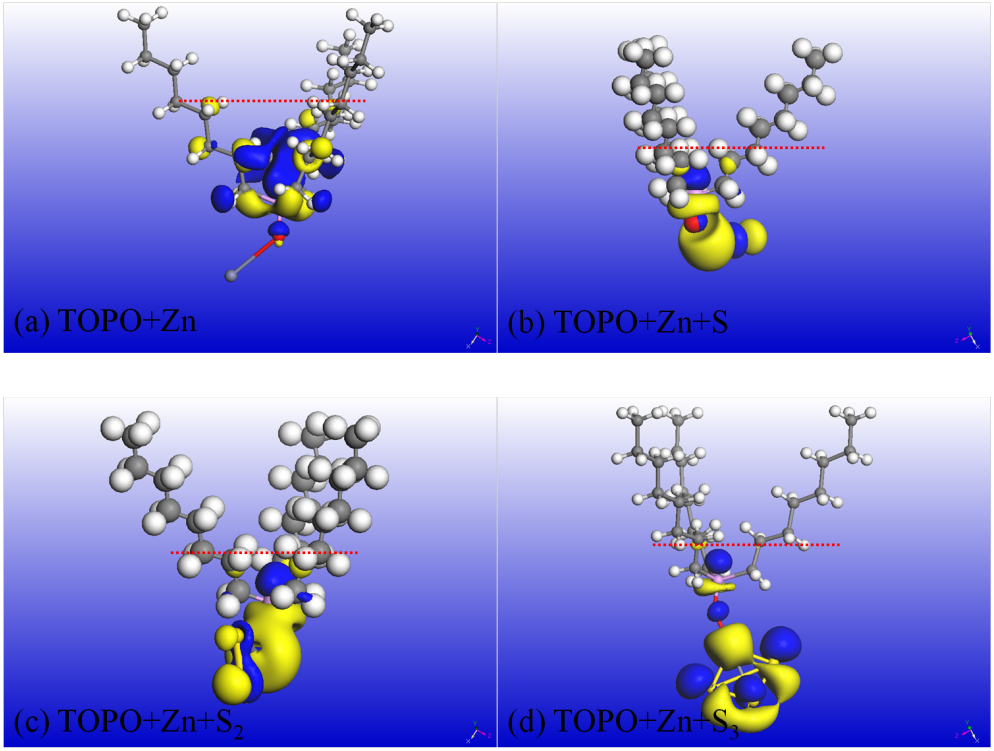

Figures 5.8 **The LUMO states of various molecular models** - (a) TOPO with a Zn atom (b) TOPO with a Zn and a S atom(c) TOPO with a Zn and two S atom(d) TOPO with a Zn and three S atom; From (a) to (d) as we add more sulfur atoms, the LUMO states show localization to the end of TOPO molecule. With these results, we can see the possibility of LUMO delocalization with deficient sulfur atoms. The TOPO attached to a sulfur-defective Zn atom will show delocalized wavefunction outwards to STM tip.

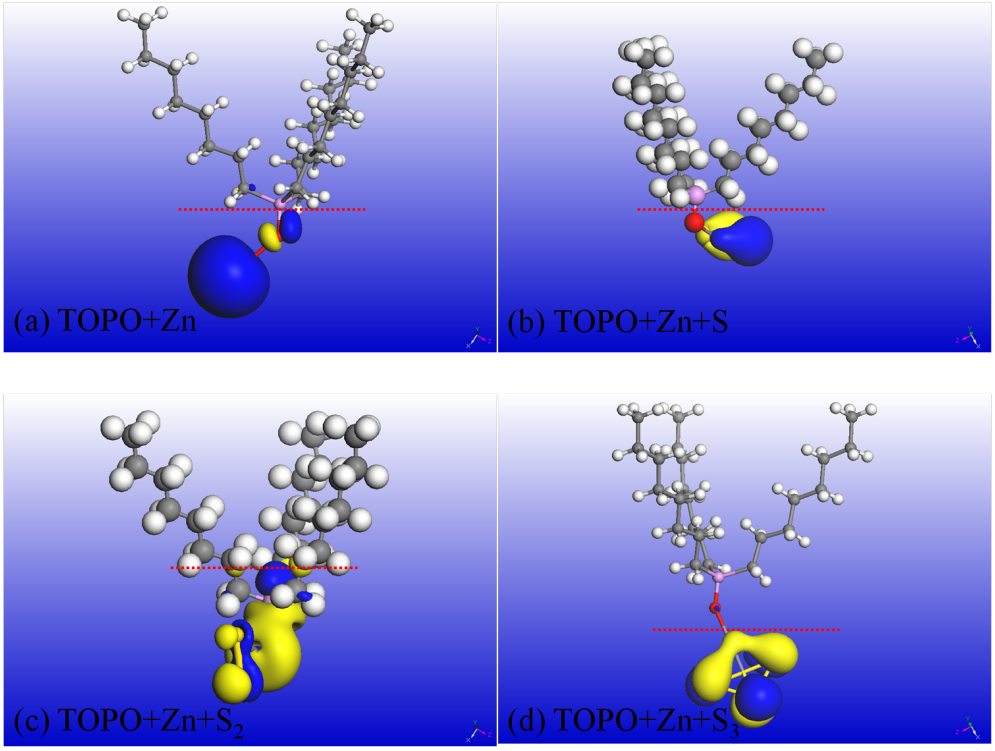

Figures 5.9 **The HOMO states of various molecular models** - (a) TOPO with a Zn atom (b) TOPO with a Zn and a S atom(c) TOPO with a Zn and two S atom(d) TOPO with a Zn and three S atom; All the states are localized under the second carbon atoms. These show the possible reason for no difference in negative bias over defect states.

We calculated single ligand molecules with small fragment with density functional theory calculation. Among many possible fragments, we tried to find a combination which has delocalized feature in LUMO orbital. So we found a tendency of orbital delocalization to outward direction with sulfur deficient fragments. A simple examples of such fragments are shown in (Fig. 5.8). As shown in the result, LUMO is significantly delocalized to the direction of triangular carbon chain when sulfur is deficient. The model with no sulfur atom, (Fig. 5.8 (a)), show LUMO extended to the fourth carbon atom, while the other cases show distribution limited below the second carbon atom. So this delocalization tendency will explain the enhancement of tunneling conductance by shortening the gap between LUMO and tip wavefunction.

And we also exhibit calculation results about HOMO distribution on the same models. To be consistent with the experimental results, they should show no significant variation. As shown in (Fig. 5.9), they show no significant delocalization in all atomic models. For all the cases, the HOMOs do not extend to carbon chains. So these results prove the observation of no tunneling conductance enhancement in negative sample bias.

Though these are not the direct calculation over the realistic system, they show the possibility of empty state delocalization towards the outside of QD. So sulfur deficient defects are most probable explanation of the observed defects.

5.3 Perspectives

As long as we know, this study is the first observation of defects at the sub-QD level. So more experiments and theoretical modeling are still required to fully reveal the all defect types. The importance of defect characterization is not only limited to discovery itself, but also connected to many phenomena which are related to defect

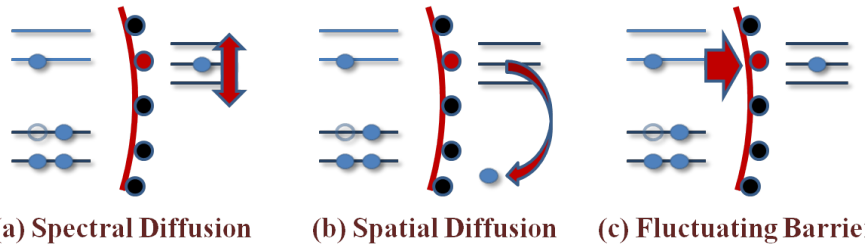

Figures 5.10 **Various Suggested mechanisms related to external trap states** - (a) spectral diffusion : the observed large broadening of the trap state can be explained by spectral diffusion (b) spatial diffusion : seems to be inconsistent with our observation for there is no signature of diffusing electron state around QD surface (c) fluctuating barrier : this model cannot be proved only by tunneling current measurement. simultaneous optical detection would relate the tunneling current fluctuation with blinking states.

dynamics. And solving the relation between the defects and the blinking problem will be the first priority.

From the observation result, we can add more feasibility to existent blinking models. For example, spectral diffusion model is consistent with the observed large broadening of the external trap states. So if the large broadening causes prolonged lifetime of the blinking dark states, then simultaneous optical measurement will probe the dark states according to the spectral broadening. Though the spatial diffusion model seems to be inconsistent with our observation[4], more precise modeling of blinking is only possible by optical measurement.

In this regard, the detection of photons from the tunneling junction is essential in solving the problem. So we plan to add photon detection capability to our system for simultaneous optical measurement with tunneling current measurement. We present our CAD design in appendix.

[4]In the timescale of our measurement, i.e. typically 1 ms or longer, there was no signature of spatially diffused electron state

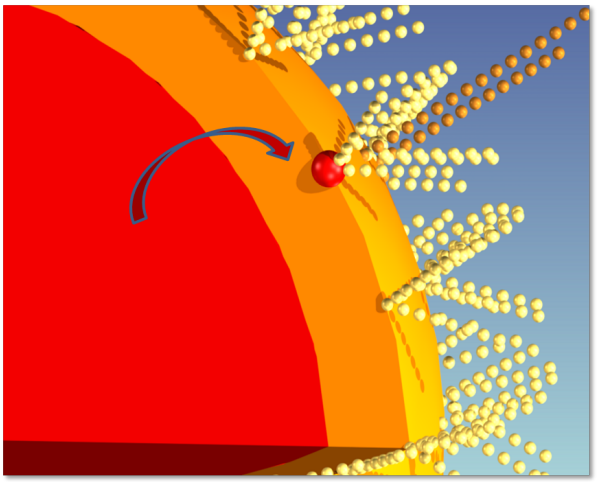

Figures 5.11 **Schematic image of external trap** - The observed gap states on QD is the most probable candidate of external trap states responsible for blinking. However, more direct proof is only possible by simultaneous photon detection from the tunneling junction. When electroluminescence photons from tunneling junction are detected, then the relation between the external trap states and blinking phenomenon can be proved. And possibly, the result will pave the way to far more efficient applications of QD

Chapter 6 Modeling of Negative Differential Resistance

6.1 Observation of NDR

At relatively low tunneling current set point (about less than 200 pA), we usually observed QD confined states fits well with DFT calculation. Though we suffered from unstable tunneling signal at higher set point, in some special cases, it is possible to obtain stable tunneling current signals and spectrum without QD moving or abrupt tip condition changes. The obtained spectra at higher tunneling current set point show extraordinary feature of negative differential resistance as shown in (Fig. 6.1). Around 300 pA set point, the differential conductance becomes negative which means the decreasing current with increasing bias at that bias range.

We also confirmed the existence of NDR effect in tunneling current measurement which is recorded simultaneously with the differential conductance spectra. The observed tunneling current also show the reduction of current with increasing bias at the energy of NDR in STS. So we can exclude the possible misleading in lock-in techniques like overload or use of insufficient sensitivity.

According to the transfer Hamiltonian approach, the tunneling current through the junction can be modeled by the convolution of the tip and sample density of states. Then the tunneling current is proportional to the integral of this form,

$$I \propto \int_0^V \rho_{tip}(\varepsilon) T(\varepsilon) \rho_{sam}(\varepsilon) d\varepsilon \tag{6.1}$$

So even if the integrand $\rho_{tip}(\varepsilon)T(\varepsilon)\rho_{sam}(\varepsilon)$ decreases at certain range of the energy, the effect should overcome the extension of integral range to manifest the NDR

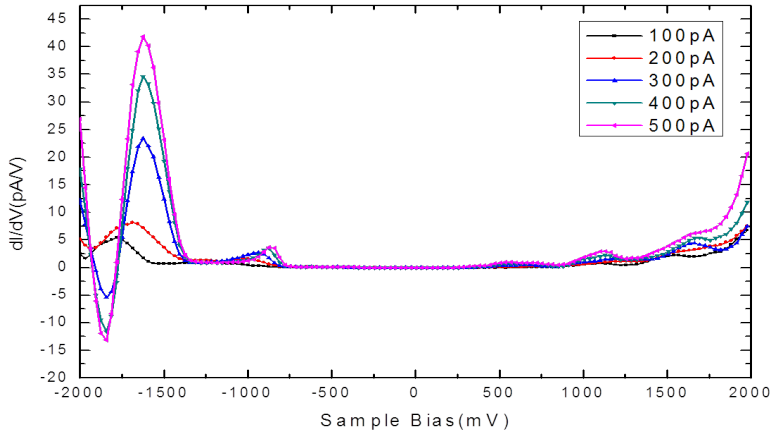

Figures 6.1 **STS on QD with NDR observed** - tunneling spectrum of QD on metal substrate. At low tunneling current set point, the spectrum shows typical QD confined states. As the current increases or the STM tip goes closer to QD, the spectrum shows evolution of NDR at negative bias. The NDR does not occur at positive bias.

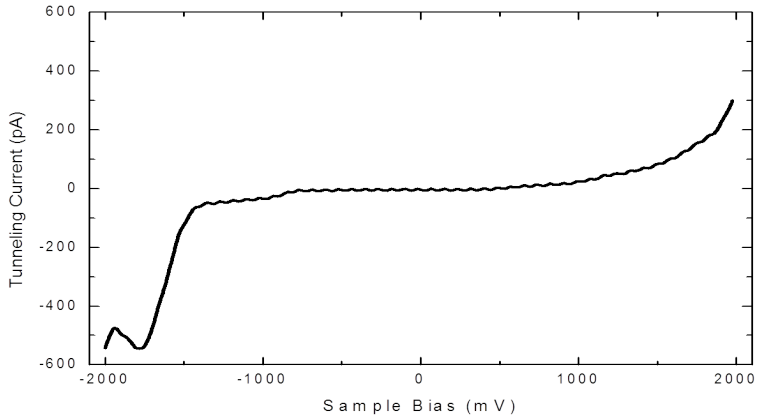

Figures 6.2 **Tunneling Current recorded with the NDR** - tunneling current measured simultaneously with the spectrum. At negative bias, the tunneling current decreases as the bias increases, so the observed NDR spectrum is consistent with this I-V curve. This excludes the possibility of misleading in using lock-in technique.

spectrum. In this context, the NDR occurs very rarely with special conditions. So by investigating the certain conditions responsible for the NDR, we can obtain much information about the system.

The notable features of the observed NDR are summarized as three points.

Firstly, the observed spectra show evolution of the tunneling conductance from positive to negative values. In other words, the NDR only occurs when the STM tip is sufficiently close to the QD surface. Then it is apparent that the mechanism responsible for this NDR effect should be induced only at close proximity of tip to QD.

Secondly, the NDR is only occurred at high negative sample bias of about 1.5 V and not observed at low negative or whole positive bias range. This behavior suggests a intuition about the origin of the NDR effect. The deep energy levels of occupied states are farthest from the vacuum level among the energy levels of QD in the measurement range. Then the states at negative bias have higher tunneling barrier (energy difference with vacuum level) than other states. So the mechanism for the NDR might be related to the elevated barrier height.

The final observation is the direction of peak shift with increasing set point current. (Fig. 6.3) is the magnified view of the NDR tunneling spectra. The peak shift to lower energy side is clearly shown in the view. The direction of the shift is the opposite of the common direction of level shifts in double barrier tunneling junction. The schematic representation of such a typical voltage divider model is shown in (Fig. 6.4). When we approach the STM tip to the QD deposited substrate, and then the barrier between tip and QD is lowered relative to the barrier between the QD and the substrate. Then more voltage is applied to the lower barrier between the QD and the substrate as indicated by solid blue arrow in the diagram. In this case, higher bias

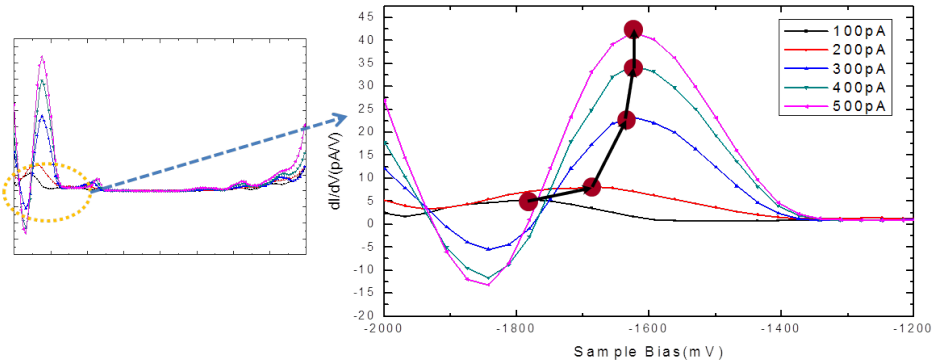

Figures 6.3 **Magnified view of the NDR spectrum** - The maximum point of each spectrum is marked by red dot. As the tunneling current increases, the maximum point shifts to the direction of lower energy. Since the set point current corresponds to the area under the dI/dV curve, the peak intensity also rises as the tunneling current increases.

is required to resonate the tunneling electrons with the QD energy level again. The increase of the bias at new resonant position is described by solid red arrow in the right panel. So according to the voltage divider model, the peaks should shift to the higher bias direction which is the opposite of the experimental observation. So the mechanism of NDR should also reveal this peculiar peak shift.

6.2 NDR Mechanisms

6.2.1 Symmetry Matched Resonant Tunneling

The most famous application of NDR is the tunnel diode which is also known as Esaki diode[20, 21]. Since its first observation of negative resistance in highly doped p-n junction in 1957, many NDR effects share the common principle with the tunnel diode. The main idea to describe the NDR in these cases can be found in the original energy diagram of Esaki**??** in (Fig. 6.5). The electrons can tunnel through the junction

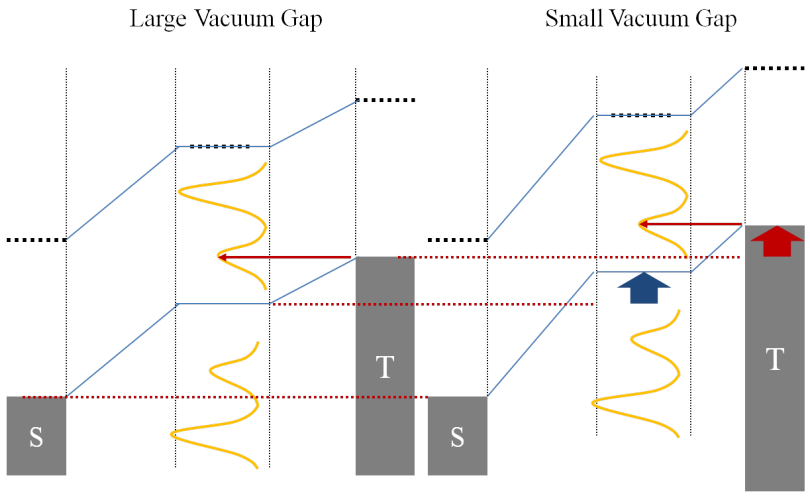

Figures 6.4 **Comparison of resonant tunneling with large and small vacuum gap size** - The left diagram shows resonant tunneling with large vacuum gap(lower set point current). When we push the STM tip to the QD (higher set point current), then more voltage is divided to the left barrier (blue solid arrow) since the resistance of vacuum gap is lowered. Then the resonant condition can only be satisfied by elevate the whole voltage (red solid arrow). So the resonant peak appears at higher bias in STS, if we increase the tunneling current.

only when the two electrodes have occupied and unoccupied states at that energy. Then the applied bias acts as a window of tunneling and at appropriate bias there can be resonant tunneling between two electrodes. If the resonant tunneling is occurred between two electrodes with energetically localized states (like the states of heavily doped semiconductors), then the current flows only at the resonant and cannot pass through when the alignment is mismatched by higher applied bias. This reduction in current shows negative resistance of the junction which is impossible with classical current flow.

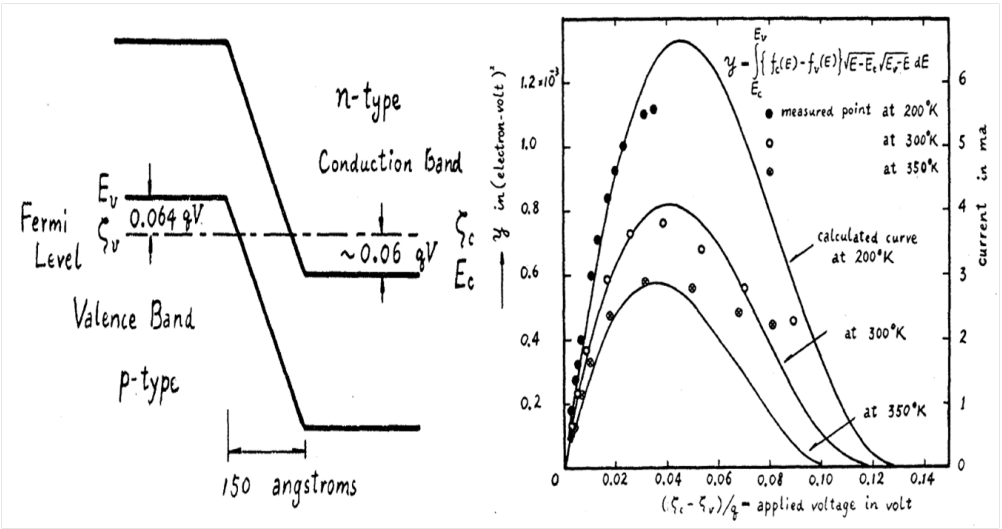

Figures 6.5 **Energy Diagram and Resonant Tunneling in Tunnel Diode** - (left)The energy diagram shows an alignment of degenerate bands in p and n doped region. At this alignment, electrons can pass through the junction by quantum tunneling and at higher voltage, the alignment is broken so that no electron can pass through. (right) Measured and calculated current through the junction. Note that the current only exists when the electron tunneling is at the resonant. At higher bias, the current decreases as the voltage increases and NDR occurs.[37]

Many recent studies focus on finding the underlying mechanism of the NDR in many tunneling systems. A new aspect of the NDR is found by a tunneling spectrum

between a nickel tip and a molecule[14]. The observed NDR reveals that the tunneling current can flow only when the spatial symmetry of each electrode is matched and the NDR can exist as a resonant between the two symmetry matched states. The finding refined our understanding about the NDR and the idea also proves its validity in recent observation of NDR in fullerene molecules under the STM junction [26].

In this context, the resonant tunneling model becomes the first to be compared with our observation. A geometrical similarity between the fullerene and QD under the STM junction also encouraged the comparison. The analysis, however, comes to the discrepancy with our situation. The counter evidences can be summarized as follows.

First, if the NDR is a result of resonant between two symmetry matched states, then the NDR always occurs at the bias[26]. This aspect is confirmed in (Fig. 6.6). At the point of negative conductance, the sign of the conductance does not change and rather only the magnitude of the conductance changes. When the two states have spatially matched symmetry, then their characteristics of localized narrow energy states determine the NDR property. Then at the point of the NDR, the change of tip-sample distance does not significantly alter the localization of energy. So the negative conductance cannot change to positive one.

In our experiment, however, the negative conductance occurs at the point where the conductance was positive at low set point current. The resonant tunneling mechanism does not provide any means to freely change the polarity as a function of tip-sample distance.

Second, we used tungten tip or gold coated tungten tip. The tungsten tip is known to have no significant electronic structure near its Fermi level. The absence of energetically localized state does not consistent with the resonant mechanism. And

there is also an report that between Ni and W tips, only the Ni tip shows NDR effect on a molecule tunneling spectrum[14]. And since gold is s-wave metal, gold tip does not show any significant spatial symmetry. Though the confined states of QD have some symmetry like P or D states, The tip wave function should have such symmetries to resonate the tunneling current. So both of the tips do not properly explain the resonant tunneling NDR.

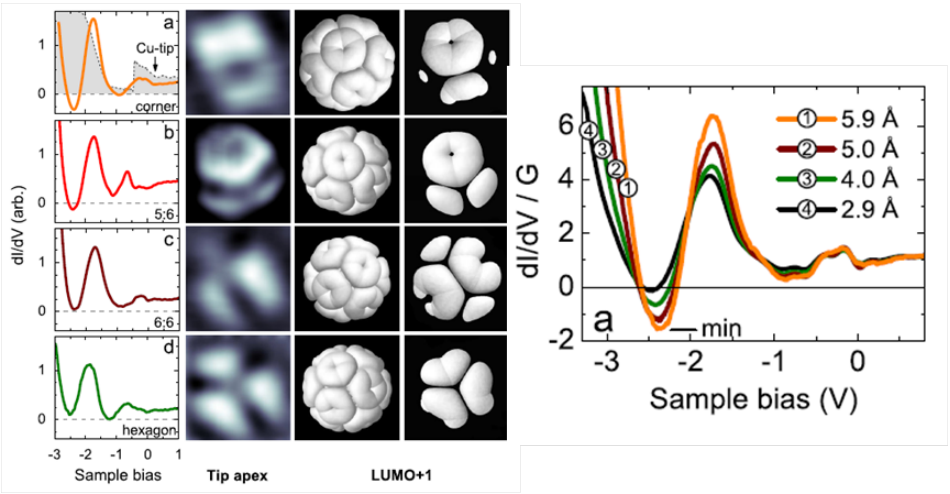

Figures 6.6 **NDR found in fullerene under STM junction** - Tunneling current can flow only when the wavefunction symmetries of the fullerene and the opposite electrode are matched. Then the resonant tunneling current can decrease when the two matched states are misaligned at higher bias. However, in this case the differential conductance cannot change the sign according to tip proximity. Only the conductance can be tuned from zero to negative at the NDR point which is not consistent with our observation.

And finally, it is impossible to explain the shift of the maximum points to lower energy direction in (Fig. 6.3) with the resonant tunneling NDR model, because the NDR of resonant tunneling occurs at specific energy levels and doest not affect the position of the peaks as in (Fig. 6.6). So our observation that the change of tunneling current induces the shift of the peak levels is out of the reach in resonant tunneling

NDR model.

With the three counter evidences, we exclude the possibility of the resonant tunneling in our experiment.

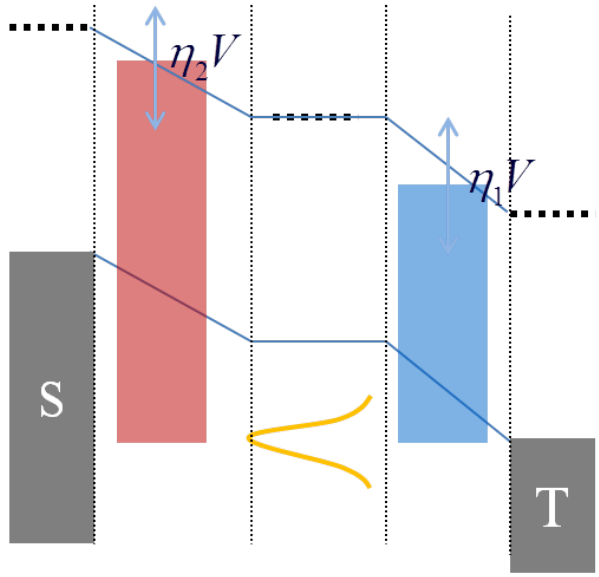

Figures 6.7 **Tunneling Resonance of Double Barrier Tunneling Junction** - When the energy localized state (yellow peak in the center) dominates the tunneling current, then the most of the tunneling electrons exist at that energy. Then the barrier experienced by the electrons approximate the total barrier height of each junction. The schematic shows the relative barrier height as red and blue squre.

6.2.2 Double Barrier Tunneling Junction Effect

Another possible mechanism found in literature is NDR effect in double barrier tunneling junction[58]. This model focuses on change of barrier height when the tunneling current is dominated by energetically localized state[43]. The energy diagram of such a Double Barrier Tunneling Junction (DBTJ) is shown in (Fig. 6.7). In this mechanism, the energetically localized state exists only in the center region. The sources of the localized state in previous reports are molecular orbitals. In our case,

the localized state can be the QD confined state. Then the resonant tunneling occurs when the chemical potential of the tip is matched with the localized energy state. Since the most of the tunneling current pass through the localized state, the state acts as a window of the tunneling current. In this aspect, we can define the effective tunneling barrier height of each junction as barrier experienced by the localized energy state. The schematic barrier height is represented as red and blue solid square in the figure.

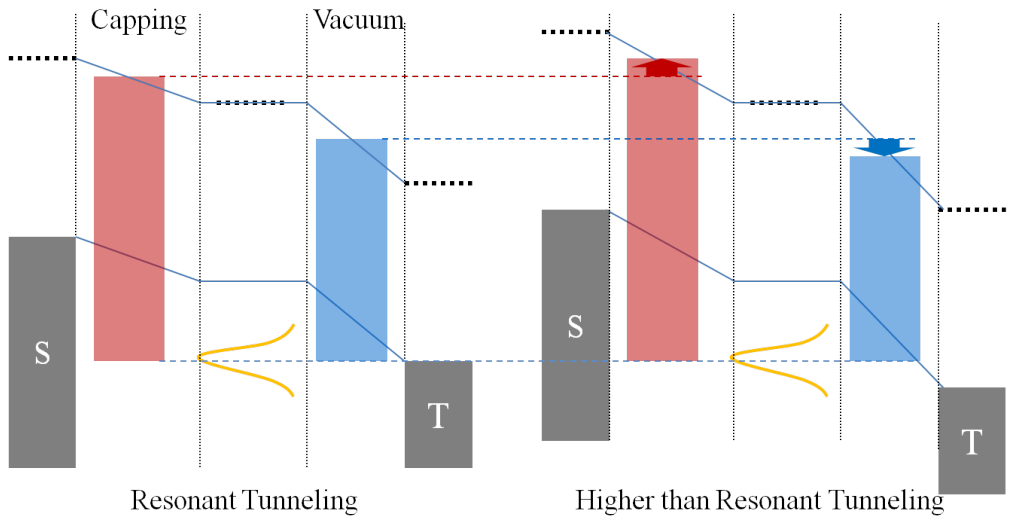

Figures 6.8 **NDR Mechanism with DBTJ** - When we increase the bias from the resonant, then the heights of each barrier changes. The raised bias increases the difference of chemical potentials of two electrodes, then the chemical potential of the left electrode increases relative to the center localized state. The chemical potential of the right electrode moves in the opposite direction. So as depicted in the right panel, the barrier of left junction (red arrow) increases while the barrier of the right junction (blue arrow) decreases.

When we increase the applied bias, then the chemical potential difference between two electrodes increases. When we compare the change of the chemical potential relative to the center localized state, then the left electrode's chemical potential increases

while that of right electrode decreases. This difference induces the opposite change of barrier height of each junction. In other words, the increase in applied bias results in the raising of the left barrier and lowering of the right barrier. These conflicting behavior of two barrier height compete each other. Then the NDR can occur only when the left barrier dominates the system. We found that the close proximity of the STM tip would lower the right junction barrier height. Then the left barrier can dominate the tunneling current and NDR can occur.

6.3 DBTJ Modeling

To verify the DBTJ NDR mechanism and further explain the experimental observations, we performed a numerical simulation of DBTJ with WKB approximation. The potential distribution of the QD under the STM tip is calculated by classical electrostatics. Then the result is used to numerical calculation of tunneling conductance under the assumption that the tunneling is dominated by the energy localized state of the QD.

6.3.1 Potential Distribution

WKB approximation explains the behavior of tunneling junction as the multiplication of a factor to the wavefunction. The factor also acts as coupling strength of wavefunction across the junction. The factor, as described in chapter 2, can be written as follows.

$$D = exp[-\int_{x_1}^{x_2} \sqrt{V(x) - \epsilon} dx] \tag{6.2}$$

where the integral goes over the barrier region and $V(x)$ renders the potential distribution inside the barrier.

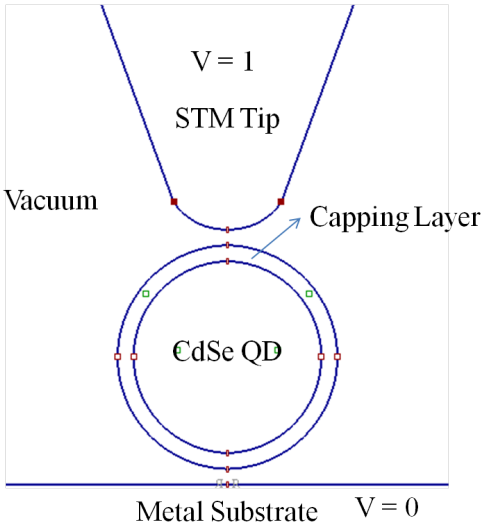

Figures 6.9 **Geometry of DBTJ used in Finite Element Method Calculation** - The STM tip is rendered as 2 nm radius tip end with 25 ° half cone angle and the QD is 6 nm sphere with dielectric constant 8. The upper barrier consists of vacuum gap and capping layer while the lower barrier consists of capping layer. We varied the size of vacuum gap and capping layer from 0.1 nm to 1.1 nm which generates 121 sets of geometries

To obtain the realistic predictions of the two tunneling junction, we estimated the potential distribution of the DBTJ by solving the classical Poisson equation through Finite Element Method (FEM). To use FEM, the geometry of the DBTJ is defined as in (Fig. 6.9) and we varied thickness of each barrier to find the best solution to our geometry. By the variation of the barrier thicknesses, we obtained 121 sets of geometries (11 thickness variation in both of vacuum and capping layer. from 0.1 nm to 1.1 nm). Then the each geometry is covered with triangular mesh with the characteristic length scale smaller than 0.15 nm as in (Fig. 6.10). The example of obtained potential distribution is drawn in the right panel and the potential distribution along the center line is extracted from each calculation as (Fig. **??**).

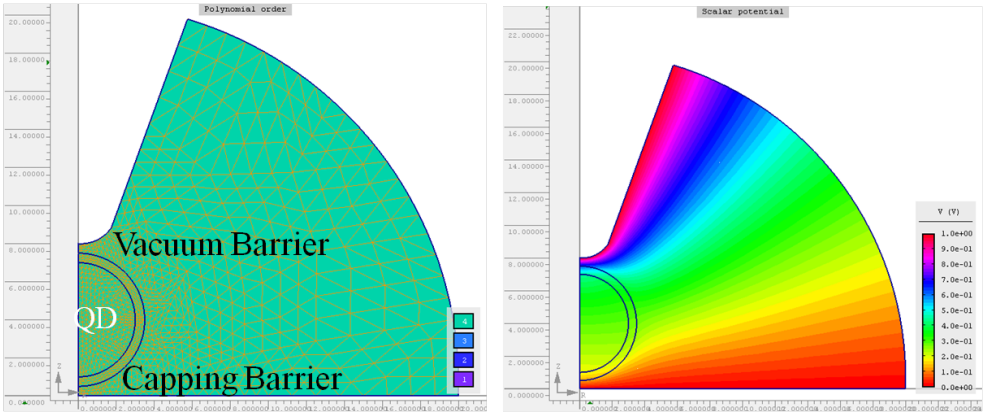

Figures 6.10 **Potential Distribution obtained by Finite Element Method** - (left) mesh grid overcoat the geometry to supply the calculation points for FEM method. The characteristic length scale of the mesh is smaller than 0.15 nm. (right) Calculated potential distribution is represented by color mapping. We note that the two junctions draw major potential drop as indicated by the abrupt color change.

The details of the calculation and used script are shown in (appendix. A). The calculated results are exported to be used in the conductance calculation in the next section.

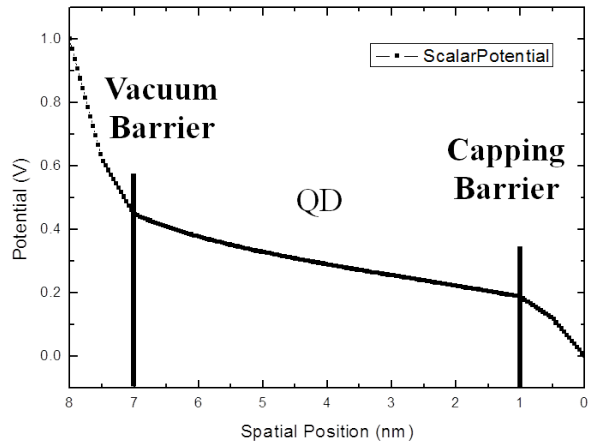

Figures 6.11 **Potential Distribution obtained by the FEM Calculation** - An example of obtained potential distribution across the center line of the geometry. The potential steeply drops in the two barrier regions. Though the potential drop across the QD is also visible, the influence of this electric field to the QD confined states was not included in the calculation, because the spatial dispersion due to the electric field does not change the conductance significantly. The effect only gives spatial rearrangement of the confined states in the QD.

6.3.2 Calculation of Tunneling Conductance

As described in the chapter 2, the total coupling strength of two junctions influence the current as follows

$$I = \int_0^V \frac{D_1 D_2}{D_1 + D_2} \rho_{QD}(\epsilon) d\epsilon \tag{6.3}$$

where D_1 and D_2 are coupling strength of each junction and ρ_{QD} is the local density of state of QD. Since the energetically localized nature is the essential part of this model, we approximated the QD confined state as Gaussian type localized density of state centered at the peak position of P_h energy state. And the broadening factor is chosen to best fit to the experimental spectrum. In this calculation, the density of state of metal tip and substrate is factor out for simplification. Since the tunneling conductance spectrum does not show any significant peaks in the range of interest, this assumption does not change the main property of the junction. With the simplified model of (Eq. 6.3), the competing behavior of D_1 and D_2 can be calculated.

The calculation of the numerical integration is done on 121 sets of geometry. Then the result is numerically differentiated to obtain the tunneling conductance. The chosen sets of result are shown in (Fig. 6.12). The obtained properties of the result can be summarized as follows.

1. No NDR is observed at thin capping layer for all variations of vacuum gap thickness.

2. At capping layer of about 0.6 nm, the NDR appears. By approaching the STM tip to QD (decreasing the vacuum gap thickness), we also find that the intensity of NDR increases. This result is well agreed with our experimental observations.

3. The best fit to our experiment is obtained at 1.0 nm capping layer thickness. And at this condition, the peak shift towards the low energy is also reproduced.

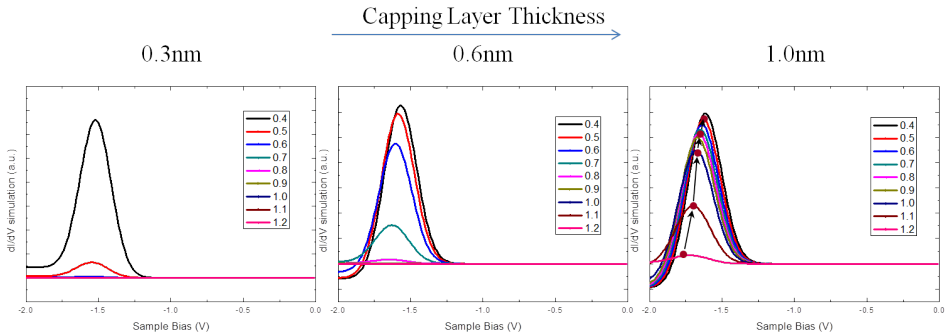

Figures 6.12 **Calculated Result of DBTJ conductance** - Among the 11 sets of the result, three representatives are presented. (left: capping layer thickness of 0.3 nm) at thin capping layer thickness, the result shows no negative conductance. The legend in the graph shows the vacuum gap between the STM tip and QD. (middle: capping layer thickness of 0.6 nm) at moderate capping layer thickness, the NDR occurs at the bias slightly larger than the resonance. (right: capping layer thickness of 1 nm) The ratios between positive and negative part of the conductance is best fit to experimental spectrum. And even the observed peak shift to lower energy is also reproduced.

By the numerical simulation, we obtained geometrical factors best fit to our experiment. The estimated capping layer is 1.0 nm. The two used capping molecules have vertical size of 0.99 nm (TOPO) and 2.02 nm(HDA), respectively. Though the images of QD did not show individual capping molecules, it is hard to imagine the thermal decomposition in our experimental procedures. So the estimated capping layer thickness confirms the existence of capping molecules on QD surface.

Chapter 7 Imaging and Characterization of Capping Molecules

7.1 Importance of Capping Layer

The capping molecules of QD act as solvent at the synthetic stage, but also as passivation after the synthesis[52]. Besides the roles, ligand molecules also decide the chemical property of QD[50]. We briefly examine the role or importance of ligand molecules in this section. Some notable features of capping molecules are summarized as follows.

- Capping layer prevents aggregation.
- decide chemical property of QD
- Decouple electronic structure of QD from outside

Unlike bulk size materials, small size materials undergo van der Waals (VDW) interaction between the particles. So materials whose size is smaller than micro meter scale usually form aggregation. The VDW interaction usually shows potentials of the Lennard-Jones potential as follows

$$V \propto (\frac{r_m}{r})^{12} - 2(\frac{r_m}{r})^6 \tag{7.1}$$

where r is the distance between two particles and r_m means the minimum energy point.

Since QD also interacts with other QDs through this VDW interaction, they usually aggregate to micro scale size without capping layer. With the help of capping

layer, the minimum energy point in the Lennard-Jones potential smears out. At the minimum energy point, the repulsive force between capping molecules exhibit repulsive force, so QDs do not attract each other. This enables prolonged lifetime of nano-sized QDs in solution and prevents degradation of QDs during deposition.

Because exposed surface of QD is covered with capping layer, they usually determine the chemical property of QD. For example, QDs with organic capping ligands dissolves in non-polar solvents while QDs with polar ligands dissolves in polar solvents. This change of chemical property comes into play when biological system is involved. Since water solubility is the essential factor in applications of biology, exchange of ligand or efficiency in the exchange are the major issues. So direct observation of capping ligands on QD surface provides valuable information to us.

Imaging of individual capping molecules on QD is required to determine packing density of the molecules. And the packing density plays important role in prediction of chemical behavior related to the QD surface[45, 33] and even optical properties[8]. But QD topography images show seamless and smooth surfaces which make suspicion of the existence of capping molecules on QD surface.

In this regard, imaging of capping molecules on QD surface is major issue of QD study[34]. However, the use of gold coated tungsten tip [1] Usually show no atomic resolution on QD surface. So no individual capping molecules are resolved on QD surface.

[1] As pointed out earlier, we usually indent clean Au(111) surface with tungsten tip to remove excessive pollutants and modify the tip end shape. This process usually resulted in the formation of gold layer on tungsten tip which compromise the image resolution with clean imaging.

7.2 Capping Molecules on Au(111)

7.2.1 Images of Capping Molecules

Instead of images on QD surface, individual capping molecules are imaged on Au(111). (Fig. 7.1 and 7.2) are typical images of HDA and TOPO molecules, respectively. The bonding site is clearly visible in HDA image as protrusion. Though the sub-molecular structure, i.e. three carbon chains, is not resolved in TOPO image, they usually make bonding through end oxygen atom.

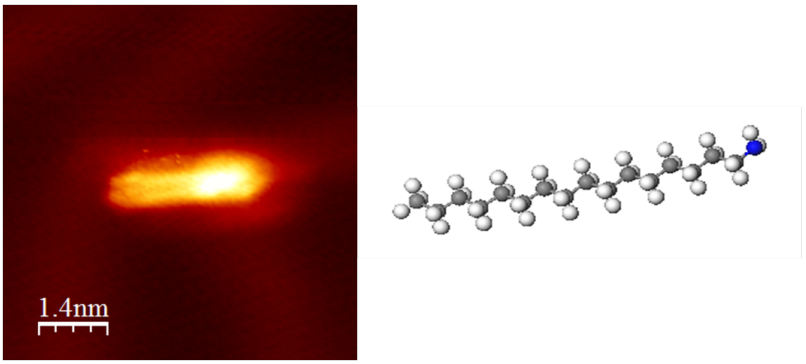

Figures 7.1 **Image of HDA at 5K** - (left) HDA molecule absorbed on Au(111) surface (right) atomic model of HDA molecule. The image shows the long carbon chain of HDA molecule and bright protrusion is observed which corresponds to nitrogen bonding with Au(111)

7.3 Determination of Bonding Direction

7.3.1 DFT Calculation

We calculate the electron distributions of LUMO and HOMO with DFT calculation. Since LUMO and HOMO are located right above and below the Fermi energy, they play major role in bonding formation.

The DFT calculation results show the distribution of HOMO and LUMO. They commonly exhibit localized wavefunction at the end atom. Both of two molecules

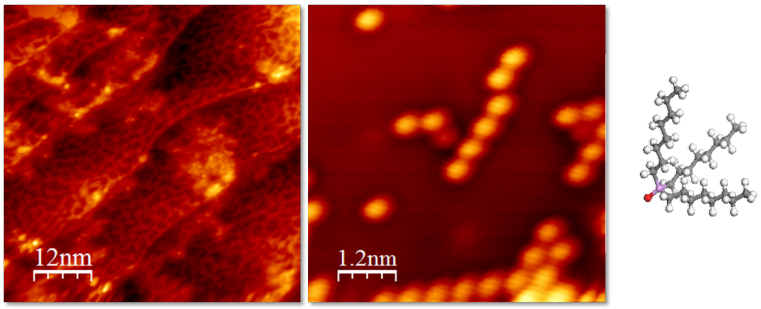

Figures 7.2 **Images of TOPO at 5K** - (left) Adsorbed TOPO molecules on Au(111). We expose clean Au(111) surface to excessive QD solution and then heated the surface up to 200°C. Since TOPO has relatively strong bonding than HDA, so HDA molecules are removed by the heating process. (middle) Image of TOPO molecular chain; The distance between each molecule is about 0.8 nm. Though three carbon chains are not resolved, TOPO typically makes bonding through end oxygen atom. (right) Atomic model of TOPO molecule; The end oxygen atom is marked with red color

have electronegative atoms at the end, oxygen and nitrogen. So the end atoms are negatively charged and will form bonding with positive ions. In our case, Zn is positively charged when it makes bonding with sulfur. So it is natural to make bonding between the negative end parts and Zn atoms.

This bonding direction is also used when they make bonding with metal electrons. As in (Fig. 7.1), the localized orbital is hybridized with metal electrons.

7.3.2 Rotational Motion

When we image HDA molecules on elevated temperature of about 80 K, we observed rotating motion of the HDA molecules. The circular object in (Fig. 7.5) is typical image of such rotating molecule. We can see the size of the circle is about 1.8 times of the original length of the molecule, so we know that the rotating motion is pinned at the end of a molecule. By comparing the observed motion with the static images at 5 K, the energy barrier of the motion can be estimated to be between 6.67

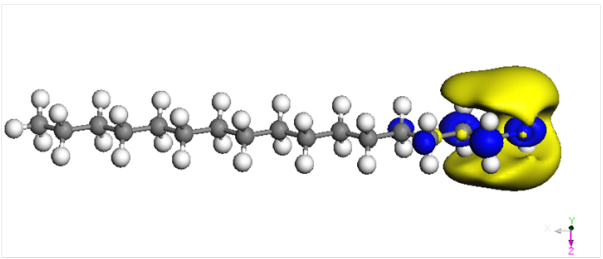

LUMO Orbital

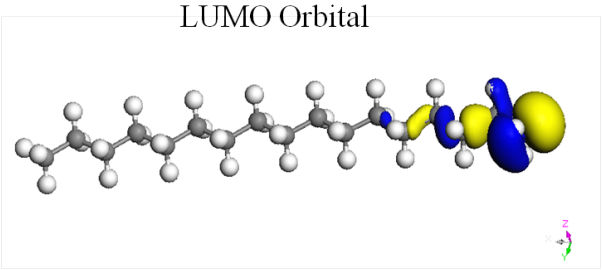

HOMO Orbital

Figures 7.3 **HOMO and LUMO Electron Distribution Calculated by DFT** - Both of HOMO and LUMO orbitals are localized at the end nitrogen atom. These orbitals form bonding with QD through hybridization. Since the high electro-negativity of end oxygen atom, HDA will be attached to Zn surface atom of QD which has partial positive charge.

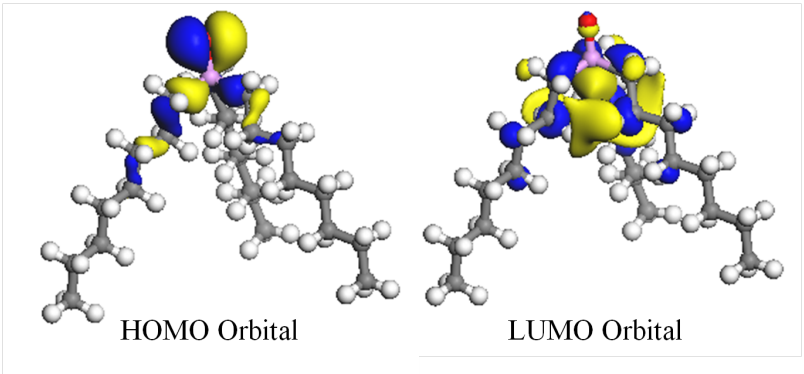

Figures 7.4 **HOMO and LUMO Electron Distribution Calculated by DFT** - TOPO also show wavefunction localized on the very end atom, Phosphor.

mV and 0.42 mV.

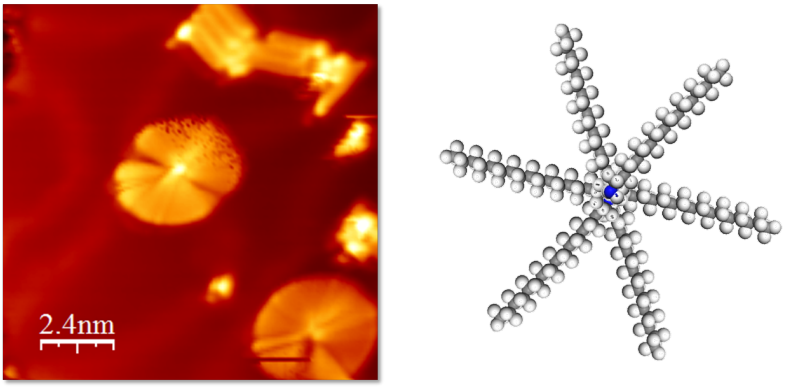

Figures 7.5 **Rotating HDA** - Image of rotating HDA molecule on Au(111) surface and its atomic model. Note that some HDA molecules aggregate and do not show any movement during the scan since the rotational motion is limited by each other.

And information about the energy barrier is obtained from bias dependent images in (Fig. 7.6). Even the small bias of 5 mV induced the rotational motion.[2]

Though the thermal energy of 5 K is not enough to rotate the molecule, switching of molecular position by tunneling current was possible. As shown in (Fig. 7.7), the molecules are intermittently switched by the tunneling current.

[2]Though the rotating images at 10 and 5 mV show relatively depressed topography, their rotational motion is apparent from the circular boundary of the depressed image. The suppressed electron density at these biases maybe the origin of the depression.

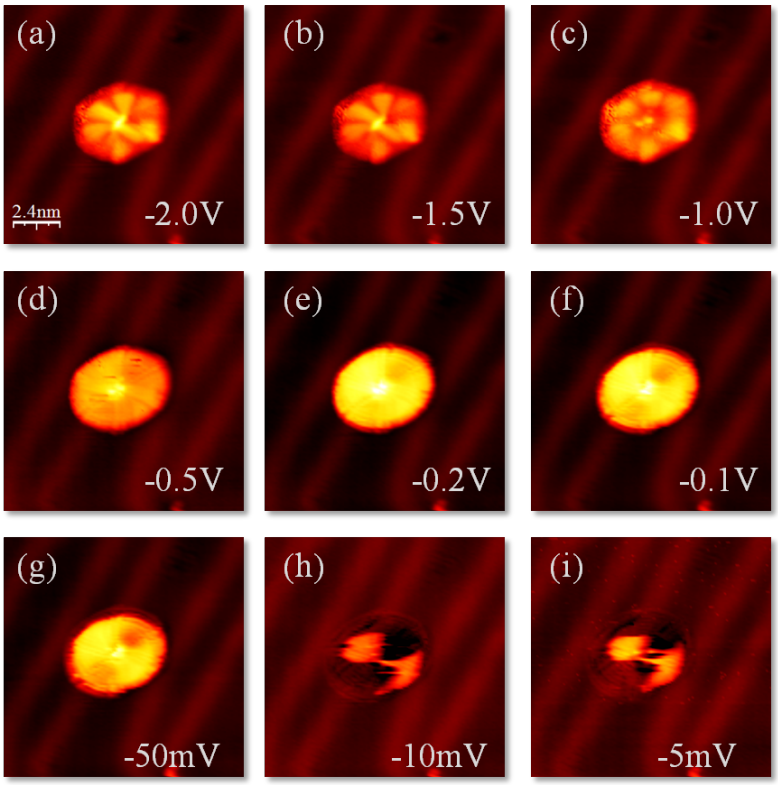

Figures 7.6 **Images of Rotation HDA at Various Sample Bias** - Each image is acquired with different sample bias from -2.0V to -5mV ((a) - (i)).

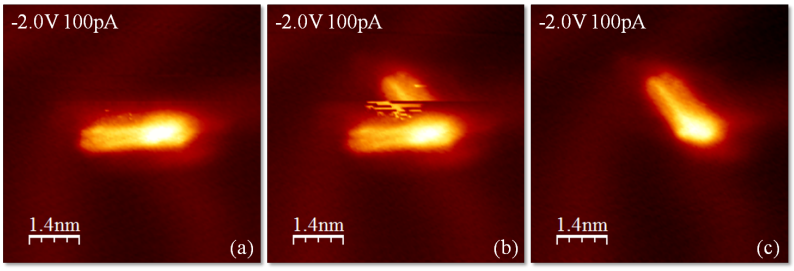

Figures 7.7 **Successive Images Showing Sudden Motion of HDA by Tunneling Current** - (left) HDA molecule image at 5K (middle) The direction of carbon chain is rotated 60° during scanning by tunneling current (right) the rotated molecule image

Bibliography

[1] A. V. Akimov, A. Mukherjee, C. L. Yu, D. E. Chang, A. S. Zibrov, P. R. Hemmer, H. Park, and M. D. Lukin. Generation of single optical plasmons in metallic nanowires coupled to quantum dots. *Nature*, **450**(7168):402–406, November 2007.

[2] Polina O. Anikeeva, Jonathan E. Halpert, Moungi G. Bawendi, and Vladimir Bulovic. Quantum dot Light-Emitting devices with electroluminescence tunable over the entire visible spectrum. *Nano Lett.*, **9**(7):2532–2536, 2009.

[3] S. Azevedo, J. R. Kaschny, C. M.C. de Castilho, and F. de Brito Mota. Electronic structure of defects in a boron nitride monolayer. *The European Physical Journal B - Condensed Matter and Complex Systems*, **67**(4):507–512, 2009.

[4] Uri Banin, YunWei Cao, David Katz, and Oded Millo. Identification of atomic-like electronic states in indium arsenide nanocrystal quantum dots. *Nature*, **400**(6744):542–544, August 1999.

[5] Uri Banin and Oded Millo. Tunneling and optical spectroscopy of semiconductor nanocrystals. *Annual Review of Physical Chemistry*, **54**(1):465–492, 2003.

[6] M G Bawendi, M L Steigerwald, and L E Brus. The quantum mechanics of larger semiconductor clusters ("Quantum dots"). *Annual Review of Physical Chemistry*, **41**(1):477–496, 1990.

[7] Debasis Bera, Lei Qian, Teng-Kuan Tseng, and Paul H. Holloway. Quantum dots and their multimodal applications: A review. *Materials*, **3**(4):2260–2345, March 2010.

[8] L.J. Brillson. Surface electronic and chemical structure of (1120)CdSe: comparison with CdS. *Surface Science*, **69**(1):62–84, December 1977.

[9] S. Brovelli, R. D. Schaller, S. A. Crooker, F. García-Santamaría, Y. Chen, R. Viswanatha, J. A. Hollingsworth, H. Htoon, and V. I. Klimov. Nano-engineered electron–hole exchange interaction controls exciton dynamics in core–shell semiconductor nanocrystals. *Nature Communications*, **2**:280, April 2011.

[10] L. Brus. Zero-dimensional "excitons" in semiconductor clusters. *Quantum Electronics, IEEE Journal of*, **22**(9):1909 – 1914, September 1986.

[11] M G Burt. Fundamentals of envelope function theory for electronic states and photonic modes in nanostructures. *Journal of Physics: Condensed Matter*, **11**(9):53–83, March 1999.

[12] Marco Califano. Off-State quantum yields in the presence of surface trap states in CdSe nanocrystals: The inadequacy of the charging model to explain blinking. *J. Phys. Chem. C*, **115**(37):18051–18054, 2011.

[13] Aldo Di Carlo. Microscopic theory of nanostructured semiconductor devices: beyond the envelope-function approximation. *Semiconductor Science and Technology*, **18**(1):R1–R31, January 2003.

[14] Lan Chen, Zhenpeng Hu, Aidi Zhao, Bing Wang, Yi Luo, Jinlong Yang, and J. G. Hou. Mechanism for negative differential resistance in molecular electronic devices: Local orbital symmetry matching. *Physical Review Letters*, **99**(14):146803, October 2007.

[15] Seth Coe, Wing-Keung Woo, Moungi Bawendi, and Vladimir Bulovi|[cacute]|. Electroluminescence from single monolayers of nanocrystals in molecular organic devices. *Nature*, **420**(6917):800–803, December 2002.

[16] Celso deMelloDonegá, Peter Liljeroth, and Daniel Vanmaekelbergh. Physicochemical evaluation of the HotInjection method, a synthesis route for monodisperse nanocrystals. *Small*, **1**(12):1152–1162, December 2005.

[17] Hugo Dil, Jorge Lobo-Checa, Robert Laskowski, Peter Blaha, Simon Berner, Jurg Osterwalder, and Thomas Greber. Surface trapping of atoms and molecules with dipole rings. *Science*, **319**(5871):1824–1826, March 2008.

[18] Jana Drbohlavova, Vojtech Adam, Rene Kizek, and Jaromir Hubalek. Quantum dots — characterization, preparation and usage in biological systems. *International Journal of Molecular Sciences*, **10**(2):656–673, February 2009.

[19] Al. L. Efros and M. Rosen. The electronic structure of semiconductor nanocrystals1. *Annual Review of Materials Science*, **30**(1):475–521, 2000.

[20] Leo Esaki. New phenomenon in narrow germanium p-n junctions. *Physical Review*, **109**(2):603–604, January 1958.

[21] Leo Esaki, Yasuhiko Arakawa, and Masatoshi Kitamura. Esaki diode is still a radio star, half a century on. *Nature*, **464**(7285):31–31, March 2010.

[22] Pavel Frantsuzov, Masaru Kuno, Boldizs|[aacute]|r Jank|[oacute]|, and Rudolph A. Marcus. Universal emission intermittency in quantum dots, nanorods and nanowires. *Nature Physics*, **4**(7):519–522, 2008.

[23] Huaxiang Fu, Lin-Wang Wang, and Alex Zunger. Applicability of the kp method to the electronic structure of quantum dots. *Physical Review B*, **57**(16):9971–9987, April 1998.

[24] Christophe Galland, Yagnaseni Ghosh, Andrea Steinbrück, Milan Sykora, Jennifer A. Hollingsworth, Victor I. Klimov, and Han Htoon. Two types of luminescence blinking revealed by spectroelectrochemistry of single quantum dots. *Nature*, **479**(7372):203–207, November 2011.

[25] Alex D Gottlieb and Lisa Wesoloski. Bardeen's tunnelling theory as applied to scanning tunnelling microscopy: a technical guide to the traditional interpretation. *Nanotechnology*, **17**(8):R57–R65, April 2006.

[26] B. W. Heinrich, M. V. Rastei, D.-J. Choi, T. Frederiksen, and L. Limot. Engineering negative differential conductance with the cu(111) surface state. *Physical Review Letters*, **107**(24):246801, December 2011.

[27] H.J. Hoffmann and E. Huber. Generation-recombination noise and defect levels in semiconducting CdSe crystals. *Physica B+C*, **111**(2–3):249–256, November 1981.

[28] Shan Jin, Yanxi Hu, Zhanjun Gu, Lei Liu, and Hai-Chen Wu. Application of quantum dots in biological imaging. *Journal of Nanomaterials*, **2011**:1–13, 2011.

[29] Tae-Ho Kim, Kyung-Sang Cho, Eun Kyung Lee, Sang Jin Lee, Jungseok Chae, Jung Woo Kim, Do Hwan Kim, Jang-Yeon Kwon, Gehan Amaratunga, Sang Yoon Lee, Byoung Lyong Choi, Young Kuk, Jong Min Kim, and Kinam Kim. Full-colour quantum dot displays fabricated by transfer printing. *Nature Photonics*, **5**(3):176–182, February 2011.

[30] Kathryn E. Knowles, Matthew T. Frederick, Daniel B. Tice, Adam J. Morris-Cohen, and Emily A. Weiss. Colloidal quantum dots: Think outside the (Particle-in-a-)Box. *J. Phys. Chem. Lett.*, **3**(1):18–26, 2011.

[31] Todd D. Krauss and Jeffrey J. Peterson. Bright future for fluorescence blinking in semiconductor nanocrystals. *J. Phys. Chem. Lett.*, **1**(9):1377–1382, 2010.

[32] Todd D. Krauss and Jeffrey J. Peterson. Quantum dots: A charge for blinking. *Nature Materials*, **11**(1):14–16, December 2011.

[33] Erol Kuçur, Wendelin Bücking, Ralf Giernoth, and Thomas Nann. Determination of defect states in semiconductor nanocrystals by cyclic voltammetry. *J. Phys. Chem. B*, **109**(43):20355–20360, 2005.

[34] Emma E. Lees, Menachem J. Gunzburg, Tich-Lam Nguyen, Geoffrey J. Howlett, Julie Rothacker, Edouard C. Nice, Andrew H. A. Clayton, and Paul Mulvaney. Experimental determination of quantum dot

size distributions, ligand packing densities, and bioconjugation using analytical ultracentrifugation. *Nano Lett.*, **8**(9):2883–2890, 2008.

[35] Peter Liljeroth, Pedro A. Zeijlmans van Emmichoven, Stephen G. Hickey, Horst Weller, Bruno Grandidier, Guy Allan, and Daniël Vanmaekelbergh. Density of states measured by Scanning-Tunneling spectroscopy sheds new light on the optical transitions in PbSe nanocrystals. *Physical Review Letters*, **95**(8):086801, 2005.

[36] Lucian Jdira. *Electronic properties of semiconductor quantum dots.* PhD thesis, Utrecht University, November 2008.

[37] J. M. Luttinger and W. Kohn. Motion of electrons and holes in perturbed periodic fields. *Physical Review*, **97**(4):869–883, February 1955.

[38] Theresa Lutz, Alexander Kabakchiev, Thomas Dufaux, Christian Wolpert, Zhe Wang, Marko Burghard, Klaus Kuhnke, and Klaus Kern. Scanning tunneling luminescence of individual CdSe nanowires. *Small*, **7**(16):2396–2400, June 2011.

[39] M. Azad Malik, Paul O'Brien, and Neerish Revaprasadu. A simple route to the synthesis of Core/Shell nanoparticles of chalcogenides. *Chem. Mater.*, **14**(5):2004–2010, 2002.

[40] Gennady Margolin, Vladimir Protasenko, Masaru Kuno, and Eli Barkai. Power-law blinking quantum dots: Stochastic and physical models. In William T. Coffey and Yuri P. Kalmykov, editors, *Fractals, Diffusion, and Relaxation in Disordered Complex Systems*, page 327–356. John Wiley & Sons, Inc., 2005.

[41] Oded Millo, David Katz, YunWei Cao, and Uri Banin. Imaging and spectroscopy of Artificial-Atom states in Core/Shell nanocrystal quantum dots. *Physical Review Letters*, **86**(25):5751–5754, June 2001.

[42] C. B. Murray, D. J. Norris, and M. G. Bawendi. Synthesis and characterization of nearly monodisperse CdE (E = sulfur, selenium, tellurium) semiconductor nanocrystallites. *J. Am. Chem. Soc.*, **115**(19):8706–8715, 1993.

[43] Y. M. Niquet, C. Delerue, G. Allan, and M. Lannoo. Interpretation and theory of tunneling experiments on single nanostructures. *Physical Review B*, **65**(16):165334, April 2002.

[44] Karin Overgaag, Peter Liljeroth, Bruno Grandidier, and Daniël Vanmaekelbergh. Scanning tunneling spectroscopy of individual PbSe quantum dots and molecular aggregates stabilized in an inert nanocrystal matrix. *ACS Nano*, **2**(3):600–606, 2008.

[45] Eran Rabani, Balázs Hetényi, B. J. Berne, and L. E. Brus. Electronic properties of CdSe nanocrystals in the absence and presence of a dielectric medium. *The Journal of Chemical Physics*, **110**(11):5355–5369, March 1999.

[46] Massimo Rontani and Elisa Molinari. Imaging quasiparticle wave functions in quantum dots via tunneling spectroscopy. *Physical Review B*, **71**(23):233106, June 2005.

[47] Shamir Rosen, Osip Schwartz, and Dan Oron. Transient fluorescence of the off state in blinking CdSe/CdS/ZnS semiconductor nanocrystals is not governed by auger recombination. *Physical Review Letters*, **104**(15):157404, April 2010.

[48] Gregory D. Scholes and Garry Rumbles. Excitons in nanoscale systems. *Nature Materials*, **5**(9):683–696, 2006.

[49] K. T. Shimizu, R. G. Neuhauser, C. A. Leatherdale, S. A. Empedocles, W. K. Woo, and M. G. Bawendi. Blinking statistics in single semiconductor nanocrystal quantum dots. *Physical Review B*, **63**(20):205316, May 2001.

[50] Michal Soreni-Harari, Nir Yaacobi-Gross, Dov Steiner, Assaf Aharoni, Uri Banin, Oded Millo, and Nir Tessler. Tuning energetic levels in nanocrystal quantum dots through surface manipulations. *Nano Lett.*, **8**(2):678–684, 2008.

[51] Dov Steiner, Assaf Aharoni, Uri Banin, and Oded Millo. Level structure of InAs quantum dots in Two-Dimensional assemblies. *Nano Lett.*, **6**(10):2201–2205, 2006.

[52] Milan Sykora, Alexey Y. Koposov, John A. McGuire, Roland K. Schulze, Olexandr Tretiak, Jeffrey M. Pietryga, and Victor I. Klimov. Effect of air exposure on surface properties, electronic structure, and carrier relaxation in PbSe nanocrystals. *ACS Nano*, **4**(4):2021–2034, 2010.

[53] Toshihide Takagahara and Kyozaburo Takeda. Theory of the quantum confinement effect on excitons in quantum dots of indirect-gap materials. *Physical Review B*, **46**(23):15578–15581, December 1992.

[54] Dmitri V. Talapin, Jong-Soo Lee, Maksym V. Kovalenko, and Elena V. Shevchenko. Prospects of colloidal nanocrystals for electronic and optoelectronic applications. *Chem. Rev.*, **110**(1):389–458, 2009.

[55] Hiroyuki Tanaka and Tomoji Kawai. Partial sequencing of a single DNA molecule with a scanning tunnelling microscope. *Nature Nanotechnology*, **4**(8):518–522, 2009.

[56] Yasuhiko Terada, Byoung-Ki Choi, Seiji Heike, Masaaki Fujimori, and Tomihiro Hashizume. Placing conducting polymers onto a H-Terminated si(100) surface via a pulse valve. *Nano Lett.*, **3**(4):527–531, 2003.

[57] J. Tersoff and D. R. Hamann. Theory and application for the scanning tunneling microscope. *Physical Review Letters*, **50**(25):1998–2001, June 1983.

[58] X. W. Tu, G. Mikaelian, and W. Ho. Controlling Single-Molecule negative differential resistance in a Double-Barrier tunnel junction. *Physical Review Letters*, **100**(12):126807, March 2008.

[59] I.E. Ture, G.J. Russell, and J. Woods. Photoconductivity, structure and defect levels in CdSe crystals. *Journal of Crystal Growth*, **59**(1–2):223–228, September 1982.

[60] L. W. Wang, A. J. Williamson, Alex Zunger, H. Jiang, and J. Singh. Comparison of the kp and direct diagonalization approaches to the electronic structure of InAs/GaAs quantum dots. *Applied Physics Letters*, **76**(3):339–341, January 2000.

[61] Lin-Wang Wang and Alex Zunger. Pseudopotential calculations of nanoscale CdSe quantum dots. *Physical Review B*, **53**(15):9579–9582, April 1996.

[62] Xiaoyong Wang, Xiaofan Ren, Keith Kahen, Megan A. Hahn, Manju Rajeswaran, Sara Maccagnano-Zacher, John Silcox, George E.

Cragg, Alexander L. Efros, and Todd D. Krauss. Non-blinking semiconductor nanocrystals. *Nature*, **459**(7247):686–689, May 2009.

[63] Vanessa Wood and Vladimir Bulović. Colloidal quantum dot light-emitting devices. *Nano Reviews*, **1**(0), July 2010.

[64] Vanessa Wood, Matthew J. Panzer, Jean-Michel Caruge, Jonathan E. Halpert, Moungi G. Bawendi, and Vladimir Bulovic. Air-Stable operation of transparent, colloidal quantum dot based LEDs with a unipolar device architecture. *Nano Lett.*, **10**(1):24–29, 2009.

[65] A. D. Yoffe. Semiconductor quantum dots and related systems: Electronic, optical, luminescence and related properties of low dimensional systems. *Advances in Physics*, **50**(1):1–208, 2001.

[66] Gang Zhang and Charles B. Musgrave. Comparison of DFT methods for molecular orbital eigenvalue calculations. *J. Phys. Chem. A*, **111**(8):1554–1561, 2007.

[67] Jing Zhao, Gautham Nair, Brent R. Fisher, and Moungi G. Bawendi. Challenge to the charging model of Semiconductor-Nanocrystal fluorescence intermittency from Off-State quantum yields and multiexciton blinking. *Physical Review Letters*, **104**(15):157403, April 2010.

[68] Zhixiang Sun. *Atomic and Electronic Structure of Quantum Dots Measured with Scanning Probe Techniques*. PhD thesis, Utrecht University, January 2012.

Chapter A Calculation of DBTJ NDR model

A.1 Potential Distribution of STM junction

Followings are the code used to calculate potential distribution of STM tunneling junction. The code is written in Python language and is intended to be used by scrip function of Argos 2D package. The Argos 2D package is open source software developed by Pavel Karban et. al. for the solution of partial differential equations based on higher order finite element method. It uses planar or axis-symmetric space to render meshes used in finite element method, so it is proper to simulate STM junction with QD if we uses axis-symmetric problem settings and is simpler than full three dimensional packages like Elmer which is also available as a open software. The calculation is repeatedly done with varying vacuum barrier thickness and capping layer thickness. Total of 121 subsets are used and they correspond to capping layers from 0.1nm to 1.1nm and vacuum layers from 0.1 nm to 1.1 nm.

```
newdocument("Electrostatic Axisymmetric STM junction", "axisymmetric",
 "electrostatic", 0, 3, "disabled", 1, 1, 0, "steadystate", 0, 0, 0)

epsCap = 2
epsQD = 8
Tipdia = 4
addboundary("Zero", "electrostatic_potential", 0)
addboundary("One", "electrostatic_potential", 1)
addboundary("Border", "electrostatic_surface_charge_density", 0)

addmaterial("Vacuum", 0, 1)
addmaterial("CdSe", 0, epsQD)
addmaterial("Capping", 0, epsCap)
QDdia = 6
fileHandle = open ( 'c:\\test.txt', 'w' )

#Cappingthick = 0.5
for j in range(2,10,1):
for i in range(20):
Cappingthick = 0.1 + j*0.1
Vacthick = 0.1 +i*0.1
#Vacthick = 0.3
TipCenter = 2*Cappingthick + QDdia +Vacthick + (Tipdia/2)
QDCenter = Cappingthick +(QDdia/2)

addedge( 0, 0, 20, 0, angle = 0, marker = "Zero" )
```

```
addedge(20,0,0,20, angle = 90, marker = "Border")
addedge(0,20,0,2*Cappingthick+QDdia+Vacthick+Tipdia, angle = 0,
 marker = "Border")
addedge(0,0,0,Cappingthick,angle = 0 , marker = "Border")
addedge(0,0,QDCenter,QDCenter, angle = 90, marker = "Border")

addedge(QDCenter,QDCenter,0,2*QDCenter, angle = 90, marker =
 "Border")
addedge(0,Cappingthick,QDCenter-Cappingthick,QDCenter,
angle = 90, marker = "Border")
addedge(QDCenter-Cappingthick,QDCenter,0,Cappingthick+QDdia,
 angle = 90, marker = "Border")
addedge(0 , 2*QDCenter , 0 , TipCenter-(Tipdia/2) ,angle = 0,
marker = "Border")
addedge(0,Cappingthick,0,Cappingthick+QDdia, angle = 0,
marker = "Border")
addedge(0 , Cappingthick+QDdia , 0 , 2*QDCenter , angle = 0 ,
 marker = "Border")
addedge(0,TipCenter-(Tipdia/2),Tipdia/2, TipCenter, angle = 90 ,
 marker = "One")
addedge(Tipdia/2, TipCenter,0,TipCenter+(Tipdia/2), angle = 90 ,
 marker = "One")

addlabel(19,0.1, 0, marker = "Vacuum")
addlabel(0.1,QDCenter, 0,  marker = "CdSe")
addlabel(0.05,0.05, 0, marker = "Capping")

zoombestfit()
solve()

tipbias = pointresult(0,TipCenter-(Tipdia/2)-0.000001)
qdtopbias = pointresult(0,QDCenter+(QDdia/2))
qdbottombias = pointresult(0,QDCenter-(QDdia/2))
samplebias = pointresult(0,0)

upperbarrier = tipbias["V"] -qdtopbias["V"]
qdbias = qdtopbias["V"] - qdbottombias["V"]
lowerbarrier = qdbottombias["V"] - samplebias["V"]
fileHandle.write ( str(Cappingthick)+'\t'+ str(Vacthick)+
 '\t'+str(upperbarrier)+'\t'+str(qdbias)+"\t"+str(lowerbarrier)+"\r\n")

#print("tip bias       = "+str(tipbias["V"])+" ")
#print("qd top bias    = "+str(qdtopbias["V"])+" ")
#print("qd bottom bias = "+str(qdbottombias["V"])+" ")
#print("sample bias    = "+str(samplebias["V"])+" ")
```

```
print(" ")
print("capping thick   = "+str(Cappingthick)+" ")
print("vacuum gap      = "+str(Vacthick)+" ")
print("upperbarrier    = "+str(upperbarrier)+" ")
print("qdbias          = "+str(qdbias)+" ")
print("lowerbarrier    = "+str(lowerbarrier)+" ")

mode("node")
selectall()
deleteselection()
mode("label")
selectall()
deleteselection()


fileHandle.close()
```

A.2 DBTJ

Followings are the code used in simulations of Double Barrier Tunneling Junction with WKB approximation. The calculated potential distribution is imported from a file to determine the ratio of potential drop between vacuum and capping layer. With the WKB modeling of tunneling junction adapted to double barrier tunneling junction, current through the junction is calculated by numerical integration. And then the differential conductance is also calculated as numerical derivative.

```
data1 = ReadList[
   "d:\\lsj\\test.txt", {Number, Number, Number, Number, Number},
   WordSeparators -> "\t"];
\[Epsilon] = 2; el = 1.6*10^-19; \[Phi]1 = 5.2; \[Phi]2 = 5.3; h =
 1.05*10^-34;
m = 9.1*10^-31; \[Sigma] = 0.1; Eh = 1.0;
f := N[\!\(
\*SubsuperscriptBox[\(\[Integral]\), \(-V\), \(0\)]\(\(\(
\*SuperscriptBox[\(\[ExponentialE]\), \(\(-2\)
\*SqrtBox[
FractionBox[\(2*m*
               el*\(\(\(\(-2\) + \[Eta]1)\)*V/2 + \[Phi]1 - En)\)\),
```

```
SuperscriptBox[\(h\), \(2\)]]]*\((z)\)\)]*
\*SuperscriptBox[\(\[ExponentialE]\), \(\(-2\)
\*SqrtBox[
FractionBox[\(2*m*el*\(((\(-\[Eta]2\)*V/2 + \[Phi]2 - En)\)\),
SuperscriptBox[\(h\), \(2\)]]*\((d)\)\)])\)/\((
\*SuperscriptBox[\(\[ExponentialE]\), \(\(-2\)
\*SqrtBox[
FractionBox[\(2*m*
               el*\(((\(((\(-2\) + \[Eta]1)\)*V/2 + \[Phi]1 - En)\)\),
SuperscriptBox[\(h\), \(2\)]]*\((z)\)\)] +
\*SuperscriptBox[\(\[ExponentialE]\), \(\(-2\)
\*SqrtBox[
FractionBox[\(2*m*el*\(((\(-\[Eta]2\)*V/2 + \[Phi]2 - En)\)\),
SuperscriptBox[\(h\), \(2\)]]*\((d)\)\)])\)*
\*SuperscriptBox[\(\[ExponentialE]\), \(-
\*SuperscriptBox[\(((\((En +
              Eh + \[Eta]*
               V)\)/\[Sigma])\), \(2\)]\)]\ )\) \
\[DifferentialD]En\)];
For[i = 1, i < 121, i++,
 d = data1[[i, 1]]*10^-9;
 z = data1[[i, 2]]*10^-9;
 \[Eta]1 = data1[[i, 3]];
 \[Eta]2 = data1[[i, 5]];
 \[Eta] = (\[Eta]1 + \[Eta]2)/2;
 p = Table[f, {V, 0, 2, 0.01}];
 p2 = Differences[p];
 Print[d];
 Print[z];
 Print[ListPlot[p2, PlotRange -> All]];
 Export["d:\\lsj\\output" ~~ ToString[i] ~~ ".dat", p2, "Table"]
 ]
```

Chapter B Hexagonal Boron Nitride Thin Film on Ni(111)

We grow Hexagonal Boron Nitride (h-BN) thin film on Ni(111) surface by borazine gas dosing while heating the sample as described in chapter 3. During the experiment, we observed characteristic defects and domains from h-BN films. Here we show some exemplary images and tunneling spectra of monolayer h-BN.

(Fig. B.1) shows the typical image of monolayer h-BN film on Ni(111) surface. There exist some domain boundaries and hole type defects.

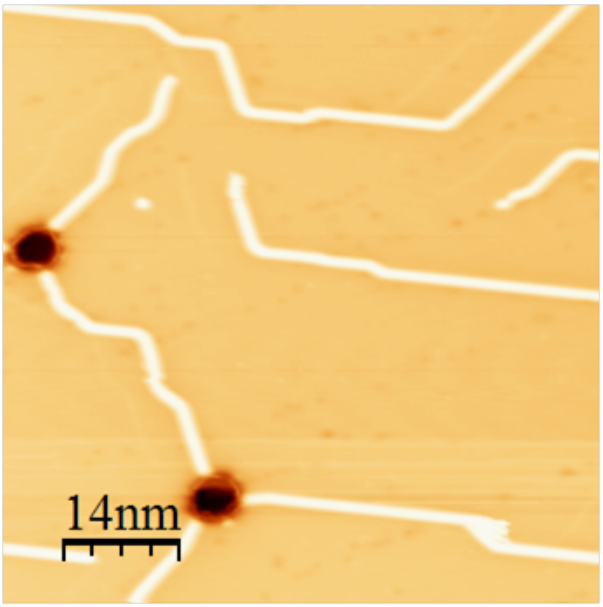

Figures B.1 **Large Scale STM Images of h-BN Monolayer on Ni(111) Surface** - h-BN monolayer on Ni(111) with two different defect types shown (line and hole types)

B.1 Various Defect Types

Two distinguished defects are observed on h-BN monolayer film.

The first one, the line type defect, shows bright protrusion for almost all bias regions. However, at positive sample bias region, the contrast between the line defects and other regions is inversed. The contrast inversion is shown in (Fig. B.2). And especially, at the bias of 1.7 V, the line type defect is shown as distinct region between two h-BN film as in (Fig. B.2 (b)). So the line type defect might be actually small size fragment of boron nitride. And sometimes the fragment can be moved by surging tunneling current. Though we cannot identify their chemical composition with STM measurement, still the major possibility is that they are h-BN fragment.

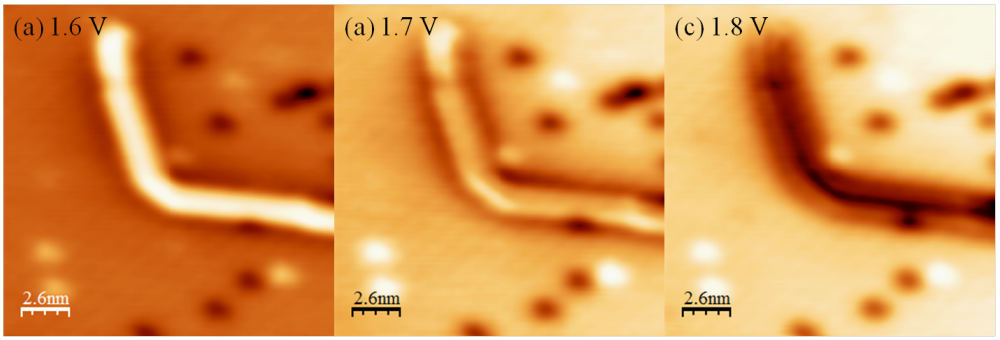

Figures B.2 **Bias dependence of the line type defect images** - (a) 1.6 V (b) 1.7 V (c) 1.8 V ; The contrast of line type defect is inversed around sample bias voltage of 1.7 V. At 1.7 V image, the internal structure of the line type defect is also shown.

Another defect type is hole type depression as in (Fig. B.3). They are usually observed at the cross point of three line type defects. And specially, the edge of the hole type defect shows atomic structure of h-BN substrate. Since nitrogen atoms have major electron density and are imaged in STM, three-fold symmetry is visible in the atomic lattice. So around the depression, we can resolve various edge types in a single

image.

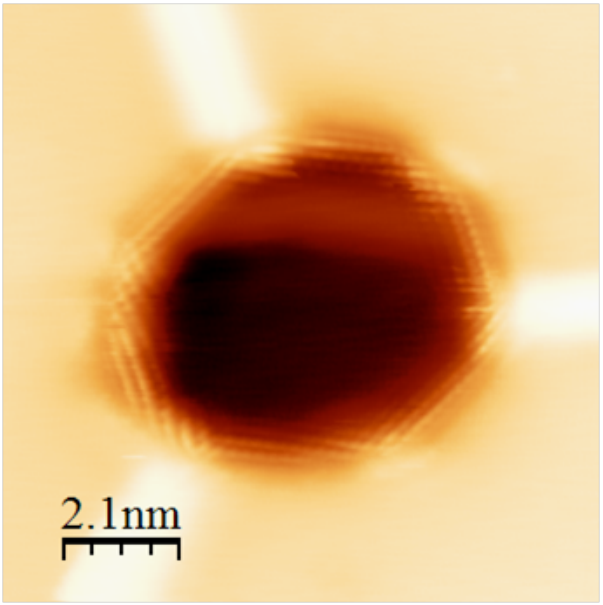

Figures B.3 **Hole Type Defect of h-BN Monolayer** - Image of hole type defect shows atomic structure of h-BN edge

B.2 Gap States Observed on the Edge of h-BN

Since h-BN film has no significant spectral structure inside the gap energy, it shows similar spectrum with nickel surface. However, at around the hole type defects, some spectral variation is observed. As shown in (Fig. B.4), some dip feature appears at the edge. Detailed structures of the dip vary from point to point.

In literature, formation of gap states by atomistic defects are already reported [3]. And applications using h-BN as template[17] or building block are significantly increasing at this time. So the observation of electronic structure change at the edge of h-BN has great importance.

And the breaking of symmetry and stoichiometry at the edge results in the bro-

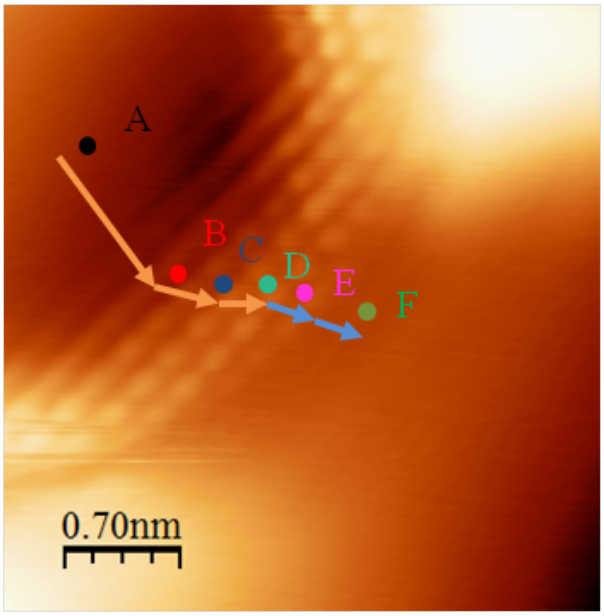

Figures B.4 **Hole Type Defect of h-BN Monolayer** - Magnified image and Points where STS results are obtained

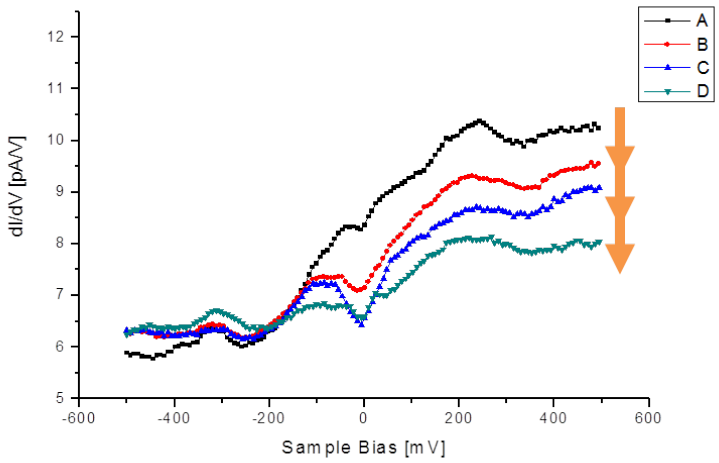

Figures B.5 **Hole Type Defect of h-BN Monolayer** - STSs show similar electronic structure for nickel(A) and h-BN(F) which reflects the suppressed electron density of boron nitride itself inside the gap energy

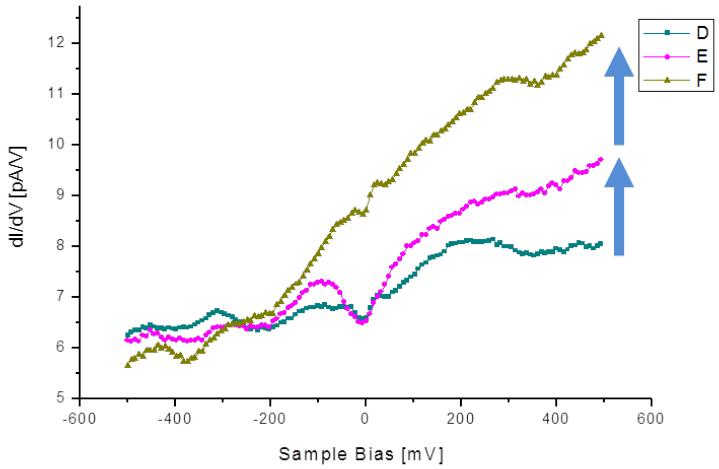

Figures B.6 **Hole Type Defect of h-BN Monolayer** - STSs from edge sites(B,C,D and E) show depressed electron density near the Fermi energy varying from different tip positions

ken electron spin population. So the exact properties are only possible with proper consideration of spin population. And also in calculation, we should consider spin polarized electronic structure[3].

In this context, further experimental characterization and calculation are still required.

Chapter C Design of Photon STM

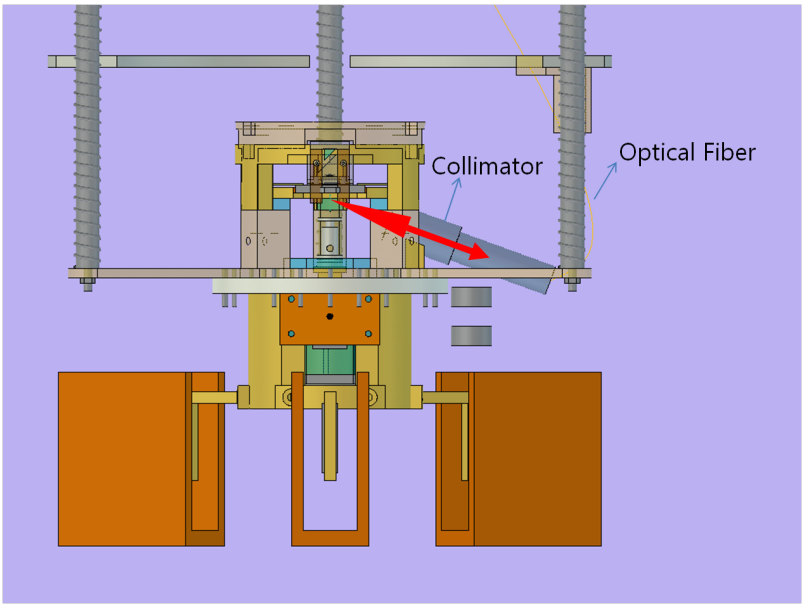

Figures C.1 **CAD Design of Photon Detection** - The generated photons by tunneling current is collected by collimating lens. Then the signal is transmitted through the optical fiber to outside of the chamber and amplified by photon multiplier tube.

초록

양자점은 크기로 변화시킬 수 있는 에너지 갭으로 인해서 양자점 디스플레이나 생물학적 발광체나 광전소자 등의 많은 응용이 예측되고 있다. 이러한 응용에 있어서 가장 큰 걸림돌이 되는 것이 발광의 깜박임(blinking) 현상이다. 이 현상을 설명하기 위해 많은 모형이 제시되었지만, 그 기본적인 역학은 아직 제대로 이해되고 있지 못하다. 최근의 단일 양자점 광발광 실험에서 양자점 마다 다른 깜박임 형태를 측정한 이후로, 양자점에 대한 더 많은 국소적인 측정이 필요해 지고 있다. 주사형 터널링 현미경과 분광학 연구는 높은 공간 및 에너지 분해능으로 인해서 이러한 양자점간 변이를 측정하는 데 적합한 장비라고 할 수 있다.

이 연구에서는 양자점을 표면에 뿌리는 방법으로 펄스형 주사방법을 사용하였다. 이 방법을 통해서 CdSe핵과 ZnS 껍데기로 이루어진 양자점을 비활성 금속인 금, 반응성 좋은 금속인 니켈, 반응성이 없는 육각격자형 질화붕소 박막등에 뿌리는 데 성공하였다. 주사터널링분광학을 이용해서 측정된 양자점의 전자구조에 있어서 일부는 순이론적 계산결과와 일치하였지만, 대부분의 양자점은 예측 못했던 에너지 갭 안의 상태를 보여주었다. 더욱이 이러한 상태는 하나의 양자점 안에서도 1 나노미터 정도의 영역에 국소적으로 존재하였다.

깜박임 현상을 설명하는 여러 모형 중 일부는 외부 포획 상태를 동원해 깜박임을 설명하고 있다. 이 연구에서 측정된 상태는 외부 포획 상태에 상응하는 상태를 측정함으로써 이러한 모형들의 타당성을 더해 주었다. 우리는 더욱 근사한 포획상태의 분포를 이용한 모형을 세워 외부 포획 상태의 원인을 불완전하게 결합한 덧씌움 분자로 설명했다. 비록 양자점 표면에서의 덧씌움 분자는 관찰하지 못했지만, 터널링 분광학 실험에서 나타난 음미분저항 현상을 설명함으로써 덧씌움 분자가 터널링

장벽을 만듦을 확인하였다. 이중 장벽에서 나타난 음미분저항에 대한 수치해석을 통해서 덧씌움 분자장벽의 두께도 확인할 수 있었다.

주사형 터널링 현미경과 광자 측정 장비를 결합 하여, 단일 양자점으로부터의 전류와 광자를 함께 측정한다면 깜박임 현상에 대한 많은 논쟁을 해결할 수 있을 것이다.

주요어: 양자점, 포획 상태, 덧씌움 분자, 부정미분저항, 주사터널링분광학
학번: 2005-20377

감사의 글

저 먼 바다로 희미하게 보이는 대륙은 참으로 매력적이었지만, 정작 눈앞에는 오직 수많은 풍랑만 가득하고 그 사이로 노를 저어야만 했던 긴 시간이었습니다. 여전히 배는 망망대해의 한 복판에 있지만, 앞서 이 길을 걸었던 많은 선배들의 발자취를 느끼며 그것을 지표 삼아 다시 한 번 한 발 한 발 나아가려 하고 있습니다. 서툴고 철없던 청년에겐 분명 벅찬 길이었지만, 한 복판에 서 있는 지금도 바다를 조금은 익숙하게 느끼고 있는 것을 보면 이제는 조금 뱃사람이 되어 간다는 생각이 듭니다.

여전히 가야 할 길은 멀지만, 박사 학위라는 중간 기착지에서 잠시 숨을 고르는 지금이 걸어왔던 길을 뒤돌아보며 또 한 번 나아갈 길을 차근히 볼 수 있는 좋은 기회가 되는 것 같습니다. 모든 순간들이 당시에는 알지 못했지만, 다시 돌이켜 보면 모두 배움의 기회였습니다. 이미 예전에 이 길을 지나갔던 선배로써, 여전히 계속해서 전진해 나아가는 연구자로써, 실험실이라는 큰 배를 이끄는 선장으로써, 늘 모두에게 배움의 기회가 되어 주셨던 국양 선생님이 계셔서 이 모든 이야기가 시작될 수 있었습니다. 앞으로 어떤 길을 가든지, 무슨 일을 하든지 저에게는 언제나 든든한 마음속의 버팀목이 되어 주실 거라 믿습니다.

시간이 지날수록 힘든 길을 헤쳐 나갈 수 있는 것은 먼저 이 길을 걸었던 선배들이 뿌려 놓은 씨앗들 덕분이라는 것을 새삼 느낍니다. 처음 실험실에 들어왔을 때, 이미 졸업을 하셔서 저에겐 큰 산과 같았던 김태환 박사님, 새파란 후배에게도 무엇이든 친절히 알려주셨던 병영이형, 뭐든 화이트보드에 친절하게 밑그림을 그려주셨던 영재형, 저널 클럽마다 날카로운 질문을 하시던 하진이형, 미팅 날짜가 같아서 미팅 때마다 바람막이가 되어주셨던 현종이형, 저에게 폴리싱의 기본을 전수해 주신 신형

준 박사님, 실험의 기본은 일희일비 하지 않는 것임을 강조해 주신 최재혁 박사님까지 시간이 꽤 흘렀지만 생생한 기억들로 남아 있습니다.

길었다면 긴 실험실 생활을 돌이켜 보면 모두 선배들과 함께 했던 추억의 조각들만 남았습니다. 진공부터 알려주며 기본적인 실험방법을 알려준 효원 누나, 늘 새벽까지 함께 일하면 야식 사주셨던 용대형, 늘 한결 같이 호두과자를 좋아하셨던 훈휘형, 무엇이든 차분하게 일하셨던 용성이형, 언제나 웃음과 함께 유쾌 했던 성철이형, 늘 그 날카로운 물리를 본받고 싶었던 중석이형, 카리스마를 본받고 싶었던 환수 형, 연구하던 모습만큼 스타 같이 했던 기억이 나는 정필이형, 언제나 맏형 같았던 정훈이형, 양계장만큼 같이 닭을 먹었던 성헌이형, 삼성 가서 본래의 카리스마를 잃은 듯한 영택이형, 도전 정신의 아이콘 희준이형, 실험실에서 늘 살았던 것 같은 정석이형, 제 옆자리 큰 형님 태권형님 까지, 모두 한 분 한 분 잊을 수 없는 추억의 조각들로 남아 있습니다.

또 즐거웠던 대학 생활을 함께 해주었던 4반 친구들, 성모, 광원, 록연, 훈민, 승현, 예령, 주완, 소진, 희태, 태경, 하나, 연정이 모두 덕분에 좋은 추억을 갖고 나아갈 수 있었고, 대학시절과 대학원 시절 늘 곁에 있어줘서 너무 든든했습니다. 때로 대학원 생활에서 벗어나고 싶을 때마다 술 한 잔 할 수 있었던 친구들 경윤이, 성철이, 동석이, 한울이, 성훈이, 주호, 희원이, 창훈이가 있어서 크게 웃을 수 있었던 건 제게 큰 행운이었습니다. 그리고 이제는 인생의 멘토가 되어주시는 손철수 선생님 그리고 최현미 선생님과 한유진 선생님, 덕분에 늘 인생에 대해 생각할 수 있었습니다. 이 모든 분들이 자칫 대학원 생활만이 전부가 될 뻔 했던 길에 세상도 들려주고 마음도 위로해 주었기에 더욱 풍성했던 지난 시간이 될 수 있었습니다.

그리고 실험실 멤버들 모두는 실험실이라는 배에서 둘 도 없는 동료들이 되어 주었습니다. 유럽을 속속들이 함께 누볐던 홍우는 때로는 편한 상담도 해주었고, 실험실에 웃음이 떠나지 않게 해주는 범용이는 진정한 매너가이로 본받고 싶었고, 사람을 좋아하시고 실험실 모두에게 새로운 바람을 넣어주신 웅돈이형은 저에게 힘

든 일이 있을 때마다 너무나 든든한 조언을 해 주셨습니다. 에너지가 도대체 어디서 그렇게 많이 나오는 지 알 수 없는 민준이에게는 너무 많은 도움을 받았고, 무엇이든 깊게 고민하고 때론 비판도 두려워 않는 정훈이와는 토론 하는 즐거움을 얻었습니다. 그 목소리를 들으면 한 없이 차분해 지는 김상희 선생님께도 늘 감사드립니다. 차분함의 최고봉 지성이와 졸업동기 유쾌 진화, 다방면 능력자 강민, 목소리 우렁찬 최고의 후배 선욱이, 아직은 오래 함께 못했지만 남은 실험실 기간 열심히 일을 도와줄 명철이와 성우, 모두 최고의 후배이자 동료가 되어 주었습니다. 그리고 누구보다도 고마웠던 일들을 일일이 다 셀 수도 없는 상준이형이 없었다면 이 여행은 단 한 발자국도 옮기지 못했을 것 같습니다.

되짚어 볼수록 감사한 분들이 너무 많아서 저는 정말 행운아였다는 생각이 듭니다. 어머니께서 종종 말씀하셨던 “넌 운이 좋으니까 잘 될 거야‘’라는 말씀은 아마도 이 모든 분들이 제 주변에 있음을 알려 주신 게 아닐까 합니다. 이제는 누구보다도 소중한 영은이가 있어서 힘들다는 것을 잊을 수 있었고, 동생에게는 늘 편안한 누나가 있어서 든든했습니다. 마지막으로 늘 묵묵히 아들을 지켜봐 주시는 어머니, 아버지께는 말로는 고마움을 다 하기 어려울 것 같습니다. 앞으로도 마음속 깊이 최선을 다하는 아들을 보여드리겠습니다.

이제 졸업이라는 작은 파도를 넘고 더 큰 바다로 나가려는 순간입니다. 두렵고 떨리기도 하고, 앞으로 다가올 멋진 일들이 기대도 되는 순간입니다. 지금까지 함께 해주셨던 고마운 인연들만큼 앞으로도 새롭게 만들어갈 멋진 인연이 있을 것을 기대하면서 나아가겠습니다. 모두에게 감사드립니다.